Università degli Studi di Padova

DIPARTIMENTO DI INGEGNERIA DELL'INFORMAZIONE
Corso di Laurea Magistrale in Ingegneria dell'Automazione

System Identification for Control Design of a Brushless Eccentric Deviator

Candidato:
Michele Dominese
Matricola 1122566

Relatore:
Mattia Zorzi

Correlatori:
Stefano Venturini
Daniele Borghese

Anno Accademico 2017-2018

Ringraziamenti

Vorrei ringraziare il prof. Mattia Zorzi, relatore di questa tesi di laurea, per la disponibilità e precisione dimostratemi durante tutto il periodo di stesura. Senza di Lei non sarei mai riuscito a svolgere tutto questo lavoro.

Ringrazio inoltre tutte le persone che mi hanno seguito durante il mio percorso in azienda. In particolare, vorrei ringraziare l'ingegner Daniele Borghese che, grazie al suo prezioso aiuto, mi ha guidato durante tutto il periodo che ho passato in azienda.

Un grande abbraccio va a tutta la mia famiglia. Senza tutto il supporto fornitomi da mia madre, mio padre e dalle mie due sorelle non sarei mai riuscito ad arrivare dove sono oggi. Un grande bacio va anche ai miei nipotini che oggi sono qua a sostenermi con la loro spensieratezza e i loro sorrisi. Un caloroso ricordo va anche a mio nonno che avrebbe tanto voluto assistere alla mia laurea ma che purtroppo oggi non può essere qui.

Con affetto ringrazio Doris, la mia morosa, che nonostate tutto è sempre vicino a me e mi sostiene sempre. Grazie a lei ho avuto la forza di andare avanti anche nei momenti più difficili o in cui ero demotivato. Grazie di cuore.

Non posso non menzionare Francesca, Carmen e Fabio. Grazie a voi le giornate in quel del DEI sono state decisamente più semplici. Vi prometto che le nostre serate frico (o le uscite per bere una Carlo V) non finiranno anche se saremo tutti in città diverse.

Un ultimo dovuto ringraziamento va al mio PC che mi ha accompagnato per tutta la mia carriera universitaria e ha deciso di smettere di funzionare poche setttimane prima di questo giorno.

E infine ringrazio, soprattutto, me stesso per la determinazione e l'impegno attuo a raggiungere questo traguardo, la voglia di sfidarmi, per averci provato ed esserci riuscito.

Contents

Introduction

System identification techniques represent a useful tool when the mathematical description of the system is not well known. The latter is a data-driven technique whose aim is to find the relation between input $\mathbf{u}$ and output $\mathbf{y}$, i.e. the mathematical model, of the underlying system. In this thesis, System Identification will be exploited to design a PID controller for such a system. Moreover, there will be a detailed analysis to see if this procedure is a valid option to design a controller for an industrial machine as well as the next steps that should be taken in order to improve the performances of the system.

The system used for the analysis is a brushless eccentric deviator developed by SMS Group; all tests on the machine were performed in their facilities in Tarcento (UD). The starting point of this work was to use System Identification methods to estimate a model for this system in such a way that the best parameters of the PID controller, used to control it, are chosen in a systematic way. This thesis will show that System Identification tools can give a good representation of the underlying system and this can be used as starting point to design a better controller.

With the results obtained from the tests and the MATLAB SIMULINK tool it was also performed the analysis and design of a feed-forward input that was already implemented in the system but its performances were not optimal. It will be shown that the opportunity to have the information deriving by the System Identification results was a good improvement for the decision and design of the feed-forward input.

This thesis is the first step for the realization of a more complex and automatized controller of the system. The main goal is to develop, in the future, a procedure that uses System Identification methods to learn automatically the machine's configuration, which is set by the product type that the plant is working on, and also change the values of the PID and of the feed-forward input in order to gain a better and more suitable response of the system.

This thesis will give a quick review on the theory on synchronous brushless electric motors and an overview on the mechanical modelling of an eccentric shaft to get a better view on how the deviator works. Later on, there will be a breif review the System Identification techniques used in this work, an explanation on how the tests were performed and the analysis of the System Identification results obtained from the data of the experiments. Afterwards the design of the PID controller and feed-forward input will be discussed and it will be compared with the real model response. Finally, there will be a section regarding future improvements on the flexibility and robustness of the controller

that are advised to be implemented in future works.

All the experiments on the deviator were performed with specific constrains imposed by the System Identification methods. For this reason it was necessary a little change on the code (written in CODESYS) developed by the company. The modified code will be provided up on request.

Useful Notations

Below some useful notations, that can help the reading of this thesis, are reported.

- $v(\cdot)$, $i(\cdot)$ and $\lambda(\cdot)$ denotes the instantaneous voltage, current and flux of the motor respectively. The upper-case version corresponds to the steady state version of the quantities.
- ϑ denotes the angle of the rotor; the angle ϑ_{me} is referred as the electromechanical angle.
- ω or $\dot{\vartheta}$ are used to identify the angular velocity of the rotor; ω_{me} is referred as the electromechanical angular velocity.
- The quantities reported in bold and with an apex, i.e. $\mathbf{g}^s(\cdot)$, are instantaneous three-phase quantities expressed in vectorial form.
- $\ddot{\vartheta}$, $\dot{\omega}$ or a are used to detote the acceleration of the rotor.
- τ is used to denote the instantaneous torque of the motor.
- Quantities expressed in italic text, i.e. $w(\cdot)$, $y(\cdot)$, are deterministic vectors.
- Quantities expressed in bold, i.e. $\mathbf{u}(\cdot)$, $\mathbf{y}(\cdot)$, are random vectors.
- θ denotes the parameter of a model.
- Variables with the hat symbol (i.e. $\hat{\theta}$) are estimated values.
- The estimated models $\mathcal{M}$ with the apex A are referred to the position loop estimation with the configuration A of the deviator; similar notation is used for the models with the B configuration.
- The estimated models $\mathcal{M}$ with the apex A_V are referred to the position speed estimation with the configuration A of the deviator; similar notation is used for the models with the B configuration.

Chapter 1

Physical Modelling of a Brushless Eccentric Deviator

In this chapter there will be an introduction to the brushless eccentric deviator and a quick explanation on the work that it performs. This plant is costituted by two foundamental elements: the eccentric shaft and the brushless three-phase syncronous motor. The deviator, shown in Fig. 1.1, is usually installed in the mill and it is used to deviate the iron rod between the production lane and the waste lane. The plant is followed by a shear that, synchronized with the deviator, it cuts the iron rod that have to be removed from the final product, such as, the rod's head and tail.

Figure 1.1: Back of the brushless eccentric deviator.

In Fig. 1.2 it is shown a close up on all the main components of the deviator. In Fig. 1.2(a) it can be seen the final part of the machine and how it is interconnected with the shear: in the picture are highlighted the knives, that are used to cut the iron rod, and the ferrule, attached at the end of the tube moved by the eccentric shaft. Moreover, the ferrule is the part of the deviator that changes accordingly to the various type of

product that is currently in production by the plant. Fig. 1.2(b) and 1.2(c) show the main components that are responsible for the motion part of the mechanical device: the eccentric shaft and the brushless three-phase synchronous motor. For the motion control part, the communication with the plant and the security or error management are handled by the drive M702, see Fig. 1.2(d).The latter can be programmed and customized.

(a) End on the deviator with its ferrule and shear of the plant.

(b) Back of the deviator.

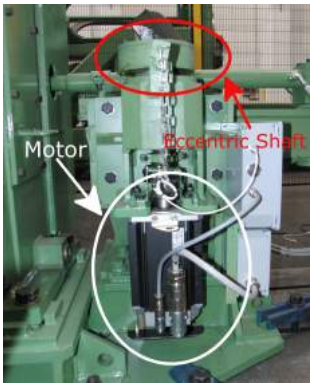

(c) Side of the deviator.

(d) Drive that is in charge of the control of the deviator.

Figure 1.2: Overview of the deviator components: *in 1.2(a) it can be seen the deviator end and the shear, in 1.2(a) there is another picture of the back of the deviator, in 1.2(c) it is shown a close up to the main components that are responsible of the motion, in 1.2(d) it can be seen the controller of the system.*

During the period of the thesis it was developed a code in CODESYS, the programming language used on the drive, in order to perform all the tests on the deviator which will be presented in the following.

As it can be seen with this quick description of the plant, the model is quite complex and, more importantly, it varies according to the type of product that the plant is currently manufacturing. The scope of this thesis is to see if, by means of System Identification, it is possible to design in a systematic way a PID controller for each configuration of the deviator.

The result obtained from the System Identification tools will be also compared with the ones obtained from the model derived by the physic of the motor and the eccentric shaft. For this reason, in the following sections there will be a quick overview about the brushless three-phase synchronous motor model as well as a simple modellization of the eccentric shaft.

1.1 Operating Principles of Brushless Three-phase Synchronous Motor

A brushless three-phase synchronous motor is an electrical device that converts electrical energy into mechanical. The motor is composed by a fixed part (stator), in which are located the windings of the three phase, and a rotating part (rotor), where the permanent magnet are situated. Rotor and stator are both made of laminated ferromagnetic material with cylindrical shape and separated by a small air gap, see Fig. 1.3.

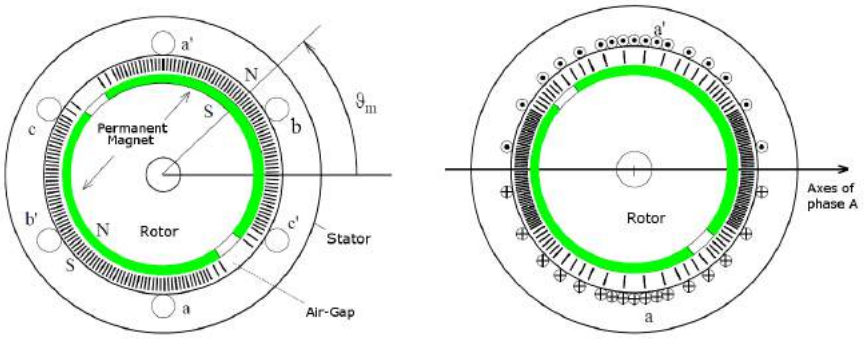

Figure 1.3: Cutaway of a brushless three-phase synchronous motor: *in the left picture it is shown how the three phases are disposed spatially and also the flux of the permanent magnets, in the right image it is displayed how the conductors of a phase are disposed and the corrispective flux created from that phase.*

The conductors of all the phases are arranged along the stator in equal number and distribution (in Fig. 1.3 indicated with *a-a'*,*b-b'* and *c-c'*). The three phases are shifted reciprocally by an angle equal to $\frac{2}{3}\pi$.

When a triplet of alternated current flows in the conductors of the three phases a magnetic field is created and overlapped with the one created by the permanent magnets. This will cause a synchronous rotation of the rotor with the magnetic field produced by the three currents. In what follows it is derived the mathematical model for such a model; for more detail see [1].

The voltage balance of each phase of the motor can be written as:

$$\begin{aligned} v_a(t) &= Ri_a(t) + \frac{\mathrm{d}\lambda_a(t)}{\mathrm{d}t} \\ v_b(t) &= Ri_b(t) + \frac{\mathrm{d}\lambda_b(t)}{\mathrm{d}t} \\ v_c(t) &= Ri_c(t) + \frac{\mathrm{d}\lambda_c(t)}{\mathrm{d}t}. \end{aligned} \tag{1.1}$$

Where $i_a(t)$, $i_b(t)$ e $i_c(t)$ are the current of each phase and $\lambda_a(t)$, $\lambda_b(t)$ e $\lambda_c(t)$ are the concatenated flux of each phase. In (1.1) it was assumed that R is the phase resistance and it is equal for all the phases. The flux of the three-phases can be written as:

$$\begin{aligned}\lambda_a(t) &= Li_a(t) + \Lambda_{mg}\cos(\vartheta_{me}(t)) \\ \lambda_b(t) &= Li_b(t) + \Lambda_{mg}\cos(\vartheta_{me}(t) - \tfrac{2}{3}\pi) \\ \lambda_c(t) &= Li_c(t) + \Lambda_{mg}\cos(\vartheta_{me}(t) - \tfrac{4}{3}\pi).\end{aligned} \tag{1.2}$$

Here, Λ_{mg} is the flux produced by the permanent magnets, L is the inductance of each phase that was assumed equal for all the phases and ϑ_{me} is the electromechanical angle between the phase a and the permanent magnet position. Substituting (1.2) into (1.1) it follows that

$$\begin{aligned}v_a(t) &= Ri_a(t) + L\frac{\mathrm{d}i_a(t)}{\mathrm{d}t} + e_a(t) \\ v_b(t) &= Ri_b(t) + L\frac{\mathrm{d}i_b(t)}{\mathrm{d}t} + e_b(t) \\ v_c(t) &= Ri_c(t) + L\frac{\mathrm{d}i_c(t)}{\mathrm{d}t} + e_c(t)\end{aligned} \tag{1.3}$$

where $e_k(t)$ with $k = a, b, c$ trpresent the electromotive force of phase k.The latter are defined as follows:

$$\begin{aligned}e_a(t) &= \tfrac{\mathrm{d}\lambda_{a,mg}(t)}{\mathrm{d}t} = -\Lambda_{mg}\omega_{me}(t)\cos(\vartheta_{me}(t) + \tfrac{\pi}{2}) \\ e_b(t) &= \tfrac{\mathrm{d}\lambda_{b,mg}(t)}{\mathrm{d}t} = -\Lambda_{mg}\omega_{me}(t)\cos(\vartheta_{me}(t) + \tfrac{\pi}{2} - \tfrac{2}{3}\pi) \\ e_c(t) &= \tfrac{\mathrm{d}\lambda_{c,mg}(t)}{\mathrm{d}t} = -\Lambda_{mg}\omega_{me}(t)\cos(\vartheta_{me}(t) + \tfrac{\pi}{2} - \tfrac{4}{3}\pi)\end{aligned} \tag{1.4}$$

where ω_{me}, expressed in $\frac{rad_{el}}{s}$[1], is the electromechanical velocity.

To simplify the notations a compact form to express the three-phase quantities as spatial vector notation is introduced:

$$\mathbf{g}(t) = \frac{2}{3}\left[g_a(t) + g_b(t)e^{j\frac{2}{3}\pi} + g_c(t)e^{j\frac{4}{3}\pi}\right]. \tag{1.5}$$

Using the compact form introduced in Equation (1.5), then Equation in (1.4) can be written as[2]:

$$\mathbf{e}^s(t) = \frac{\mathrm{d}\boldsymbol{\lambda}^s_{mg}}{\mathrm{d}t} = j\Lambda_{mg}\omega_{me}e^{j\vartheta_{me}} = j\omega_{me}\boldsymbol{\lambda}^s_{mg}. \tag{1.6}$$

Similarly, Euation (1.3) can also be rewritten as:

$$\mathbf{v}^s = R\mathbf{i}^s + L\frac{\mathrm{d}\mathbf{i}^s}{\mathrm{d}t} + \mathbf{e}^s = R\mathbf{i}^s + L\frac{\mathrm{d}\mathbf{i}^s}{\mathrm{d}t} + j\omega_{me}\boldsymbol{\lambda}^s_{mg}. \tag{1.7}$$

By applying the energy balance to Equation (1.3) it can be written:

$$v_a\cdot i_a + v_b\cdot i_b + v_c\cdot i_c = R(i_a^2 + i_b^2 + i_c^2) + \frac{\mathrm{d}}{\mathrm{d}t}\left[\frac{1}{2}L(i_a^2 + i_b^2 + i_c^2)\right] + e_a\cdot i_a + e_b\cdot i_b + e_c\cdot i_c. \tag{1.8}$$

[1]Notice that the rad_{el} represent the mechanical angles between two poles of the motor.

[2]From now on, dependence from the time will be omitted for the sake of clarity.

In (1.8) four terms can be identified. On the left hand side of the equation there is the instantaneous power absorbed by the motor. The term $R(i_a^2+i_b^2+i_c^2)$ is the Joule dissipated power and $\frac{\mathrm{d}}{\mathrm{d}t}\left[\frac{1}{2}L(i_a^2+i_b^2+i_c^2)\right]$ is the power used to create the magnetic field. The last of the three terms represent the generated electromechanical power i.e the electrical power that is converted in mechanical power which can be expressed by the product of the generated torque and the mechanical velocity, that is

$$e_a \cdot i_a + e_b \cdot i_b + e_c \cdot i_c = \frac{\tau \omega_{me}}{p}. \tag{1.9}$$

Substituting (1.4) in (1.9) it can be found the expression of the generated torque:

$$\tau = \Lambda_{mg} p \left[i_a \cos(\vartheta_{me} + \frac{\pi}{2}) + i_b \cos(\vartheta_{me} + \frac{\pi}{2} - \frac{2}{3}\pi) + i_c \cos(\vartheta_{me} + \frac{\pi}{2} - \frac{4}{3}\pi) \right]. \tag{1.10}$$

Again, using a notation like the one that was previously introduced, but fixing the vector with the rotor instead of the stator[3].

With this simplification of notations the flux of the permanent magnet will be $\boldsymbol{\lambda}_{mg}^r = \Lambda_{mg} + j0$ and equations in (1.3) become:

$$\begin{aligned} \mathbf{v}^r &= R\mathbf{i}^r + L\tfrac{\mathrm{d}\mathbf{i}^r}{\mathrm{d}t} + j\omega_{me}L\mathbf{i}^r + j\omega_{me}\Lambda_{mg} \\ v_d &= Ri_d + L\tfrac{\mathrm{d}i_d}{\mathrm{d}t} - L\omega_{me}i_q \\ v_q &= Ri_q + L\tfrac{\mathrm{d}i_q}{\mathrm{d}t} + L\omega_{me}i_d + \omega_{me}\Lambda_{mg} \end{aligned} \tag{1.11}$$

where v_d is the real part of the vector $\mathbf{v}^r$ and v_q it is the imaginary part. Applying again the energy balance to equation (1.11) it follows:

$$(v_d i_d + v_q i_q)\mathrm{d}t = [R(i_d^2 + i_q^2)]\mathrm{d}t + L(i_d \mathrm{d}i_d + i_q \mathrm{d}i_q) + \omega_{me}\Lambda_{mg} i_q \mathrm{d}t. \tag{1.12}$$

Similarly to before, four terms can be identified, but this time the term responsible for the electromechanical energy has a very simple form; in fact, noting that p is the number of poles of the motor, it can be written as follows:

$$\tau = \frac{3}{2} p \Lambda_{mg} i_q \tag{1.13}$$

which depends only on i_q and the factor $\frac{3}{2}$ is due to the conversion between the vector in abc to the vector in $\mathbf{g}^r$.

From the last two equation in (1.11) the block scheme of a brushless three-phase synchronous motor can be drawn. In Fig 1.4, it can be seen in the green box, the block diagram of a brushless motor derived from equations in (1.11). The block $\mathrm{F_i}(s)$ represent the transfer function of the inverter which is the device that generates the needed three-phase altarnate voltage; it has a transfer function that can usually can usually be expressed as it follows:

$$\mathrm{F_i}(s) = \frac{1}{\tau_c s + 1} \tag{1.14}$$

[3]The change between the two vectorial representation can be performed by $\mathbf{g}^r = \mathbf{g}^s e^{j\vartheta_{me}}$, where the apex s, as before, represent vectors fixed with the stator and r vectors fixed with the rotor.

where $\tau_c = \frac{T_s}{2}$ and T_s is the switching time. The blocks $\mathrm{F_d}(s)$ and $\mathrm{F_q}(s)$ are the transfer function of the axes d and q; if, as in our case, the motor is symmetric and isotropic the two block are identical and equal to:

$$\mathrm{F_q}(s) = \frac{1}{Ls + R}. \tag{1.15}$$

The last block, $\mathrm{F_L}(s)$ represents a simple load that is attached to the motor. If the load is affected by a viscous friction with coefficient equal to B and total inertia, i.e. load inertia plus rotor inertia, equal to J, then it follows:

$$\mathrm{F_L}(s) = \frac{1}{Js + B} \tag{1.16}$$

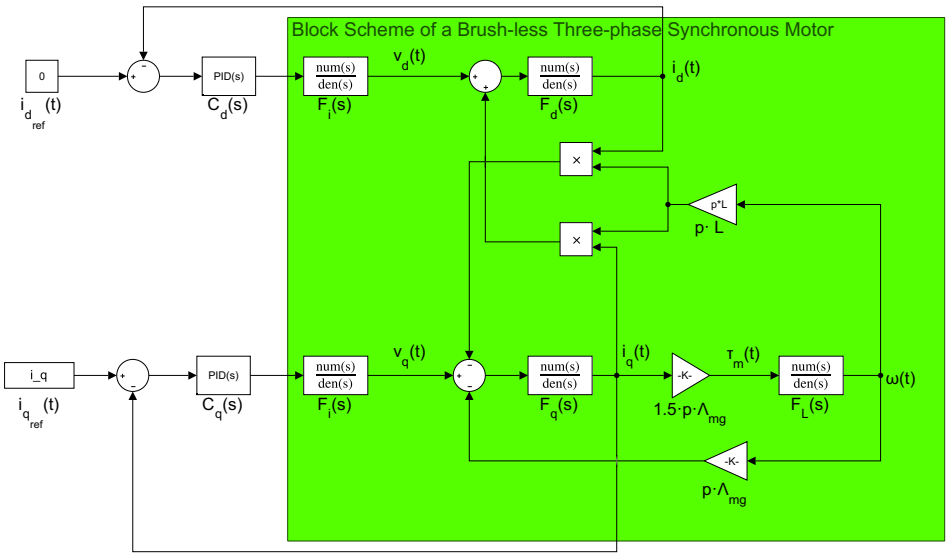

Figure 1.4: Block diagram of a brushless three-phase synchronous motor with control loop: *in the green box is reported the modellization of the motor,* $\mathrm{C_d}(z)$ *and* $\mathrm{C_q}(z)$ *are the controllers of* $i_d(t)$ *and* $i_q(t)$.

In Fig. 1.4 it is also showed the controllers that are usually applied to the motors. The two axes are controlled separately and there is a non-linear action to decouple and linearise the two axes. Usually the input of the d axis is set to 0 and the input of the q axis is set to the value of torque that has to be applied. In this case the two controllers $\mathrm{C_d}(s)$ and $\mathrm{C_q}(s)$ are PID controllers.

Another important aspect of a brushless three-phase synchronous motor regards its operating limits, which usually derive from construction features of the motor. To ease the analysis the following equation are going to focus only in the steady-state. Therefore, all the currents and voltages of the motor are sinusoidal and with magnitude and frequency constant over the time, furthermore the velocity ω is constant and equal to Ω.

Assuming that the voltage and the current of the motor must not overtake the values I_N and V_N, then:

$$\begin{aligned} I_d^2 + I_q^2 &\leq I_N^2 \\ V_d^2 + V_q^2 &\leq V_N^2. \end{aligned} \tag{1.17}$$

In the steady-state the equation in (1.11) can be rewritten as:

$$\begin{aligned} V_d &= RI_d - \Omega_{me} L I_q \\ V_q &= RI_q + \Omega_{me} L I_d + \Omega_{me} \Lambda_{mg}. \end{aligned} \tag{1.18}$$

Since all the values are constant, all the contributions deriving by the derivatives over the time are null. Substituting (1.18) in (1.17) and neglecting the term of the resistive voltage drop (usually small), it follows:

$$(\Omega_{me} L I_q)^2 + (\Omega_{me} L I_d + \Omega_{me} \Lambda_{mg})^2 \leq V_N^2. \tag{1.19}$$

That latter be rewritten as:

$$\left(I_d + \frac{\Lambda_{mg}}{L} \right)^2 + I_q^2 \leq \frac{V_N^2}{\Omega_{me}^2 L^2}. \tag{1.20}$$

The limits of a brushless motor expressed in the plane $I_d - I_q$ are represented visually in Fig. 1.5. The circle of radius I_N represent the maximum current that can be applied. The deviator application works exclusively in the segment $\overline{BB'}$ which are the point with maximum torque per ampere (MTPA). For this reason, during the simulation of the model, the reference of $i_d(t)$was always forced to 0.

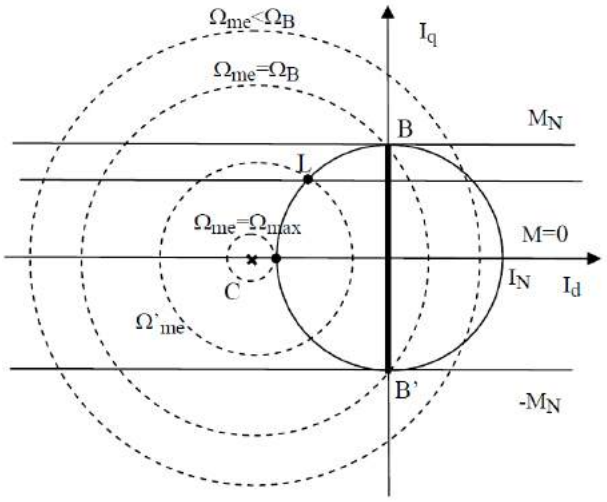

Figure 1.5: Brushless three-phase synchronous motor operating limits: *the horizontal lines are the points with the same generated torque and the segment $\overline{BB'}$ are the MTPA points, the circle with center in the origin is the current limit, the dashed circle are the possible operating speed of the motor.*

The brushless motor used on the eccentric deviator is an EMERSON 190UDF150JAAEA and its technical specifications are reported below:

- Nominal voltage $V_N = 460\,V$;
- Nominal current $I_N = 21.4\,A$;
- Number of poles $2p = 10$;
- Phase resistance $R = 0.173694\,\Omega$;
- Phase inductance $L = 4.179\,mH$;
- Switching time of the inverter $T_s = 62.5\,\mu s$;
- Time costant of the inverter $\tau_c = 31.25 \cdot 10^{-6}$;
- Nominal speed $\Omega_N = 1500\,\text{rpm} \; = 157.0796\,\frac{\text{rad}}{s}$;
- Torque per ampere $\frac{3}{2}p\Lambda_{mg} = 3.2\,\frac{Nm}{A}$;
- Permanent magnet flux $\Lambda_{mg} = 0.4267\,Wb$;
- Nominal torque $\tau_N = \frac{3}{2}p\Lambda_{mg}I_N = 68.48\,Nm$;
- Maximum torque $\tau_{Max} = 3.5\tau_N = 239.68\,Nm$;
- Maximum current $I_{Max} = 74.9\,A$;
- Rotor inertia $J_M = 0.01035\,kgm^2$.

The parameters can be fond in the motor data-sheet [2] or, eventually, in the M-Connect file of the application. An important aspect on the motor is that, as it can be seen from its specification, it is capable to sustain and generate high values of current which goes up to the 350% of the nominal torque; obviously this is possible only for a short period of time. Moreover, a high usage of the motor in overcharge condition implies a faster wear of the motor and, as it will be clear later on, this is one of the purpose that pushed the company to consider System Identification tools for the design of the PID controllers.

1.2 Modellization of the Eccentric Shaft

To give a modellization of the eccentric shaft the first step was to search for some literature. It was found a model for eccentric systems driven by DC motors [3] dynamic equations has been obtained by using the Lagrangian theory. In Fig. 1.6 it can be seen how the eccentric device was modelled.

Unfortunately the data needed to characterize this model were not sufficient so, after further research on the information gathered from the file that the company provided, it was possible to derive a schematic physical modellization of the eccentric device as the one reported in Fig. 1.7.

The length of all the reported segments are known since they are constants used to build the eccentric deviator. From this schematic modellization it can be created a link to the components of the eccentric deviator previously introduced. More specifically:

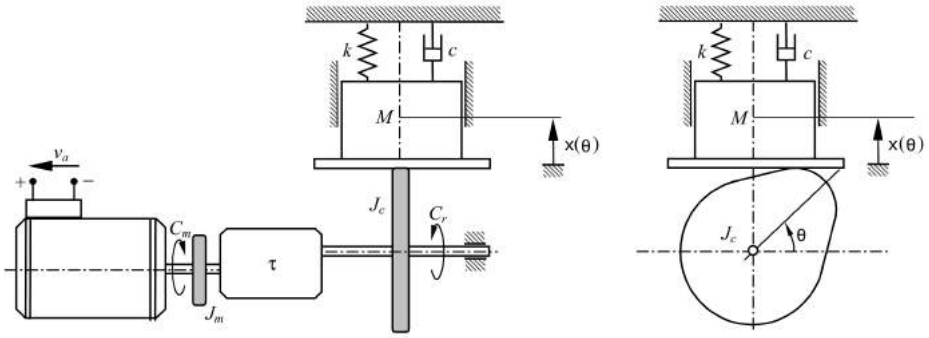

Figure 1.6: Modellization of the eccentric shaft found in the literature: *side view (left), top view (right).*

- The segments $\overline{MA}$, $\overline{AB}$ and $\overline{BC}$ are the schematic modellization of the eccentric shaft;
- The segment of length L is the tube that is attached to the machine showed in Fig. 1.1 and 1.2(b);
- The rectangle attached to the end of the tube is the schematic representation of the ferrule.

The device is showed in three different configurations: starting position (blue and with subscript 0), with the rotor of the motor at an angle equal to ϑ (green and with subscript ϑ) and at its maximum degree (redand with subscript f). With M is represented the rotor of the motor; the point A is constrained to move along the circumference of radius a; points B and C are bound to the x axis[4]. Note that, the segment $\overline{OC_i}$ where $i = 0, \vartheta, f$ is not constant.

In the file of the company the length of the segment were the following ones:

$$\begin{aligned} a &= 20 \cdot 10^{-3}\, m \\ b &= 330.01 \cdot 10^{-3}\, m \\ c &= 95 \cdot 10^{-3}\, m \\ L &= 1521 \cdot 10^{-3}\, m \\ \overline{OC_0} &= l = 575 \cdot 10^{-3}\, m. \end{aligned} \tag{1.21}$$

It is worth keeping in mind that the values in (1.21) were derived from a file that was done for the an older deviator of the conpany and consequentially, those values may be slightly different from the ones of the deviator on which the test were performed. This can lead to small different physical characteristic, i.e. the tube mass (and consequentially its inertia). With that in mind, this modellization will be used to simulate the model and compare it with the one obtained with the System Identification methods.

[4]Note that the segment $\overline{BC}$ lies always on the x axis

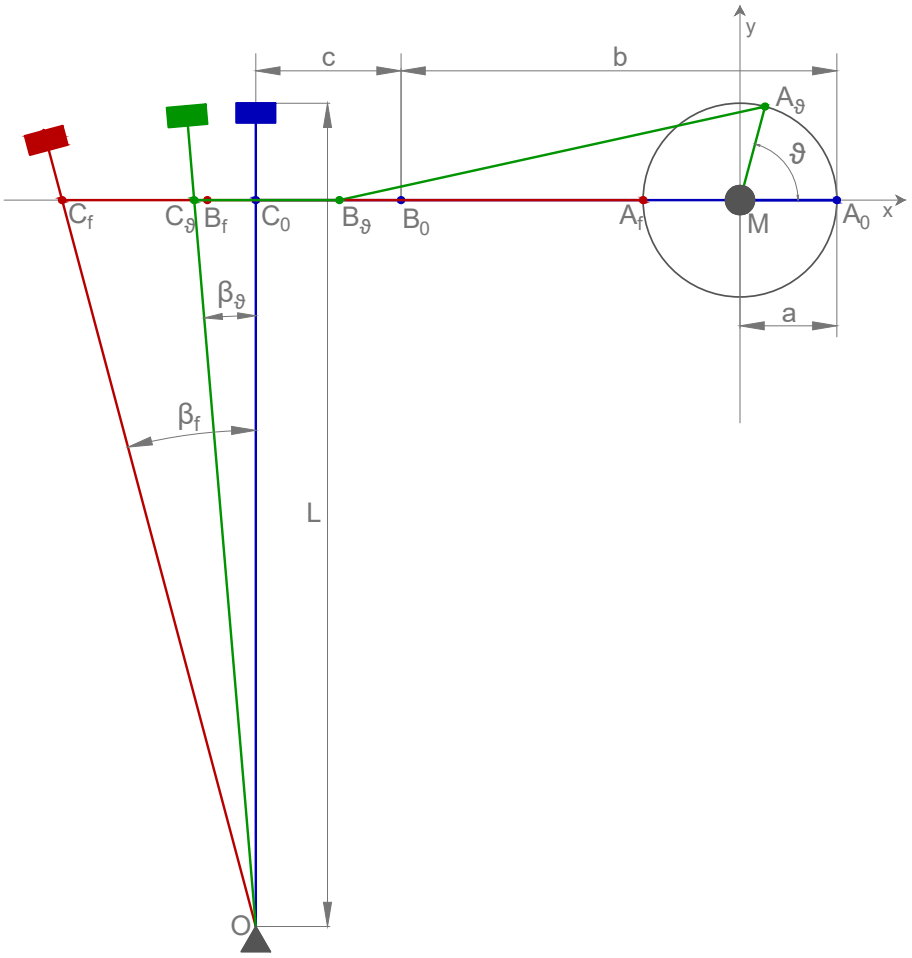

Figure 1.7: Schematic physical modellization of the eccentric shaft in different positions: *in blue and with subscript* 0 *the model in the usual start position, in green and with subscript* ϑ *the model in a position between* $[0, \pi]$*, in red and with subscript* f *the usual final position of the model.*

The Lagrangian of the schematic system can be expressed by:

$$\mathcal{L} = K - V = \frac{1}{2}\left[J\dot{\vartheta}^2 + J_T\dot{\beta}^2\right] \tag{1.22}$$

where K is the kinetic energy and V is the potential energy; J is the sum of the inertia of the motor's rotor and the eccentric shaft inertia (for the eccentric daviator $J = 0.029177\,kgm^2$). Moreover, J_T is the inertia tube of length L and is calculated without the contribution of the ferrule (for the eccentric daviator $J_T = 12.8\,kgm^2$). The angle ϑ and β are respectively the angle of the rotor and the angle the tube from its starting position to its actual position. Note that the Lagrangian has not any contribution from the potential energy (i.e. $V = 0$) terms since there are no positional forces.

In what follows, the goal is to find the motion equations that depend only on the variable ϑ and its time derivatives. The first step is to write the coordinates of the point

C as a funcion of ϑ.

$$x_C(\vartheta) = a\cos\vartheta - \sqrt{b^2 - a^2\sin^2\vartheta} - c \tag{1.23}$$

Moreover, the angle β is given by:

$$\begin{aligned} l\tan(\beta(\vartheta)) &= a - b - c - a\cos\vartheta + \sqrt{b^2 - a^2\sin^2\vartheta} + c \\ &= a(1-\cos\vartheta) - b + \sqrt{b^2 - a^2\sin^2\vartheta} \\ \tan(\beta(\vartheta)) &= k(1-\cos\vartheta) - j + \sqrt{j^2 - k^2\sin^2\vartheta} \\ \beta(\vartheta) &= \arctan\left[f(\vartheta)\right] \end{aligned} \tag{1.24}$$

where it is recalled that $l = \bar{OC}_0$. Moreover, $k = \frac{a}{l}$, $j = \frac{b}{l}$ and $f(\vartheta) = k(1-\cos\vartheta) - j + \sqrt{j^2 - k^2\sin^2\vartheta}$. The derivative over the time of the angle β can be expressed by:

$$\begin{aligned} \dot{\beta}(\dot{\vartheta},\vartheta) &= \tfrac{1}{f(\vartheta)^2+1}\tfrac{\partial f(\vartheta)}{\partial\vartheta}\dot{\vartheta} \\ \tfrac{\partial f(\vartheta)}{\partial\vartheta} &= k\sin\vartheta - \tfrac{k^2}{2}\tfrac{\sin(2\vartheta)}{\sqrt{j^2-k^2\sin^2\vartheta}} := \sqrt{g(\vartheta)}. \end{aligned} \tag{1.25}$$

To get the motion equation of the eccentric shaft it is required to solve the equation $\frac{\mathrm{d}}{\mathrm{d}t}\left(\frac{\partial\mathcal{L}}{\partial\dot{\vartheta}}\right) - \frac{\partial\mathcal{L}}{\partial\vartheta}$. In the case of the eccentric shaft $\mathcal{L} = K$ and, substituting (1.25) if follows:

$$\mathcal{L}(\dot{\vartheta},\vartheta) = \frac{1}{2}\left[J + J_T\frac{g(\vartheta)}{\left(f(\vartheta)^2+1\right)^2}\right]\dot{\vartheta}^2 \tag{1.26}$$

where $g(\vartheta) = g_1(\vartheta) + g_2(\vartheta) + g_3(\vartheta)$ with

$$\begin{aligned} g_1(\vartheta) &= \tfrac{k^4}{4}\tfrac{\sin^2(2\vartheta)}{j^2-k^2\sin^2\vartheta} \\ g_2(\vartheta) &= -k^3\tfrac{\sin(2\vartheta)\sin\vartheta}{\sqrt{j^2-k^2\sin^2\vartheta}} \\ g_3(\vartheta) &= k^2\sin^2\vartheta. \end{aligned} \tag{1.27}$$

Now there are all the ingredients to proceed and compute the terms that are needed to derive the motion equation. More specifically:

$$\begin{aligned} \tfrac{\partial\mathcal{L}}{\partial\dot{\vartheta}} &= \left[J + J_T\tfrac{g(\vartheta)}{(f(\vartheta)^2+1)^2}\right]\dot{\vartheta} \\ \tfrac{\mathrm{d}}{\mathrm{d}t}\left(\tfrac{\partial\mathcal{L}}{\partial\dot{\vartheta}}\right) &= \left[J + J_T\tfrac{g(\vartheta)}{(f(\vartheta)^2+1)^2}\right]\ddot{\vartheta} + J_T\tfrac{\partial}{\partial\vartheta}\left(\tfrac{g(\vartheta)}{(f(\vartheta)^2+1)^2}\right)\dot{\vartheta}^2 \\ \tfrac{\partial\mathcal{L}}{\partial\vartheta} &= \tfrac{1}{2}J_T\tfrac{\partial}{\partial\vartheta}\left(\tfrac{g(\vartheta)}{(f(\vartheta)^2+1)^2}\right)\dot{\vartheta}^2 \end{aligned} \tag{1.28}$$

where the term $\frac{\partial}{\partial\vartheta}\left(\frac{g(\vartheta)}{(f(\vartheta)^2+1)^2}\right)$ can be computed as it follows:

$$\frac{\partial}{\partial\vartheta}\left(\frac{g(\vartheta)}{\left(f(\vartheta)^2+1\right)^2}\right) = \frac{\partial g(\vartheta)}{\partial\vartheta}\frac{1}{\left(f(\vartheta)^2+1\right)^2} - \frac{\partial}{\partial\vartheta}\left(\left(f(\vartheta)^2+1\right)^2\right)\frac{g(\vartheta)}{\left(f(\vartheta)^2+1\right)^4}. \tag{1.29}$$

Dividing Equation (1.29) in two blocks and remembering how $g(\vartheta)$ is defined,

$$\begin{aligned} \tfrac{\partial g(\vartheta)}{\partial\vartheta} &= \tfrac{\partial g_1(\vartheta)}{\partial\vartheta} + \tfrac{\partial g_2(\vartheta)}{\partial\vartheta} + \tfrac{\partial g_3(\vartheta)}{\partial\vartheta} \\ \tfrac{\partial g_1(\vartheta)}{\partial\vartheta} &= \tfrac{k^4}{4}\tfrac{2\sin(4\vartheta)(j^2-k\sin^2\vartheta)+j\sin^3(2\vartheta)}{\left(j^2-k^2\sin^2\vartheta\right)^2} \\ \tfrac{\partial g_2(\vartheta)}{\partial\vartheta} &= -\tfrac{k^3}{2}\tfrac{\sqrt{j^2-k^2\sin^2\vartheta}}{j^2-k^2\sin^2\vartheta}\left[\sin(3\vartheta)\left(3 + \tfrac{k^2}{4\left(j^2-k^2\sin^2\vartheta\right)}\right) - \tfrac{k^2}{4}\tfrac{\sin(5\vartheta)}{j^2-k^2\sin^2\vartheta} - \sin\vartheta\right] \\ \tfrac{\partial g_3(\vartheta)}{\partial\vartheta} &= k^2\sin(2\vartheta) \end{aligned} \tag{1.30}$$

$$\frac{\partial}{\partial\vartheta}\left(\left(f(\vartheta)^2+1\right)^2\right)=2\left(f(\vartheta)^2+1\right)2f(\vartheta)\frac{\partial f(\vartheta)}{\partial\vartheta}$$
$$\frac{\partial}{\partial\vartheta}\left(\left(f(\vartheta)^2+1\right)^2\right)\frac{g(\vartheta)}{(f(\vartheta)^2+1)^4}=4\frac{f(\vartheta)}{(f(\vartheta)^2+1)^3}\left(\frac{\partial f(\vartheta)}{\partial\vartheta}\right)^3. \tag{1.31}$$

Now all the terms to write the motion equation of the system are known so, if the motor generated the torque τ_m, it follows that the motion equation is

$$\left[J+J_T\frac{g(\vartheta)}{\left(f(\vartheta)+1\right)^2}\right]\ddot{\vartheta}+\frac{1}{2}h(\vartheta)\vartheta^2=\tau_m \tag{1.32}$$

where $h(\vartheta)=\frac{\partial}{\partial\vartheta}\left(\frac{g(\vartheta)}{(f(\vartheta)^2+1)^2}\right)$.

From (1.32) it can be clearly seen the part that rule the presence of the eccentric shaft. Furthermore, this result was used to add the action of the eccentric part into the MATLAB SIMULINK modellization. A simple way to do so is to subtract to the motor torque the torque generated by the mechanic, in other words subtract to τ_m the value of $\frac{1}{2}h(\vartheta)\vartheta^2$.

As it was said before, this model derived from the physics will be used in Section 4.1 to see if our initial analysis was good enough.

Chapter 2

System Identification Techniques

In this chapter there will be a breif introduction on what System Identification is, why and how is performed. Roughly speaking System Identification is the discipline which develops data driven modelling techniques, i.e. the model is found by using the collected data from the system. For more details, see [8], [9] or [10].

In Fig. 2.1 it can be seen the usual block scheme diagram of an industrial plant and, as it will be explained in Section 3.1, this set-up is similar also to the plant of the eccentric deviator.

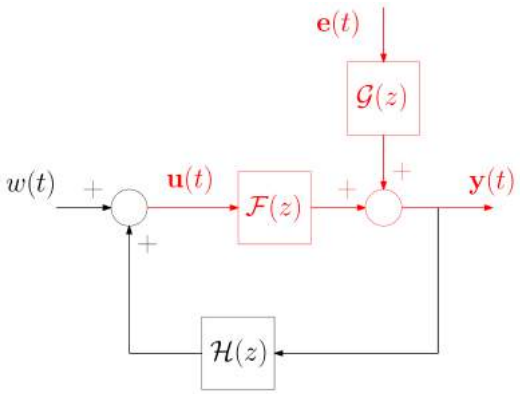

Figure 2.1: Typical model of a plant: *in red the two "blocks" that the System Identifications techniques aims to find.*

Such a diagram correspond to the mathematical relations:

$$\begin{cases} \mathbf{y}(t) = \mathcal{F}(z)\mathbf{u}(t) + \mathcal{G}(z)\mathbf{e}(t) \\ \mathbf{u}(t) = \mathcal{H}(z)\mathbf{y}(t) + w(t). \end{cases} \tag{2.1}$$

Here, $\mathcal{F}(z)$ represents the plant; $\mathbf{u}(t)$ and $\mathbf{y}(t)$ the input and the output (wiyhout noise) of the plant, respectively; $\mathcal{G}(z)\mathbf{e}(t)$ is the noise acting on the output of the plant; $\mathcal{H}(z)$ is the controller; $w(t)$ is the reference signal.

The goal of System Identification is to find the relations between $\mathbf{u}(t)$ and $\mathbf{y}(t)$ or, in other words, to find the functions $\mathcal{F}(z)$ and $\mathcal{G}(z)$. The typical assumption is that $\mathcal{F}(z)$ and $\mathcal{G}(z)$ are rational transfer functions.

Withon the identification procedure of a unknown system, it is possible to identify the following steps:

1. Experiment setup: This is a preliminar task that has the goal of setting up the right conditions to perform the identification in the optimal way (i.e. the design of input $\mathbf{u}(t)$); this topic will be treated, for the eccentric deviator, in Section 3.1.

2. Data Processing: The data are filtered or processed to ease the identification procedure; the latter are useful in the nexts steps.

3. Model Structure Design: A class of models structures $\mathcal{M}$ for $\mathcal{F}(z)$ and $\mathcal{G}(z)$ is chosen.

4. Training Step: The identification procedure is performed for all the model structure $\mathcal{M}$ chosen in the previous step.

5. Validation: The optimal model, say $\mathcal{M}_{OPT}\left(\hat{\theta}\right)$ is chosen using different validation methods.

2.1 Data Processing

Data Filtering: Sometimes the relation between the input and the output of the plant, here denoted by $\tilde{u}(t)$ and $\tilde{y}(t)$, respectively, partially known. If this happen it can be written that:

$$\tilde{y}(t) = \mathcal{F}_{known}(z)\mathcal{F}(z)\tilde{u}(t) \tag{2.2}$$

where $\mathcal{F}_{known}(z)$ represent the known dynamics.

By multiplying Equation (2.2) by $\left(z^l\mathcal{F}_{known}(z)\right)^{-1}$ it follows:

$$\frac{1}{z^l\mathcal{F}_{known}(z)}\tilde{y}(t) = \frac{1}{z^l}\mathcal{F}(z)\tilde{u}(t) \tag{2.3}$$

where $l \in \mathbb{N}$ is such that the relation $z^l\mathcal{F}_{known}(z)$ and its inverse are causal. Therefore, the filtered data

$$\begin{aligned} u(t) &= \tfrac{1}{z^l}\tilde{u}(t) \\ y(t) &= \tfrac{1}{z^l\mathcal{F}_{known}(z)}\tilde{y}(t) \end{aligned} \tag{2.4}$$

will be used to estimate $\mathcal{F}(z)$ and $\mathcal{G}(z)$. Finally, the identified model will be:

$$\tilde{\mathbf{y}}(t) = \mathcal{F}_{known}(z)\mathcal{F}(z)\tilde{\mathbf{u}}(t) + \mathcal{G}(z)z^l\mathcal{F}_{known}(z)\mathbf{e}(t). \tag{2.5}$$

In Section 3.1, it will be shown that, for one of the two types of identification procedure performed, some dynamics of the transfer function of the eccentric deviator is known. In

this case the known part is an integrator and so, to have the inverse of $\mathcal{F}_{known}(z)$ causal, it is needed that $l = 1$. Moreover, this implies:

$$\begin{aligned} \mathcal{F}_{known}(z) &= \tfrac{1}{z-1} \\ \tfrac{1}{z^l \mathcal{F}_{known}(z)} &= \tfrac{z-1}{z} \\ u(t) &= \tfrac{1}{z}\tilde{u}(t) \\ y(t) &= \tfrac{1}{z^l \mathcal{F}_{known}(z)}\tilde{y}(t). \end{aligned} \tag{2.6}$$

Data Detrending: If the data $\tilde{u}^N := [\tilde{u}(1) \dots \tilde{u}(N)]$ and $\tilde{y}^N := [\tilde{y}(1) \dots \tilde{y}(N)]$ are not with zero mean the System Identification procedure can give bad results, for example the estimation of poles close to the unit circle which cause numerical problems in the numerical optimization. A way to deal with this problem is to detrend the data using the following procedure:

1. Compute the simple mean of the data:

$$\bar{y}^N = \frac{1}{N}\sum_{t=1}^{N} \tilde{y}^N, \qquad \bar{u}^N = \frac{1}{N}\sum_{t=1}^{N} \tilde{u}^N; \tag{2.7}$$

2. Define $y(t) = \tilde{y}(t) - \bar{y}^N$ and $u(t) = \tilde{u}(t) - \bar{u}^N$;
3. Estimate the model $\mathbf{y}(t) = \mathcal{F}(z)\mathbf{u}(t) + \mathcal{G}(z)\mathbf{e}(t)$
4. Add the mean of the data to the estimated model:

$$\tilde{\mathbf{y}}(t) = \mathcal{F}(z)\tilde{\mathbf{u}}(t) + \mathcal{G}\mathbf{e}(t) + \bar{y}^N - \mathcal{F}(z)\bar{u}^N. \tag{2.8}$$

2.2 Model Structure Design

As stated before, the search of $\mathcal{F}(z)$ and $\mathcal{G}(z)$ is restricted to rational transfer functions. Then, they can be written:

$$\begin{aligned} \mathcal{F}(z) &= \tfrac{b_0 + b_1 z^{-1} + \dots + b_{n_B - 1} z^{-n_B + 1}}{1 + f_1 z^{-1} + \dots + f_{n_F} z^{-n_F}} \\ \mathcal{G}(z) &= \tfrac{1 + c_1 z^{-1} + \dots + c_{n_C} z^{-n_C}}{1 + d_1 z^{-1} + \dots + d_{n_D} z^{-n_D}}. \end{aligned} \tag{2.9}$$

From the literature, the following parametric model structure $\mathcal{M}(\theta)$ have been proposed: Box-Jenkins, Output Error, ARMAX and ARX. Unfortunately, since the knowledge on the system is limited, no preliminary assumptions can be made on the structure of $\mathcal{F}(z)$ and $\mathcal{G}(z)$ and so it was not possible to restrict the identification to to a specific model structure. In what follows these model structures are going to be introduced.

Box-Jenkins: The Box-Jenkins (BJ) model structure is described as follows:

$$\mathbf{y}(t) = \frac{\mathrm{B}(z)}{\mathrm{F}(z)}\mathbf{u}(t - n_k) + \frac{\mathrm{C}(z)}{\mathrm{D}(z)}\mathbf{e}(t) \tag{2.10}$$

where

$$\begin{aligned} \mathrm{B}(z) &= \sum_{k=0}^{n_B-1} b_k z^{-k} \\ \mathrm{F}(z) &= 1 + \sum_{k=0}^{n_F} f_k z^{-k} \\ \mathrm{C}(z) &= 1 + \sum_{k=0}^{n_C} c_k z^{-k} \\ \mathrm{D}(z) &= 1 + \sum_{k=0}^{n_D} d_k z^{-k}; \end{aligned} \tag{2.11}$$

$n_k \geq 0$ is the input delay used to avoid algebraic loops, $\mathbf{e}$ is a white noise with unknown variance σ^2. In this case, the parameters vector characterizeing the model is:

$$\theta = [b_0, \ldots, b_{n_B-1}, f_1, \ldots, f_{n_F}, c_1, \ldots, c_{n_C}, d_1, \ldots, d_{n_D}]\,. \tag{2.12}$$

The polynomials $\mathrm{F}(z)$, $\mathrm{C}(z)$ and $\mathrm{D}(z)$ have all the roots inside the unit circle. In this way BIBO stability of the model is guaranteed.

The Output Error (OE) models are a particular type of BJ models where $\mathrm{C}(z) = 1$ and $\mathrm{D}(z) = 1$. Therefore,

$$\mathbf{y}(t) = \frac{\mathrm{B}(z)}{\mathrm{F}(z)}\mathbf{u}(t - n_k) + \mathbf{e}(t). \tag{2.13}$$

ARMAX: The ARMAX models are described as follows:

$$\mathrm{A}(z)\mathbf{y}(t) = \mathrm{B}(z)\mathbf{u}(t - n_k) + \mathrm{C}(z)\mathbf{e}(t) \tag{2.14}$$

where

$$\begin{aligned} \mathrm{A}(z) &= 1 + \sum_{k=0}^{n_A} a_k z^{-k} \\ \mathrm{B}(z) &= \sum_{k=0}^{n_B-1} b_k z^{-k} \\ \mathrm{C}(z) &= 1 + \sum_{k=0}^{n_C} c_k z^{-k} \end{aligned} \tag{2.15}$$

$n_k \geq 0$ is the input delay used to avoid algebraic loops, $\mathbf{e}$ is a white noise with unknown variance σ^2.

The vector θ has a structure similar as the one introduced before.

The ARX models are a type of ARMAX models with $\mathrm{C}(z) = 1$

$$\mathrm{A}(z)\mathbf{y}(t) = \mathrm{B}(z)\mathbf{u}(t - n_k) + \mathbf{e}(t). \tag{2.16}$$

2.3 Training Step

The training step consists on the application of the prediction error minimization (PEM) method to find the parameter θ by using the model structure $\mathcal{M} : \mathbf{y}(t) = \mathcal{F}_\theta(z)\mathbf{u}(t) + \mathcal{G}_\theta(z)\mathbf{e}(t)$ where the subscript θ means that $\mathcal{F}(z)$ and $\mathcal{G}(z)$ are parametrized according to the chosen model structure. The corresponding model will be denoted by $\mathcal{M}(\theta)$ This method tries to find the optimal unknown θ that better explains the data $\tilde{u}^N := [\tilde{u}(1) \dots \tilde{u}(N)]$ and $\tilde{y}^N := [\tilde{y}(1) \dots \tilde{y}(N)]$.

More precisely, finds the optimal model by minimizing the prediction error under model $\mathcal{M}(\theta)$, which is defined as $\boldsymbol{\varepsilon}_\theta(t) := \mathbf{y}(t) - \hat{\mathbf{y}}(t|t-1)$ where

$$\hat{\mathbf{y}}(t|t-1) = \mathcal{G}(z)^{-1}\mathcal{G}_1(z)\mathbf{y}(t) + \mathcal{G}(z)^{-1}\mathcal{F}(z)\mathbf{u}(t) \tag{2.17}$$

and $\mathcal{G}_1(z) = \mathcal{G}(z) - I$ where I is the identity matrix. Assume now that the acquired data are collected from $t = 1, \dots, N$, where N is the time instant of the last data collected The error $\varepsilon_\theta(t)$ can be computed for all $t = 1, \dots, N$ and an estimate of θ can be found by minimizing the term

$$\sum_{t=1}^{N} \varepsilon_\theta(t)^2. \tag{2.18}$$

This minimization leads to the so called PEM estimate:

$$\hat{\theta}_{PEM}(y^N, u^N) = \arg\min \left(\frac{1}{N} \sum_{t=1}^{N} \varepsilon_\theta^2(t) \right) = \arg\min V_N(\theta). \tag{2.19}$$

The solution of (2.19) is usually not simple, however, if the model structure is ARX, then the model in (**??**) and the one-step-ahead predictor can be written as:

$$\begin{aligned} \mathbf{y}(t) &= \boldsymbol{\varphi}(t)^T\theta + \mathbf{e}(t) \\ \hat{\mathbf{y}}(t|t-1) &= \boldsymbol{\varphi}(t)^T\theta \end{aligned} \tag{2.20}$$

where $\boldsymbol{\varphi}(t)$ is defined as

$$\boldsymbol{\varphi}(t) := [-\mathbf{y}(t-1) \ \dots \ -\mathbf{y}(t-n_A) \ \ \mathbf{u}(t-1) \ \dots \ \mathbf{u}(t-n_B)]^T \tag{2.21}$$

Now, using the data $u^N = [u(1) \ \dots \ u(N)]$ and $y^N = [y(1) \ \dots \ y(N)]$ generated by the model, it follows:

$$V_N(\theta) = \frac{1}{N} \sum_{t=1}^{N} \varepsilon_\theta^2 = \frac{1}{N} \|\bar{\varepsilon}_\theta\|^2 = \frac{1}{N} \|y^N - \Phi\theta\|^2 \tag{2.22}$$

where

$$\Phi := \begin{bmatrix} \varphi(1) \\ \vdots \\ \varphi(N) \end{bmatrix} \quad \bar{\varepsilon}_\theta := \begin{bmatrix} \varepsilon_\theta(1) \\ \vdots \\ \varepsilon_\theta(N) \end{bmatrix} \tag{2.23}$$

Finally, under the constraint that Φ has full column rank, it follows:

$$\hat{\theta}_{PEM}(y^N, u^N) = \left(\Phi^T\Phi\right)^{-1} \Phi^T y^N. \tag{2.24}$$

2.4 Validation

Validation techniques are useful tools that helps the task of finding the optimal model $\mathcal{M}_{OPT}\left(\hat{\theta}_{PEM}\right)$ between all the model structures $\mathcal{M}_k\left(\hat{\theta}_{PEM}\right)$ with $k = 1, \ldots, M$ obtained in previous step. In this section there will be a quick explanation of the theory behind all the techniques used during the deviator tests. More importantly, later on, there will be also an analysis on the effectiveness of the various validation techniques used in this thesis.

The method that will be considered are the following ones:

- Residual Analysis;
- Zero-Pole Cancellation;
- Complexity Terms;
- Cross-Validation.

Residual Analysis: The Residual Analysis is a validation method that uses the correlation of $\boldsymbol{\varepsilon_{\hat{\theta}_{PEM}}}(t) = \mathbf{y}(t) - \hat{\mathbf{y}}(t|t-1)$, Equation (2.25) below, to obtain a plot that captures the goodness of the performed PEM estimate[1]:

$$r_{\boldsymbol{\varepsilon_{\hat{\theta}_{PEM}}}}(s) = \bar{\mathbb{E}}_{\theta_0}\left[\boldsymbol{\varepsilon_{\hat{\theta}_{PEM}}}(t+s)\boldsymbol{\varepsilon_{\hat{\theta}_{PEM}}}(t)\right]. \tag{2.25}$$

The more $\boldsymbol{\varepsilon_{\hat{\theta}_{PEM}}}(t)$ is similar to $\mathbf{e}(t)$, the more $\mathcal{M}\left(\hat{\theta}_{PEM}\right)$ describes the underling system. Therefore, the more $r_{\boldsymbol{\varepsilon_{\hat{\theta}_{PEM}}}}(s)$ is similar to (i.e. it doesn't exceed prefixed bounde)

$$r_{\boldsymbol{\varepsilon_{\hat{\theta}_{PEM}}}}(s) \approx \begin{cases} \sigma^2 & s = 0 \\ 0 & s \neq 0 \end{cases} \tag{2.26}$$

the more the analyzed model structure can be considered a good representation of the underling system.

Figure 2.2 shows two different Residual Analysis plots. The yellow zone on the plot is the confidence region that $r_{\boldsymbol{\varepsilon_{\hat{\theta}_{PEM}}}}(s)$ should not exceed. This region is plotted using the statistical properties of $\varepsilon_{\hat{\theta}_{PEM}}$ and all the details can be found in the notes [10].

Zero-Pole Cancellation: This validation technique consists in plotting the zero-pole diagram of the transfer function $\mathcal{F}_{\hat{\theta}_{PEM}}(z)$ and choose the model structure that has the fewest number of zero-pole cancellations.

In Fig. 2.3 is shown an example of a transfer function that should be avoided. As it can be seen there are two pairs of zero-pole (zeroes represented with a circle and poles with a cross) which have a zero and a pole really close to each other. This proximity

[1]The operator $\bar{\mathbb{E}}$ is defined as follows: $\bar{\mathbb{E}}\left[\mathrm{u}(t)\right] = \lim_{N\to\infty} \frac{1}{N} \sum_{t=1}^{N} \mathbb{E}\left[\mathrm{u}(t)\right]$ where $\mathrm{u}(t)$ is a quasi-stationary process.

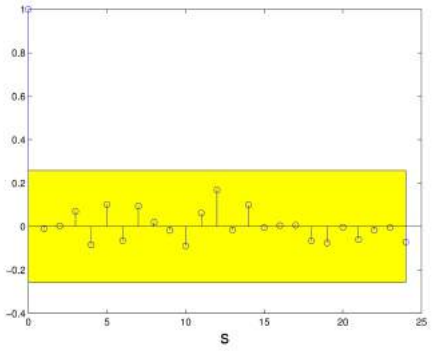

(a) An examples of a Residual Analysis of a good identified model.

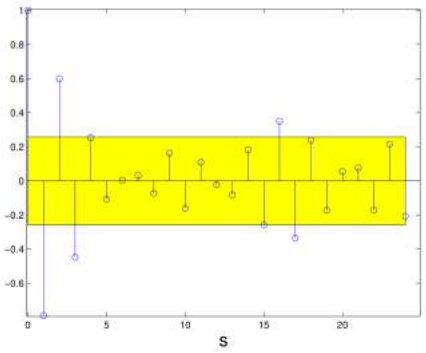

(b) An examples of a Residual Analysis of a bad identified model.

Figure 2.2: Examples of Residual Analysis plots

implies that a cancellation between the zero and pole could be performed. Furthermore, if this happens, than it means that a simpler model with a fewer number of parameters can be used. Notice that in Fig. 2.3 the zero-pole cancellation on the left side it is not an exact cancellation (like the one on the right) but, if it is possible, it should be avoided.

Another characteristic of the transfer function that, if possible, should be avoided is the presence of poles near the unitary circle (always reported with a dashed line in all the figures). Their presence may cause instability so, between different models, if possible it should chosen the one that has less or hopefully no poles near the unit circle.

This method is going to be one of the key element during the search of the optimal model structure of the deviator especially during the identification of the position loop model. In fact this method was used in the first place to discard a large number of models that were affected by cancellations and in a second place to chose the optimal model when two of them had similar performances on all the other tests.

Criteria with Complexity Terms: The creteria with Complexity Terms are choice criteria whic evaluates the candidate models according to two terms. The best model minimizes the sum of these two terms. The first one favours the model structures that well explain the data. The second term favours the simpler model structures, i.e. the models with a fewer number of parameters.

During the deviator tests two types of Complexity Terms were used: the Akaike information criterium (AIC) and the Minimum description length criterium (MDL or BIC). The two terms are defined as follows:

1. The AIC Criterium considers the following two terms:

$$J_{AIC}(\mathcal{M}) = (N-k)\log V_N(\hat{\theta}_{PEM}) + 2p \tag{2.27}$$

where p is the number of parameters, N is the length of the data, k is the number of data used to initialize the one-step ahead predictor and

$$V_N(\hat{\theta}_{PEM}) = \frac{1}{N}\sum_{t=1}^{N} \varepsilon^2_{\hat{\theta}_{PEM\,(y^N,\,u^N)}}(t) \tag{2.28}$$

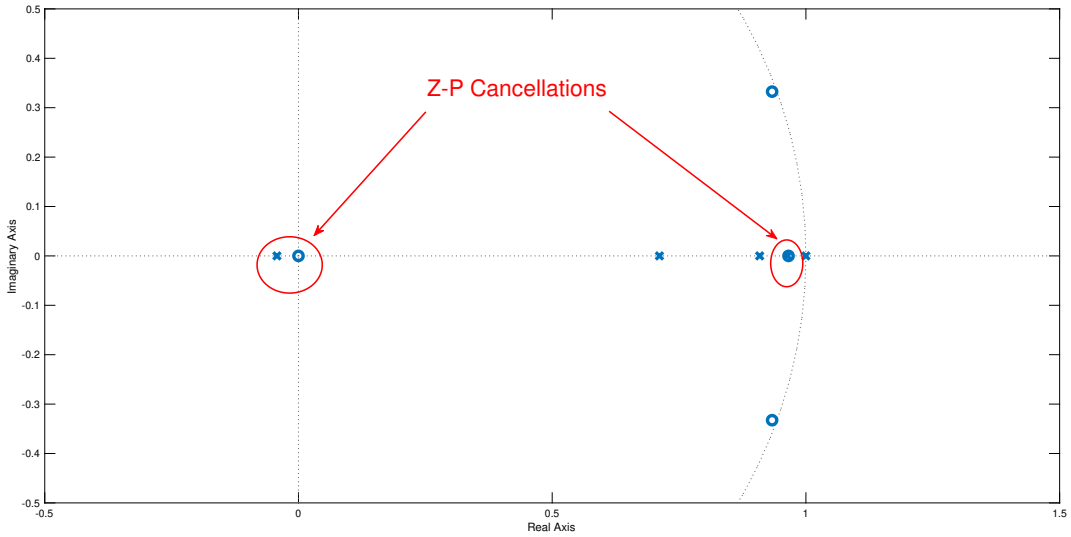

Figure 2.3: Example of a bad zero-pole diagram: *two pairs of zero (blue circle) and pole (blue cross), highlighted inside the two red circle, that could cause a cancellation in the transfer function* $\mathcal{F}_{\hat{\theta}_{PEM}}(z)$. *This plot is taken from one of the model structure obtained from the tests.*

2. The BIC Criterium considers the following two terms:

$$J_{BIC}(\mathcal{M}) = V_N \cdot \left(1 + \frac{p \log N}{N}\right) \tag{2.29}$$

where all the values are defined as before.

As it will be clear from the results, those two criteria represent an effective tool to design an exciting input for the underlying system. More importantly, these methods were perfect to chose the optimal model.

Cross-Validation: The Cross-Validation techniques use different datasets generated by the underlying $\mathcal{M}(\theta_0)$ to ease the choice of the optimal model $\mathcal{M}_{OPT}\left(\hat{\theta}_{PEM}\right)$. More specifically, if the model $\mathcal{M}(\hat{\theta}_{PEM})$ can explain the data acquired from the underlying system, even in different conditions, then it means that $\mathcal{M}\left(\hat{\theta}_{PEM}\right)$ effectively capture the real dynamics of the model.

The following steps are the ones that are usually used to perform the Cross-Validation analysis:

1. Compute the PEM estimate using the first dataset.
2. Compute the prediction error $\varepsilon^{N_V}_{\hat{\theta}_{PEM}}(t)$ by using an unseen dataset y^t_V with $t = 1 \dots N_V$.
3. Compute the "*fit*" (percent) of the prediction capability which is defined as:

$$\text{Fit}\left(\mathcal{M}\left(\hat{\theta}_{PEM}\right)\right) = \left(1 - \frac{\|\varepsilon^{N_V}_{\hat{\theta}_{PEM}}\|}{\|y^{N_V}_V - \bar{y}^{N_V}_V\|}\right) \cdot 100 \tag{2.30}$$

where N_V is the length of the validation dataset and

$$\begin{aligned} \varepsilon_{\hat{\theta}_{PEM}}^{N_V} &= \left[\varepsilon_{\hat{\theta}_{PEM}}(1) \ \dots \ \varepsilon_{\hat{\theta}_{PEM}}(N_V)\right]^T \\ y_V^{N_V} &= \left[y_{\hat{\theta}_{PEM}}^V(1) \ \dots \ y_{\hat{\theta}_{PEM}}^V(N_V)\right]^T \\ \bar{y}_V^{N_V} &= [1 \ \dots \ 1]^T \frac{1}{N_V} \sum_{t=0}^{N_V} y_V(t). \end{aligned} \tag{2.31}$$

4. Choose the model that better explain the true model behaviour and thus that maximizes the fit in (2.30).

As it will be shown later, this method can be very useful to distinguish how the different estimated models perform, in particular in the situation where the input is not sufficiently exiting. Moreover, like the criteria with Complexity Terms, the Cross-Validation method represent an effective tool to design an exiting input for the underlying system.

Chapter 3

System Identification of the Brushless Eccentric Deviator

In this Chapter it can be found a detailed explanation and analysis of the various steps of the identification procedure when applied on the brushless eccentric deviator system.

More in detail, the first part of the chapter focuses on how the eccentric deviator set up is composed and what are the model structures that are going to be identified with the System Identification tool. Secondly, there will be a focus on the problems that derive from the limits imposed from both the company (and/or the system) and from the System Identification theory. As it will be shown the main problem was to design an input that was sufficiently exciting for the eccentric deviator. The next two sections can be considered as the first step of the usual identification procedure described in Chapter 2.

In the final part of the Chapter along with the analysis of the identification results on the eccentric deviator there will be also a quick overview on which are the analysed model structures and how it was performed the validation test. Additionally, when all the results of the tests are analysed a quick conclusion will be reported.

3.1 Experimental Set-Up

In this first Section there it will be explained how it was structured the set-up of the brushless eccentric deviator. Starting with how its plant was structured, Figure 3.1 shows the control scheme that was used on the eccentric deviator. In the green box of the picture it is shown the block that represents the deviator system or, in other words, the uknown part of the studied model. It can be seen that it is possible to measure two different quantities: the angular velocity $\omega_m(t)$ and the position $\vartheta_m(t)$. In the picture are also reported the two limiters that affects the system inputs, the torque limit and the speed limit.

The plant is controlled using two different control loops. The innermost is the speed loop that is controlled by $C_\omega(z)$, a PID controller which is tuned with the proportional and the integral part. The outermost is the position loop that was controlled by $C_\vartheta(z)$, a PID controller which is tuned with only the proportional part.

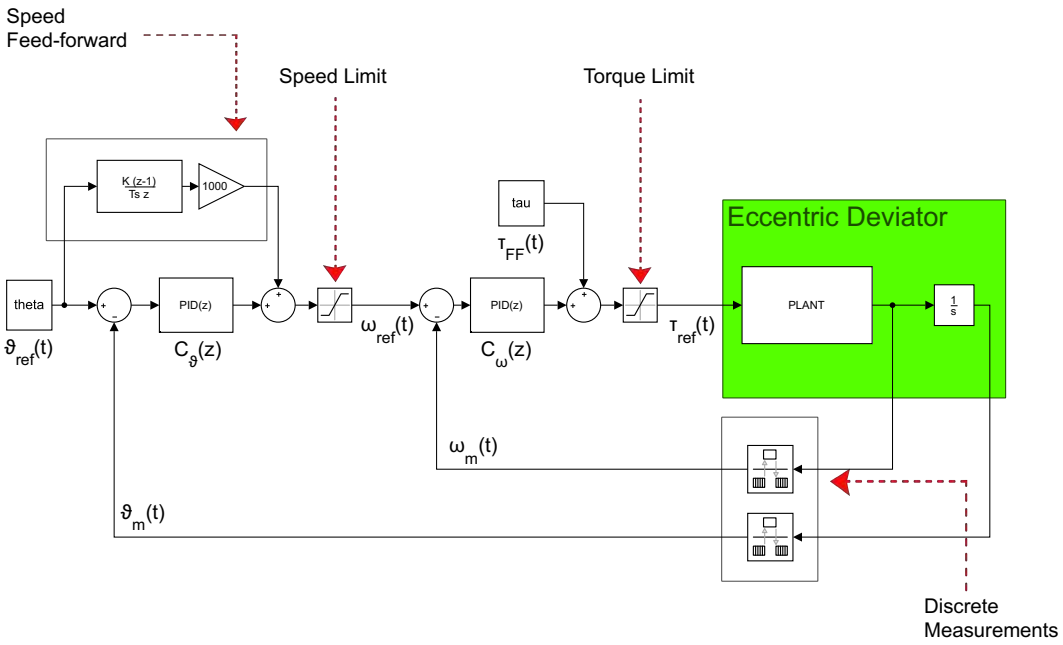

Figure 3.1: Block diagram of the deviator plant: *the two control loops of the system are shown along with their limiters and feed-forward actions. The eccentric deviator is showed in the green box (the presence of the known integrator is also highlighted).*

Since the eccentric deviator is used to move loads with a high inertia, to overcome the problem of the motor's size, the company fed the system with a feed-forward action that adds the desired speed to the output of $C_\vartheta(z)$, this bonds the system to a maximum instant speed that prevents possible overcharge on the motor. Moreover, the torque feed-forward input τ_{FF} was added to improve the performances of the system response.

The main goal of this thesis, as it was introduced before, was the design of a new control law for the eccentric deviator. The first focus was put on the design of the position controller, which previously was tuned by some experimental tests and used without changes for all the different configurations under which the system is used. Secondly, the focus was moved onto the design of a new feed-forward torque input (τ_{FF}). This was possible by simulating the identified models with the MATLAB SIMULINK environment that permitted a quick and easy analysis of the results without the necessity of performing a test for every proposed input. The only minor problem was that it needed some work to write a suitable CODESYS implementation of the new input on the deviator's drive.

Notice that, two different models needed to be identified: the one that was fed up by the position loop (in Fig. 3.1 the closed loop of the speed control plus the integrator) and the one that was fed up by the speed loop (only the "*Plant*" block on Fig. 3.1). For the first identification set-up it was used as input $\mathbf{u}(t)$ the speed $\omega_{ref}(t)$ and as output $\mathbf{y}(t)$ the measured position $\vartheta_m(t)$; for the second identification set-up it was used as input $\mathbf{u}(t)$ the

torque $\tau_{ref}(t)$ and as output $\mathbf{y}(t)$ the measured angular velocity $\omega_m(t)$. All the quantities mentioned before were collected into datasets with length $N = 29990$ with sempling time equal to $T = 500\ \mu s$.

As it has been noticed in Chapter 1, the deviator changes its configuration with respect to the product that the entire plant is currently manufacturing. This change has a visible impact on the eccentric deviator performance which cannot be easely embedded in the system description because it would take a lot of external work and it is not an easy and automatic procedure to perform. One of the thesis objective was to find an easy and hopefully automatic procedure to handle these situations and. As it will be shown in the next sections, computing the identification procedure for different configuration of the system can give interesting results which can be used as a starting point for future works.

As it was said before, the different configuration of the plant are caused by the different type of ferrule attached to the end of the deviator's tube and, their contribute is essentially a change on the value of the total inertia that the brushless motor moves during a movement. In this thesis, the following configurations have been analysed:

- **Configuration A**: tests performed with the commonly used ferrule. This is the lighter ferrule among all the different ones that are used by the SMS group;
- **Configuration B**: tests performed with a ferrule that was approximately $2.7095\,kg$ heavier of the commonly used ferrule. To add this weight it was used a cylindrical piece of metal to simulate the change of installed ferrule since, at that time, there was not a set of different ferrule in the facilities.

To see whether the System Identification is a valid tool for the implementation of an automatic and flexible controller, the identification procedure described above was performed for each configuration and each control loop. This was done principally to see if was possible to identify how the system changes from one configuration to another or, at least, to have a rough idea on how to distinguish different configuration of the deviator. Once all the results have been acquired, an analysis will be carried out on the possible advantages of using System Identification methods with respect to the modellization based on the physics.

An important fact to keep in mind is that, unfortunately, the drive was not able to acquire more than four traces of data. For this reason, during the identification tests the acquired traces were $\omega_{ref}(t)$, $\tau_{ref}(t)$, $\omega_m(t)$ and $\vartheta_m(t)$. Instead, for the comparison with the underlying system or other analysis the monitored signals where usually $\vartheta_{ref}(t)$, $\tau_{ref}(t)$, $\tau_m(t)$ and $\vartheta_m(t)$. Moreover, for the final analysis on the performances of the new control laws and the comparison with the physical modellization the acquired traces were $\vartheta_{ref}(t)$, $\vartheta_m(t)$, $\tau_{ref}(t)$ and $\tau_m(t)$; this was done to give a clearer view on why the control law is a better option than the classic one.

3.2 Input Design

An important step is to set up the right conditions to perform the System Identification procedure. One of the most important task is to design an input that is capable of

effectively excite the system. More specifically, the input $\mathbf{u}(t)$ should be a periodic signal with a spectrum rich in frequency components, something that is usually not possible in some industrial plant. Another important design aspect of $\mathbf{u}(t)$ is that it should be high in magnitude so that the disturbances doesn't affect too much the identification of the plant.

Notice that, up until now, the focus was put only on $\mathbf{u}(t)$ forgetting that usually, the signal $\mathbf{u}(t)$ is constrained by the relation $\mathbf{u}(t) = \mathcal{H}(z)\mathbf{y}(t) + w(t)$. So, the task must be modified . More precisely the only input that can be designed is the reference signal $w(t)$ which makes the task even harder. As it will be clear shortly, the design of an optimal $\mathbf{u}(t)$ will be relatively easy only for the position loop identification since it can be designed using the feed-forward speed input. Unfortunately, for the speed loop, $w(t)$ is completely regulated by the two control loop and this implies that input cannot be designed at all.

As it has been already noticed, the SMS Group uses a speed feed-forward action to help the system stay inside its limitations. More specifically, this implied an indirect design of the input $w(t =)\vartheta_{ref}(t)$. In particular, the angular position reference were calculated by solving the inverse kinematics of specific speed profiles. Therefore, given a desired speed profile $\omega_{des}(t)$, the input $\vartheta_{ref}(t)$ was calculated as follows:

$$\vartheta_{ref}(t) = \vartheta_{ref}(0) + \omega_{des}(0)t + \frac{1}{2}\mathrm{a}(t)t^2 \tag{3.1}$$

where $\mathrm{a}(t)$ is the instantaneous acceleration which is a piecewise constant signal since $\omega_{des}(t)$ is composed by a prefixed number of ramps with different angular coefficient (i.e. various desired acceleration of the system). As it is clear, this helped a lot during the design of a suitable input for the identification procedure because, as it will be shown later, the input $\mathbf{u}(t)$ that is created during a movement was very similar to the designed $\omega_{des}(t)$.

Obviously there were some limitations on the possible movements that could be performed that derived from the application of the eccentric deviator or the brushless motor constrains. The only limitation imposed by the motor was that the maximum angular velocity it had to be less than the nominal speed $\Omega_N = 1500\,\mathrm{rpm}$. On the other hand, the permitted movements were restricted by the application between a minimum angle $\vartheta_{min} = -20^\circ = -\frac{1}{9}\pi\,\mathrm{rad}$ and a maximum angle $\vartheta_{max} = 200^\circ = \frac{10}{9}\pi\,\mathrm{rad}$ even though movements with this wide angle were particular case and were used only for special configurations of the deviator. Furthermore, the usual movement is restricted between angles equals to $\vartheta_{min} = 0\,\mathrm{rad}$ and $\vartheta_{max} = \pi\,\mathrm{rad}$. This type of movement was also used for the identification tests on the eccentric deviator.

The first problem that derived from the common application of the deviator was that it performed a movement after an approximative delay equal to $T_{delay} = 2\,s$[1] and the movement command was acquired from the plant. Obviously, this downtime was far to be optimal for the identification problem and so, to solve this it was developed a program that started the inverse movement after a delay equal to $T_{delay} = 2\,ms$ from the acknowledgement of final position reached for a prefixed number of times. As it will be clear later, sometimes this small delay was not sufficient and this leaded to some

[1]For example if a movement is performed at a time t_1 the inverse movement will start at $t_2 = T + T_{delay}$ where T is the time needed to perform a movement.

sub-optimal estimate of the analysed configuration. To see if low performances were a consequence of a non-optimal input in Chapter 5 there will be an analysis where the PEM estimate was performed with a dataset where $\vartheta(t)$ had a delay with respect to the movement equal to $T_{delay} = 0\,s$.

Passing now on a more specific description, Fig. 3.2 shows the input used to obtain the dataset used to perform the PEM estimate. This signal was designed in the same way of the quickest profile used by the company for their application. Furthermore, the pictures shows the desired speed signal (Fig. 3.2(a)) and the calculated position input $\vartheta(t)$ (Fig. 3.2(b)). From now on, this profile will be referred as *Reg*, abbreviation of Regular. Moreover, as it can be seen in Fig. 3.2(b), the reported signal is designed for a movement that starts from $\vartheta_{ref_{Reg}}(0) = 0\,\text{rad}$ and ends at an angle equal to $\vartheta_{ref_{Reg}}(T_{Reg}) = \pi\,\text{rad}$. Clearly, if the system has to do the inverse movement, the plot in Fig. 3.2(b) will be reversed and it will start from π and end with the reference at 0. Moreover, the plot in Fig. 3.2(a) will be mirrored with respect to the time axis.

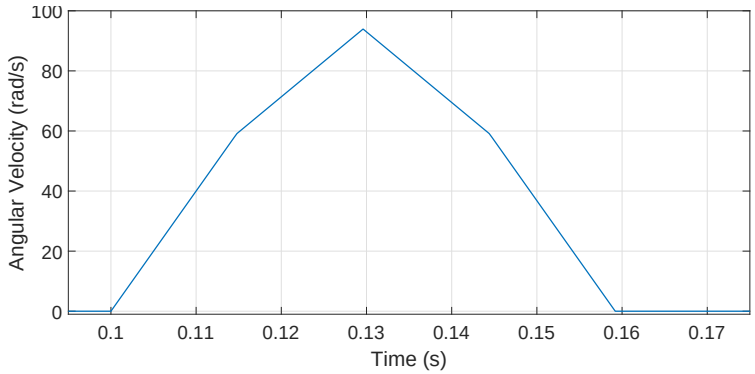

(a) Desired angular velocity $\omega_{des_{Reg}}(t)$.

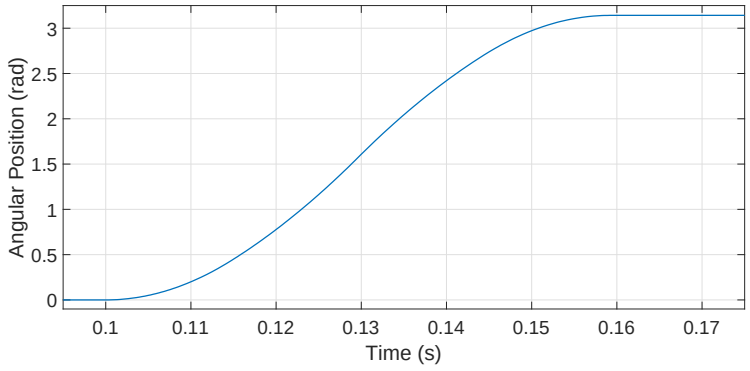

(b) Position input $\vartheta_{ref_{Reg}}(t)$.

Figure 3.2: Regular input profile: *in Fig. 3.2(a) the desired speed reference, in 3.2(b) the position profile calculated by solving the inverse kinematic.*

This profile has a total duration of $T_{Reg} = 59.2\,ms$ and, as it can be seen in Fig. 3.2(a), its speed profile is symmetric with respect to the middle point of the movement $\frac{T_{Reg}}{2} = 29.6\,ms$. Another thing that can be noted on the picture are the different ramps that defines the signal $\omega_{ref_{Reg}}(t)$. The characteristics of the four ramps are showed in Table 3.1 and refers for a signal that goes from 0 to π: to obtain the inverse movement

the only thing to do is to invert the acceleration column and put a minus on all the angular velocity reported.

Table 3.1: Ramps characteristics.

Ramp	Angular Velocity				Acceleration	Duration	Computed Angle	
	Starting		Final					
	rpm	$\frac{\text{rad}}{s}$	rpm	$\frac{\text{rad}}{s}$	$\frac{\text{rad}}{s^2}$	ms	$\circ$	rad
First	0	0	564.19	59.08	4000	14.77	25°	$\frac{5}{36}\pi$
Second	564.19	59.08	896.95	93.93	2350	14.82	65°	$\frac{13}{36}\pi$
Third	896.95	93.93	564.19	59.08	-2350	14.82	65°	$\frac{13}{36}\pi$
Fourth	564.19	59.08	0	0	-4000	14.77	25°	$\frac{5}{36}\pi$

Another key aspect on the input design is the values which takes the controller of the system. More specifically, since the controller plays an active role on the construction of the input $\mathbf{u}(t)$ used for the identification procedure, it should guarantee a good excitement of the system in order to produce an input that satisfy the constrains imposed by the System Identification procedure. In other words, the controller used for the identification tests should have the same performances of the one that guarantee an optimal response of the system. For the identification of the deviator the values of two controllers were the same that were tuned by the engineers of the SMS Group during their test on the machine. In Equation (3.2) are reported these two controllers:

$$\begin{aligned} C_\omega(z) &= K_{P_\omega} + \tfrac{K_{I_\omega}}{z-1} = 0.4 + \tfrac{1}{z-1} \\ C_\vartheta(z) &= K_{P_\vartheta} = 450. \end{aligned} \tag{3.2}$$

As it was said in Section 2.4 to ease the search of the optimal model it is useful to collect dataset with different inputs to see if the identified model can fully explain the underlying system. Using some input already designed and used by the SMS Group, the following inputs were considered:

- Medium (*Med*): a profile similar to the Regular one but with a longer duration $T_{Med} = 71,79\,ms$ and a lower maximum speed. In red in Fig. 3.3;
- Trapeze (*Trp*): a slow profile with only three ramps in which the second ramp is with an acceleration equal to zero. In yellow in Fig. 3.3;
- Run-Up (RU): a profile that starts at $\vartheta_{ref}(0) = -20°$ and ends at $\vartheta_{ref}\,(T_{RU}) = 200°$. In purple in Fig. 3.3. This input was used only to compare the estimated model performances with the system response.

All the considerations of the previous paragraph are valid also for all the validation inputs. The detail of all the profiles can be found in Appendix A since it would take a lot of space and it is not a key argument of the thesis.

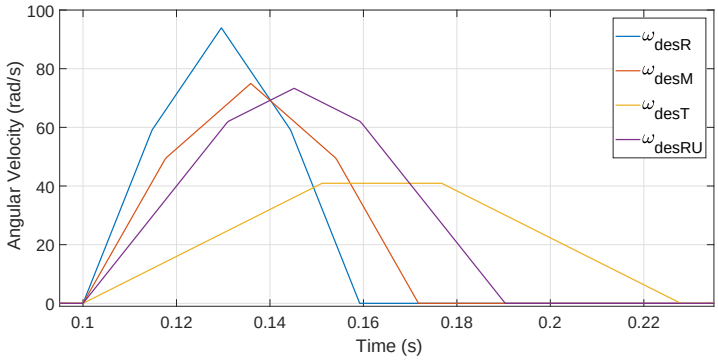

(a) Desired angular velocity $\omega_{des}(t)$.

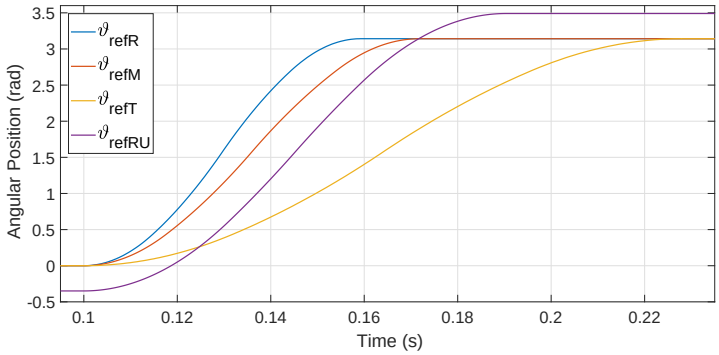

(b) Position input $\vartheta_{ref}(t)$.

Figure 3.3: Validation input profiles: *in blue the Regular profile, in red the Medium profile, in yellow the Trapeze profile and in purple the Run-Up profile. In Fig 3.3(a) are reported the desired angular velocity profiles and in Fig. 3.3(b) are reported the calculated position inputs. Notice that the Run-Up input (purple) doesn't start at* 0 *and end at* π.

As it has been said before, all these inputs were designed form different existing speed profiles used by the SMS Group in fact, slower inputs with lower values of acceleration are generally used when the installed ferrule is heavier than the one used in configuration A.

To produce meaningful datasets for the Cross-Validation technique, the following sets of data were collected for each configuration:

- Med_60: A dataset obtained performing 60 consecutive movements with a delay of $2\,ms$ with input the Medium profile.
- Trp_60: A dataset obtained performing 60 consecutive movements with a delay of $2\,ms$ with input the Trapeze profile.
- 03_60: A dataset obtained performing 40 consecutive movements with input the Regular profile followed by 20 movements with input the Trapeze profile, all of them executed with a delay of $2\,ms$.

It can be noted that those three datasets have different dynamics. In fact the first two set of data have a slower and easier movement which implies a higher period of the

generated signal ($T_{P_{Med}} \approxeq 150\,ms$ for the Medium and $T_{P_{TRP}} \approxeq 260\,ms$ for the Trapeze). On the other hand, the dataset 03_60 mixes a part where the dynamic of the signal is high and a part with a slow dynamic. This implies that is the most challenging.

Since the task of this thesis was to identify the model without external actions, during the tests, the torque feed-forward action $\tau_{FF}(t)$ was always setted to zero.

3.3 Model Structure Design and Validation Procedure

Since the knowledge on the deviator system was limited, it could not be possible to make some preliminary assumption on the structure of $\mathcal{M}$. The best guess that could be made was to perform the PEM estimate for ten model structures. The total starting degree of all the position loop was equal to 4 and for the speed loop it was equal to 3. This difference was due to the fact that, in the position loop identification, it was added the known part of $\mathcal{F}_{known}(z)$ as described in Section 2.1.

Due to the high number of proposed models the validation was split into two parts. The first part consisted in a comparison among all the models that belong to the same model classes OE, ARX, ARMAX and BJ. The comparison was performed in the following way:

1. By looking at the zero-pole all the models with evident or close zero-pole cancellation were excluded;

2. By looking at the Cross-Validation test performed with the Medium dataset the less performing models were discarded;

3. By looking at the Residual Analysis the less performing models were discarded;

4. If there were too many models after this procedure, after a final look to the AIC and BIC terms, the process was repeated.

Usually, after this preliminary procedure, four models were selected and the above steps were was repeated to find the optimal model $\mathcal{M}_{OPT}\left(\hat{\theta}_{Pem}\right)$. In this the Cross-Validation test was performed using also the other datasets.

Since all the OE models performed poorly in all the identification procedure, in this thesis their plots are not going to be examined or analysed.

Moreover, due to the high quantity of plots produced during the first validation, only the plots regarding the second procedure are going to be analysed in this thesis. It is recommended, to have a clearer view, to consult the MATLAB file and all the generated plot which is available upon request.

3.4 Configuration A: Identification Results

3.4.1 Position Loop

The scope of this Section is to explain and analyse the results obtained form the identification of the model fed up by the position loop when the deviator is used with configuration A. In Fig. 3.4 it is showed a segment of the acquired dataset used for the training step. In Fig. 3.4(a) it is reported the speed reference $\omega_{ref}(t)$ in blue (used for the identification of the model) and in red it is plotted the measured speed $\omega_m(t)$ used for the identification treated in the next section. In Fig. 3.4(b) the angular position response $\vartheta_m(t)$ of the system is showed[2]. Notice that, the output of the system is affected by a significant overshoot that can be observed even without the presence of the reference signal on the plot.

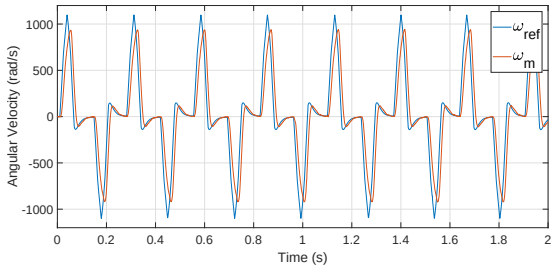

(a) Reference signal $\omega_{ref}(t)$ in blue and measured signal $\omega_m(t)$ in red.

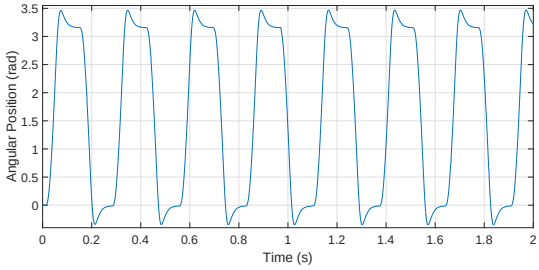

(b) Measured signal $\vartheta_m(t)$

Figure 3.4: Segment of the Regular dataset with configuration A: *in Fig 3.4(a) it is showed the speed reference $\omega_{ref}(t)$ and the system speed response $\omega_m(t)$, in Fig. 3.4(b) it is showed the measured system position $\vartheta_m(t)$.*

As it was said before, here it is reported be only the second part of the validation analysis. The four model structures are:

- $\mathcal{M}^A_{ARX_{11}}$: ARX model structure with number of parameters[3] $n_A = n_B = 11$ and $n_k = 1$;
- $\mathcal{M}^A_{ARMAX_{11}}$: ARMAX model structure with number of parameters $n_A = n_B = n_C = 11$ and $n_k = 1$;
- $\mathcal{M}^A_{BJ_7}$: BJ model structure with number of parameters $n_B = n_C = n_D = n_F = 7$ and $n_k = 1$;
- $\mathcal{M}^A_{BJ_{10}}$: BJ model structure with number of parameters $n_B = n_C = n_D = n_F = 10$ and $n_k = 1$.

[2]Here it is reported only the measured angular position due to the limited amount of data traces that the drive was capable of storing during the movements.

[3]Here it is included also the integral part which has been added in the data processing step.

Starting with the zero-pole cancellation test, it can be seen in Fig. 3.5 that all the models were chosen without exact zero-pole cancellation. The only notable thing to highlight is the presence of a close zero-pole cancellation in the proximity of 0 in model $\mathcal{M}^A_{ARMAX_{11}}$ (in red on Fig. 3.5(a)). It can be noted that all the models are without poles outside the unit circle (the grey dashed line). Furthermore, $\mathcal{M}^A_{ARMAX_{11}}$ is the model which has the highest number of poles close to the unitary circle.

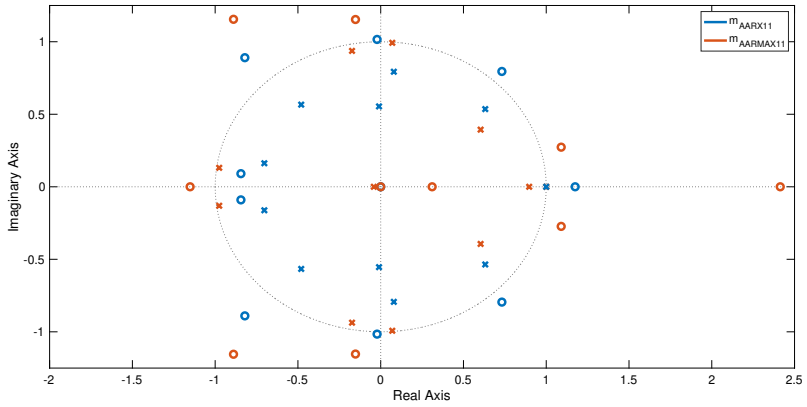

(a) Zero-pole diagram of models $\mathcal{M}^A_{ARX_{11}}$ (blue) and $\mathcal{M}^A_{ARMAX_{11}}$ (red)

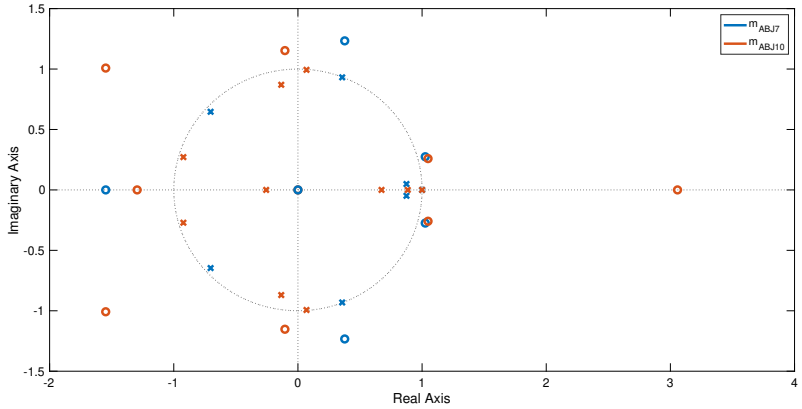

(b) Zero-pole diagram of models $\mathcal{M}^A_{BJ_7}$ (blue) and $\mathcal{M}^A_{BJ_{10}}$ (red)

Figure 3.5: Zero-pole diagram estimated models with configuration A: *in Fig. 3.5(a) models* $\mathcal{M}^A_{ARX_{10}}$ *(blue) and* $\mathcal{M}^A_{ARMAX_8}$ *(red). In Fig. 3.5(b) models* $\mathcal{M}^A_{BJ_7}$ *(blue) and* $\mathcal{M}^A_{BJ_{10}}$ *(red). All the models are without exact zero-poles cancellation and all of them have a zero in* $z_0 = 0$ *and a pole in* $p_0 = 1$ *derived by the added integrator.*

Another thing to note is the presence, in all the four models, of a pole in $p_0 = 1$ and a zero in $z_0 = 0$. This is caused by the presence of the known part in $\mathcal{F}(z)$ which, as it was said before, has the form of a discrete integrator which forces the presence of z_0 and p_0.

Passing on the Complexity Terms test, the results are reported in (3.3). As it can be seen, both the AIC and BIC give almost the same results. By looking at the performances of the different models it can be seen that the two model structures that better perform are $\mathcal{M}^A_{ARMAX_{11}}$ and $\mathcal{M}^A_{BJ_{10}}$ with a difference that is almost insignificant in both terms.

$$
\begin{aligned}
J_{AIC}\left(\mathcal{M}^{A}_{ARX_{11}}\right) &= -1.225 & J_{BIC}\left(\mathcal{M}^{A}_{ARX_{11}}\right) &= 4.862 \cdot 10^{4} \\
J_{AIC}\left(\mathcal{M}^{A}_{ARMAX_{11}}\right) &= -1.349 & J_{BIC}\left(\mathcal{M}^{A}_{ARMAX_{11}}\right) &= 4.491 \cdot 10^{4} \\
J_{AIC}\left(\mathcal{M}^{A}_{BJ_{7}}\right) &= -1.342 & J_{BIC}\left(\mathcal{M}^{A}_{BJ_{7}}\right) &= 4.505 \cdot 10^{4} \\
J_{AIC}\left(\mathcal{M}^{A}_{BJ_{10}}\right) &= -1.348 & J_{BIC}\left(\mathcal{M}^{A}_{BJ_{10}}\right) &= 4.497 \cdot 10^{4}.
\end{aligned}
\tag{3.3}
$$

The results obtained with the Complexity Terms tests are confirmed by the Residual Analysis plot reported in Fig. 3.6. As it will be clear at the end of this chapter, this similarity is present in all the identification procedure performed in this thesis.

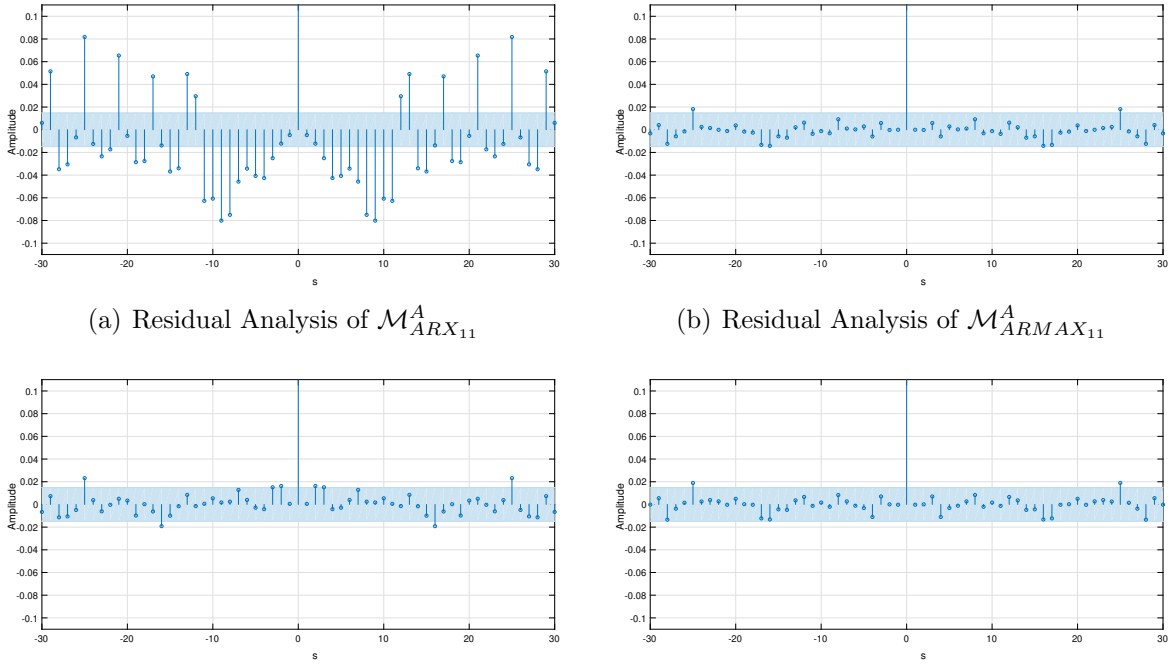

(a) Residual Analysis of $\mathcal{M}^{A}_{ARX_{11}}$

(b) Residual Analysis of $\mathcal{M}^{A}_{ARMAX_{11}}$

(c) Residual Analysis of $\mathcal{M}^{A}_{BJ_{7}}$

(d) Residual Analysis of $\mathcal{M}^{A}_{BJ_{10}}$

Figure 3.6: Residual Analysis of the estimated position loop models with configuration A: *the light blue area is the confidence region that* $r_{\varepsilon_{\hat{\theta}_{PEM}}}(s)$ *should not exceed. As it can be seen Fig. 3.6(a), model* $\mathcal{M}^{A}_{ARX_{11}}$ *is the one that has the poorest performances among all. On the other hand* $\mathcal{M}^{A}_{ARMAX_{11}}$ *(Fig. 3.6(b)) and* $\mathcal{M}^{A}_{BJ_{11}}$ *(Fig. 3.6(d)) have a nearly optimal plot.*

From the picture it is clear that $\mathcal{M}^{A}_{ARX_{11}}$ has the worst performances overall since its residuals $r_{\varepsilon_{\hat{\theta}_{PEM}}}(s)$ are mostly outside the confidence region. On the other hand, for the other three model structures, it is difficult to have a clearer view than the one that was previously obtained with the Complexity Terms tests.

It is clear that, with only those three validation tests, the decision of the optimal model $\mathcal{M}_{OPT}(\hat{\theta}_{PEM})$ is trivial. The Cross-Validation technique can help distinguish the dereferences among models and obtain a clearer answer to the problem. Figure 3.7 shows a small part of the prediction error $\varepsilon^{Med}(t) = \vartheta_m(t) - \hat{\vartheta}_m(t)$ obtained with the Cross-Validation test performed with the Med_60 validation dataset. As it can be clearly seen,

it is hard to give an answer. The only thing that can be possibly said is that $\mathcal{M}^A_{ARX_{11}}$ is the model that has the best performances but this is only a rough analysis.

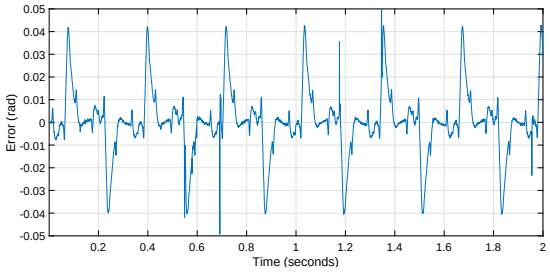

(a) Plot of the error $\varepsilon^{Med}_{ARX_{11}}(t)$ of model $\mathcal{M}^A_{ARX_{11}}$

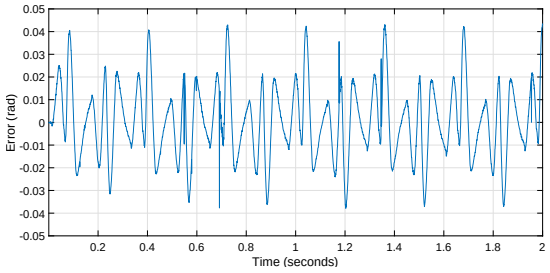

(b) Plot of the error $\varepsilon^{Med}_{ARMAX_{11}}(t)$ of model $\mathcal{M}^A_{ARMAX_{11}}$

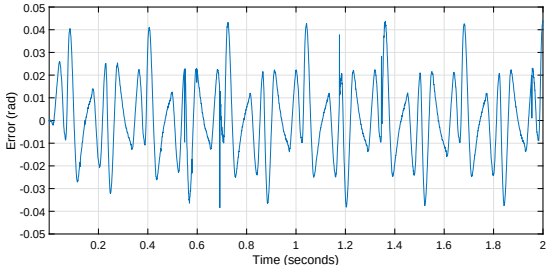

(c) Plot of the error $\varepsilon^{Med}_{BJ_7}(t)$ of model $\mathcal{M}^A_{BJ_7}$

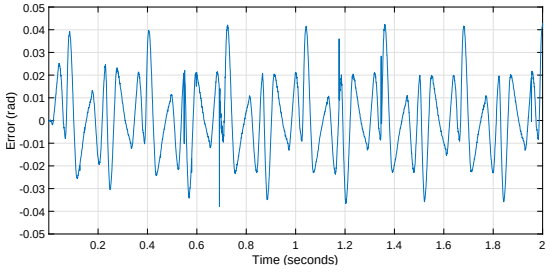

(d) Plot of the error $\varepsilon^{Med}_{BJ_{10}}(t)$ of model $\mathcal{M}^A_{BJ_{10}}$

Figure 3.7: Plot of $\varepsilon^{Med}(t)$ for the estimated position loop models in configuration A: *as it can be seen, these plots are difficult to read and the only consideration that can be done is that* $\mathcal{M}^A_{ARX_{11}}$ *(Fig. 3.7(a)) has the best performances over all but it can be said more than this.*

On the other hand, there is another way to evaluate the Cross-Validation results. More specifically, the Fit term can be used to classify the model performances during the Cross-Validation test. In (3.4) the Fit terms of the four models are reported:

$$\begin{aligned} \text{Fit}_{Med}\left(\mathcal{M}^A_{ARX_{11}}\right) &= 98.998\% \quad \text{Fit}_{Med}\left(\mathcal{M}^A_{ARMAX1}\right) = 98.799\% \\ \text{Fit}_{Med}\left(\mathcal{M}^A_{BJ_7}\right) &= 98.752\% \quad \text{Fit}_{Med}\left(\mathcal{M}^A_{BJ_{10}}\right) = 98.792\%. \end{aligned} \tag{3.4}$$

The first notable thing is that, as it was supposed by looking at Fig. 3.7, the best model for this dataset is $\mathcal{M}^A_{ARX_{11}}$ and is followed by $\mathcal{M}^A_{ARMAX11}$. Moreover, this result is in contrast with what it was derived with the Complexity Terms or the Residual Analysis test, since previously $\mathcal{M}^A_{ARX_{11}}$ and $\mathcal{M}^A_{ARMAX1}$ were the worst models. Another notable thing is that the percentage of all the $\mathring{Fit}$ terms are good but, as it will be clear later, this result is not optimal. Furthermore, the ranking obtained with this first dataset is confirmed also for the Trp_60 set of data. As before the error $\varepsilon^{Trp}(t)$ plot is not so meaningful and so only the Fits terms of each model are reported. All the plots can still be consulted on the MATLAB file which is available upon request.

$$\begin{aligned} \text{Fit}_{Trp}\left(\mathcal{M}^A_{ARX_{11}}\right) &= 99.291\% \quad \text{Fit}_{Trp}\left(\mathcal{M}^A_{ARMAX11}\right) = 99.067\% \\ \text{Fit}_{Trp}\left(\mathcal{M}^A_{BJ_7}\right) &= 99.02\% \quad \text{Fit}_{Trp}\left(\mathcal{M}^A_{BJ_{10}}\right) = 99.048\%. \end{aligned} \tag{3.5}$$

As it was already said, with the Trp_60 dataset the best model is still $\mathcal{M}^A_{ARX_{11}}$ followed again by $\mathcal{M}^A_{ARMAX11}$. It is reminded to the reader that those two dataset were the ones with the slowest dynamic in fact, as it can be seen in Fig. 3.3(a). On the other hand, if the focus is moved on a more informative dataset, like the 03_60 set of data, the result is different:

$$\begin{aligned} \text{Fit}_{03}\left(\mathcal{M}^A_{ARX_{11}}\right) &= 98.319\% \quad \text{Fit}_{03}\left(\mathcal{M}^A_{ARMAX11}\right) = 98.772\% \\ \text{Fit}_{03}\left(\mathcal{M}^A_{BJ_7}\right) &= 98.716\% \quad \text{Fit}_{03}\left(\mathcal{M}^A_{BJ_{10}}\right) = 98.782\%. \end{aligned} \tag{3.6}$$

With the results reported in (3.6) the best models are $\mathcal{M}^A_{BJ_{10}}$ and $\mathcal{M}^A_{ARMAX11}$. Notice that, $\mathcal{M}^A_{ARX_{11}}$ have lost all of its advantage over the other two BJ models. Moreover, the results obtained on the 03_60 dataset confirms what the Residual Analysis and the two Complexity Terms tests showed in the first place. Furthermore, as it was said before, this dataset was the one that most excited the system and a good result on this test should be considered more informative than the ones obtained with the previous two dataset.

Before passing on the final choice of the optimal model for this configuration a quick discussion on the result reported above is needed. As it was showed the Residual Analysis and the two Complexity Terms test give the same results. Furthermore, the two terms are especially useful to obtain a ranking between all the estimated model structures. Passing on the zero-poles plot, it is clear that it is useful tool only in the first part of the analysis, since it was used to discard a lot of the non-optimal models but, as it will be explained shortly, it will be useful also in the final decision of the optimal model. Moreover, in addition to the previous analysis on the Cross-Validation test, it can be seen that the percentage changes significantly between two different datasets. In particular, for the "less dynamic" dataset (Trp_60 and Med_60) all the estimated models have values of the Fit term that can be considered good but not optimal. As it will be clear later on, the Cross-Validation can provide better fits by using a more exciting input. Moreover, as it will be clear at the end of this thesis when the dataset used to perform the identification is acquired using a more exciting input, the Cross-Validation test will provide homogeneus results among all datasets and with percentage which is always above 99%.

Finally, the two candidate for the optimal model were $\mathcal{M}^A_{ARMAX11}$ and $\mathcal{M}^A_{BJ_{10}}$ because those two models obtained good results in all the validation tests. In conclusion, the final choice of the optimal model was put on $\mathcal{M}^A_{BJ_{10}}$ because, as it was said before, it had good performances over all the validation tests and, more importantly, it had the best performance on the more informative dataset. Moreover, in comparison with the other candidate for the optimal model, $\mathcal{M}^A_{ARMAX11}$, it had a simpler structure of $\mathcal{F}(z)$ and it had a better zero-pole plot since it was without zero-pole quasi-cancellation or a high number of poles near the unitary circle.

Figure 3.8 shows a clearer image of the zeros and poles of $\mathcal{M}^A_{BJ_{10}}$. For a more detailed structure of $\mathcal{F}^A_{BJ_{10}}(z)$ it is recommended to consult the MATLAB file which is available upon request.

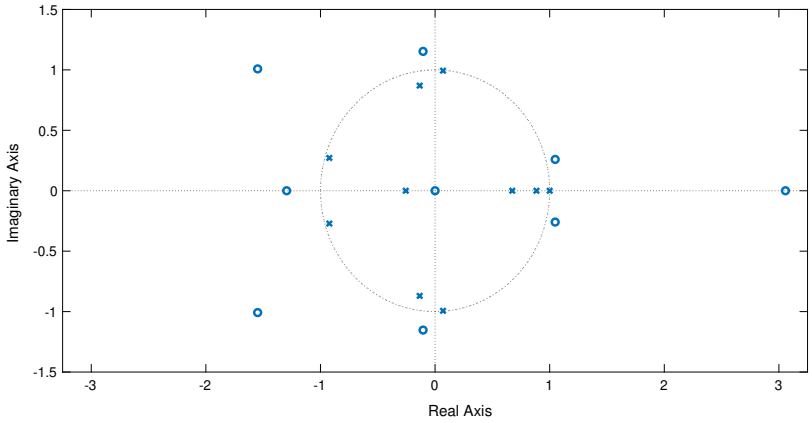

Figure 3.8: Zero-pole diagram of the chosen model $\mathcal{M}^{A}_{BJ_{10}}$ for the position loop identification in configuration A

3.4.2 Speed Loop

The scope of this section is to explain and analyse the results obtained form the identification of the model fed up by the speed loop when the deviator is used with configuration A. Part of the dataset used for the PEM estimate is reported in Fig. 3.9. Here it is showed only the input $\tau_{ref}(t)$ used since the output $\omega_m(t)$ was already reported in Fig. 3.4(a) (red signal). Notice that the signal $\tau_{ref}(t)$ has a more visible error and it is not optimal for the identifications techniques since it has a lot of pieces that are semi-constant, this can imply a poor estimation of the model. Moreover, note also that the maximum requested torque for each movement exceed 200 Nm which is near to the 300% of the nominal torque.

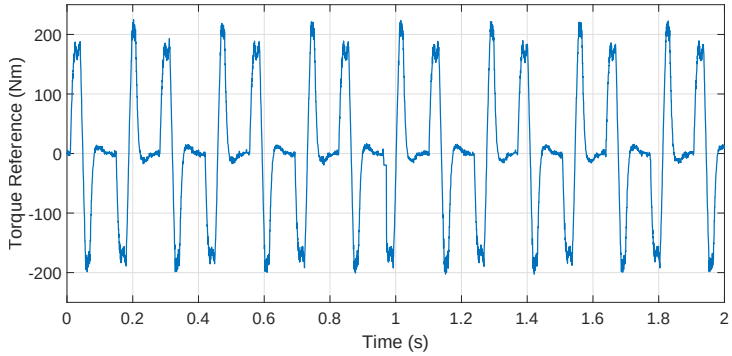

Figure 3.9: Segment of the reference signal $\tau_{ref}(t)$ with configuration A

As in the previous analysis, here it is reported only the second part of the validation analysis. The four model structures are:

- $\mathcal{M}^{A_V}_{ARX_5}$: ARX model structure with number of parameters $n_A = n_B = 5$ and $n_k = 1$;
- $\mathcal{M}^{A_V}_{ARX_7}$: ARX model structure with number of parameters $n_A = n_B = 7$ and $n_k = 1$;
- $\mathcal{M}^{A_V}_{ARMAX_8}$: ARMAX model structure with number of parameters $n_A = n_B = n_C = 8$ and $n_k = 1$;

- $\mathcal{M}_{BJ_{11}}^{A_V}$: BJ model structure with number of parameters $n_B = n_C = n_D = n_F = 11$ and $n_k = 1$.

The zero-pole plot of the different models is showed in Fig. 3.10: all the estimated models are without from zero pole cancellations and, for the two ARX model, even almost without poles near the unitary circle.

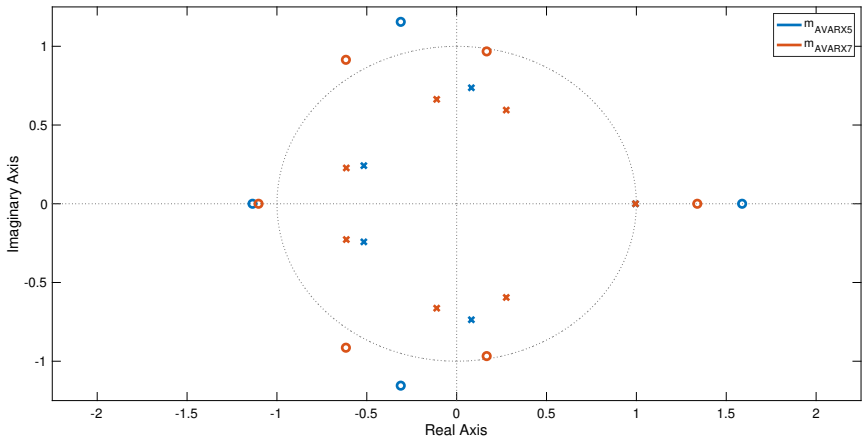

(a) Zero-pole diagram of models $\mathcal{M}_{ARX_5}^{A_V}$ (blue) and $\mathcal{M}_{ARX_7}^{A_V}$ (red)

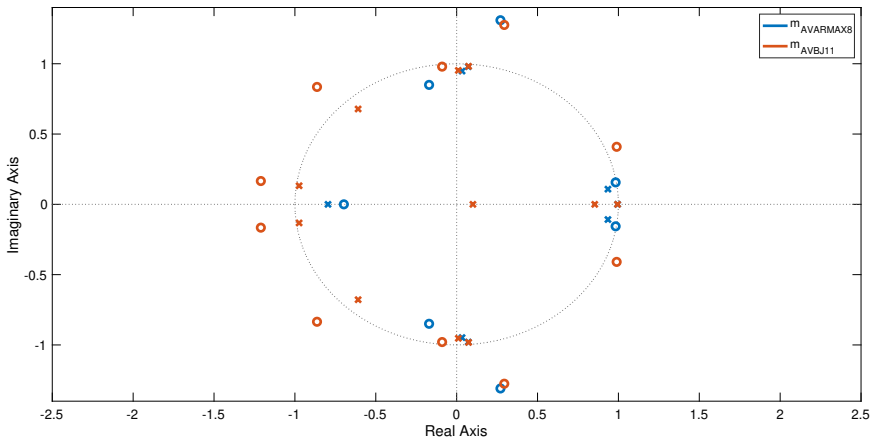

(b) Zero-pole diagram of models $\mathcal{M}_{ARMAX_8}^{A_V}$ (blue) and $\mathcal{M}_{BJ_{11}}^{A_V}$ (red)

Figure 3.10: Zero-pole diagram of the estimated speed loop models with configuration A: *as it can be seen, all the models are free from zero-poles cancellations and, for the models in 3.10(a), even almost from poles near the unitary circle.*

Passing to the more informative part of the validation tests, the AIC and BIC values of all the models are reported below:

$$
\begin{aligned}
J_{AIC}\left(\mathcal{M}^{A_V}_{ARX_5}\right) &= 9.365 & J_{BIC}\left(\mathcal{M}^{A_V}_{ARX_5}\right) &= 3.66 \cdot 10^5 \\
J_{AIC}\left(\mathcal{M}^{A_V}_{ARX_7}\right) &= 9.345 & J_{BIC}\left(\mathcal{M}^{A_V}_{ARX_7}\right) &= 3.656 \cdot 10^5 \\
J_{AIC}\left(\mathcal{M}^{A_V}_{ARMAX_8}\right) &= 9.215 & J_{BIC}\left(\mathcal{M}^{A_V}_{ARMAX_8}\right) &= 3.617 \cdot 10^5 \\
J_{AIC}\left(\mathcal{M}^{A_V}_{BJ_{11}}\right) &= 9.218 & J_{BIC}\left(\mathcal{M}^{A_V}_{BJ_{11}}\right) &= 3.619 \cdot 10^5.
\end{aligned}
\tag{3.7}
$$

The first observation that can be done by looking at the two Complexity Terms is that there is a significant increase of all the AIC and BIC values, this may be consequence of the fact that the signals used for the identification procedure is not suitable to perform the PEM estimate. In (3.7) it can be seen that, as before, both the AIC and BIC terms give the same results, More specifically, $\mathcal{M}^{A_V}_{ARMAX_8}$ and $\mathcal{M}^{A_V}_{BJ_{11}}$ are the two models with the lower values in both terms. Furthermore, as in the previous analysis, this result is confirmed also by the Residual Analysis test which is showed in Fig. 3.11.

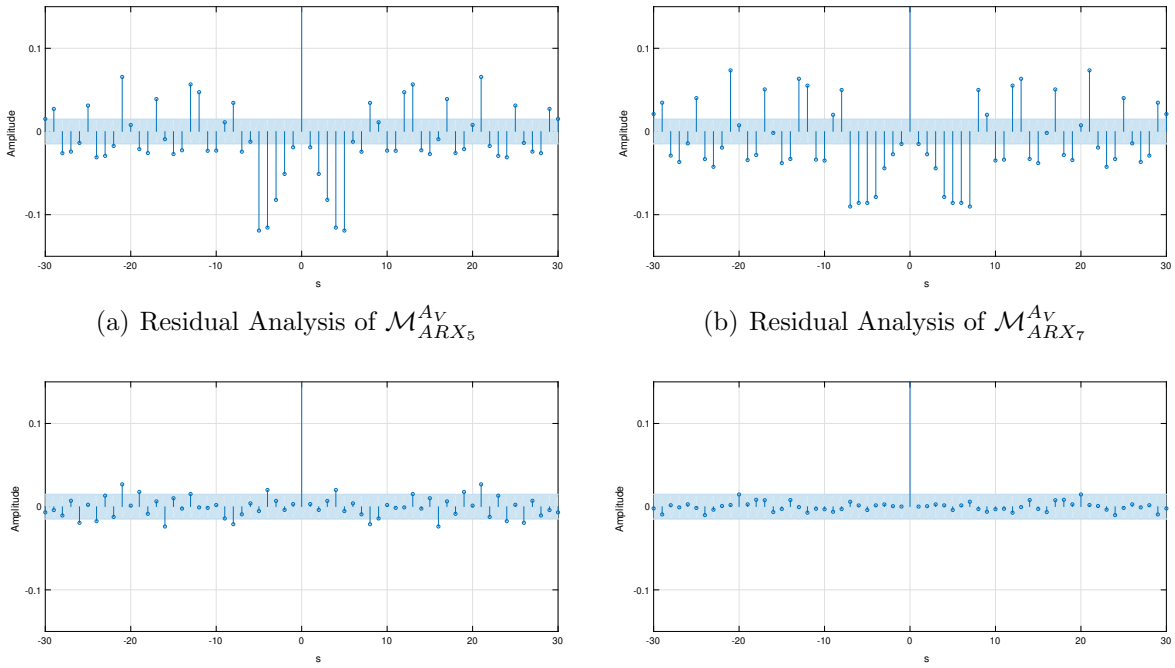

(a) Residual Analysis of $\mathcal{M}^{A_V}_{ARX_5}$

(b) Residual Analysis of $\mathcal{M}^{A_V}_{ARX_7}$

(c) Residual Analysis of $\mathcal{M}^{A_V}_{ARMAX_8}$

(d) Residual analysis of $\mathcal{M}^{A_V}_{BJ_{11}}$

Figure 3.11: Residual Analysis of the estimated speed loop models with configuration A: *the light blue area is the confidence region that* $r_{\varepsilon_{\hat{\theta}_{PEM}}}(s)$ *should not exceed. As it can be seen, the two ARX model structures have a non optimal performances because most of the points are outside the confidence region.*

As before, the residual plot is informative but it does not add useful information for the search of the optimal model. The only thing that can be said is that $\mathcal{M}^{A_V}_{BJ_{11}}$ has a good response to this validation test.

As it was said before, the Cross-Validation plots will not be reported since they are not so informative. In (3.8) the results of the Fit computed with the Medium dataset

terms are reported. The first thing to notice is that, as it was supposed before, there is a significant decrease of the Fit values, even with this dataset that is not challenging like the 03_60 set of data. This is another indicator that shows that the input used is probably not optimal to perform the System Identification:

$$\begin{aligned} \text{Fit}_{Med}\left(\mathcal{M}^{A_V}_{ARX_5}\right) &= 97.916\% \quad \text{Fit}_{Med}\left(\mathcal{M}^{A_V}_{ARX_7}\right) = 97.786\% \\ \text{Fit}_{Med}\left(\mathcal{M}^{A_V}_{ARMAX_8}\right) &= 95.837\% \quad \text{Fit}_{Med}\left(\mathcal{M}^{A_V}_{BJ_{11}}\right) = 96.527\%. \end{aligned} \tag{3.8}$$

Similar to the position loop analysis, with this dataset, the results are opposite with the respect to the ones that were given by the Residual Analysis and the Complexity Terms test. In fact the models that have the best performances are $\mathcal{M}^{A_V}_{ARX_5}$ and $\mathcal{M}^{A_V}_{ARX_7}$. Unlike before, where there were only a difference of 0.5% between the first two and the last two models analysed, here the difference in performances is more sensible. This trend is even more pronounced in the Trp_60 dataset as it can be seen in below:

$$\begin{aligned} \text{Fit}_{Trp}\left(\mathcal{M}^{A_V}_{ARX_5}\right) &= 98.525\% \quad \text{Fit}_{Trp}\left(\mathcal{M}^{A_V}_{ARX_7}\right) = 98.422\% \\ \text{Fit}_{Trp}\left(\mathcal{M}^{A_V}_{ARMAX_8}\right) &= 95.805\% \quad \text{Fit}_{Trp}\left(\mathcal{M}^{A_V}_{BJ_{11}}\right) = 96.636\%. \end{aligned} \tag{3.9}$$

Passing on the final dataset of the Cross-Validation test, the results are pretty much similar as the previous set of data. In fact, as it is showed in (3.10) the situation does not change. This makes the decision for the optimal model harder since there is not an agreement among the different validation procedures. It can be noted that, as in the position loop estimate, the performances of all the models lowered as the dynamics and complexity of the dataset input increased:

$$\begin{aligned} \text{Fit}_{03}\left(\mathcal{M}^{A_V}_{ARX_5}\right) &= 96.931\% \quad \text{Fit}_{03}\left(\mathcal{M}^{A_V}_{ARX_7}\right) = 96.857\% \\ \text{Fit}_{03}\left(\mathcal{M}^{A_V}_{ARMAX_8}\right) &= 95.222\% \quad \text{Fit}_{03}\left(\mathcal{M}^{A_V}_{BJ_{11}}\right) = 95.533\%. \end{aligned} \tag{3.10}$$

Before passing to the optimal model choice, a quick review on the result will be performed. The first discussion is that, as said before, the estimation of this unknown model, with this particular input, is not optimal. This could be deduced by the results on the Complexity Terms and the Cross-Validation tests and clarified in Section 4.1. A possible explanation of the bad result of the identification could be that input was not optimal. More specifically, the bad estimate could derive from the hypnotized not optimality of the position loop input added to the impossibility of choosing the design of the input.

As said before, since the various validation tests give opposite results, the optimal model decision could be difficult. By intuition and since the task, especially for the speed loop, is to find a model that has a response as similar as possible to the real model the choice should be on $\mathcal{M}^{A_V}_{ARX_5}$ or $\mathcal{M}^{A_V}_{ARX_7}$ since they are the two models that have the best performances on the Cross-Validation tests. For reason that will be clear later, the research of the optimal model was restricted instead between $\mathcal{M}^{A_V}_{ARMAX_8}$ and $\mathcal{M}^{A_V}_{BJ_{11}}$. Unfortunately the choice is still a bit difficult since, as in the position loop case, there are

two model that performs almost equally in all the tests but, since $\mathcal{M}_{BJ_{11}}^{A_V}$ had the best residuals plot and had a better performance on the 03_60 dataset, it was chosen as best model for the speed loop estimate in configuration A.

Figure 3.12 shows a clearer image of the zeros and poles of $\mathcal{M}_{BJ_{11}}^{A_V}$. For a more detailed structure of $\mathcal{F}_{BJ_{11}}^{A_V}$ it is recommended to consult the MATLAB file which is available upon request.

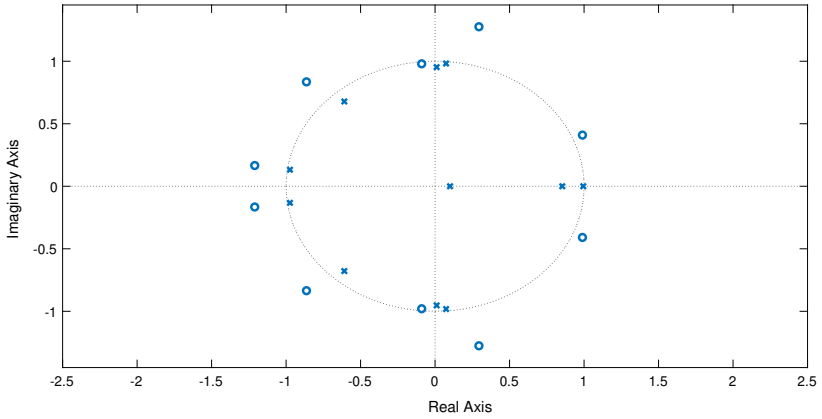

Figure 3.12: Zero-pole diagram of the chosen model $\mathcal{M}_{BJ_{11}}^{A_V}$ for the speed loop identification in configuration A

3.5 Configuration B: Identification Results

3.5.1 Position Loop

The scope of this Section is to explain and analyse the results obtained form the identification of the model fed up by the position loop when the deviator is used with configuration B. In Fig. 3.13 it is showed a segment of the acquired dataset, obtained with the regular input and used for the training step. In Fig. 3.13(a) it is reported the speed reference $\omega_{ref}(t)$ used as input for the identification procedure (blue signal) and the measured angular velocity $\omega_m(t)$ (red signal). The measured angular position $\vartheta_m(t)$ can be seen in Fig. 3.13(b).

By looking at Fig. 3.13(b) the dataset seems identical to yhe one in configuration A but, as it can be seen in Fig. 3.14, the two model responded quite differently even if the input was the same (Regular input) and the wait time after the position reached acknowledgement was identical ($2\,ms$). Notice that, as it can be seen in Fig. 3.14(b) the model in this configuration is affected by a slightly higher overshoot. In Section 3.5.2 it will be showed another aspect that further differentiates the two configurations.

For the position loop in configuration B the following model structures have been selected it the second validation:

- $\mathcal{M}_{ARX_{11}}^{B}$: ARX model structure with number of parameters $n_A = n_B = 1$ and $n_k = 1$;

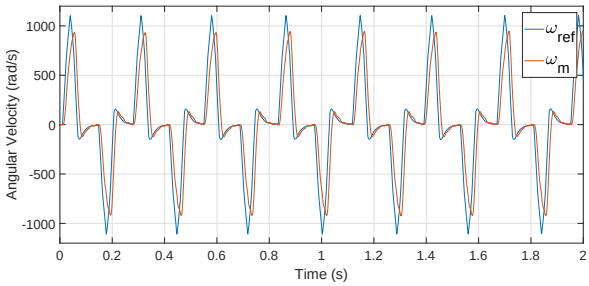

(a) Reference signal $\omega_{ref}(t)$ in blue and measured signal $\omega_m(t)$ in red.

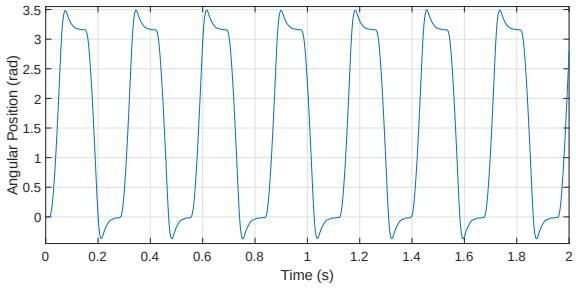

(b) Measured signal $\vartheta_m(t)$

Figure 3.13: Segment of the Regular dataset with configuration B: *in Fig 3.13(a) it is showed the speed reference $\omega_{ref}(t)$ and the system speed response $\omega_m(t)$, in Fig. 3.13(b) it is showed the measured system position $\vartheta_m(t)$.*

- $\mathcal{M}^B_{ARMAX_5}$: ARMAX model structure with number of parameters $n_A = n_B = n_C = 5$ and $n_k = 1$;
- $\mathcal{M}^B_{BJ_9}$: BJ model structure with number of parameters $n_B = n_C = n_D = n_F = 9$ and $n_k = 1$;
- $\mathcal{M}^B_{BJ_{10}}$: BJ model structure with number of parameters $n_B = n_C = n_D = n_F = 10$ and $n_k = 1$.

Figure 3.15 shows the zero-pole plots of all the four models. Like for the position loop estimate in configuration A, it can be noted that all the models have a zero in $z_0 = 0$ and a pole in $p_0 = 1$ that are a direct consequence of the added integrator. Moreover, all the models are without from zero-poles cancellations. As usual this validation method is useful only in the first part to get rid of all the non-optimal models and in the final choice if there are model structures with similar performances.

Starting with the Complexity Terms test, in (3.11) all the values obtained from the models are reported:

$$\begin{aligned} J_{AIC}\left(\mathcal{M}^B_{ARX_{11}}\right) &= -12.05 & J_{BIC}\left(\mathcal{M}^B_{ARX_{11}}\right) &= -2.761 \cdot 10^5 \\ J_{AIC}\left(\mathcal{M}^B_{ARMAX_5}\right) &= -12.11 & J_{BIC}\left(\mathcal{M}^B_{ARMAX_5}\right) &= -2.780 \cdot 10^5 \\ J_{AIC}\left(\mathcal{M}^B_{BJ_9}\right) &= -12.18 & J_{BIC}\left(\mathcal{M}^A_{BJ_9}\right) &= -2.798 \cdot 10^5 \\ J_{AIC}\left(\mathcal{M}^B_{BJ_{10}}\right) &= -12.18 & J_{BIC}\left(\mathcal{M}^B_{BJ_{10}}\right) &= -2.798 \cdot 10^5. \end{aligned} \tag{3.11}$$

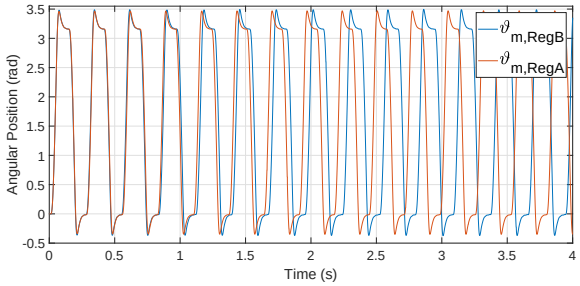

(a) The measured position of the two dataset compared

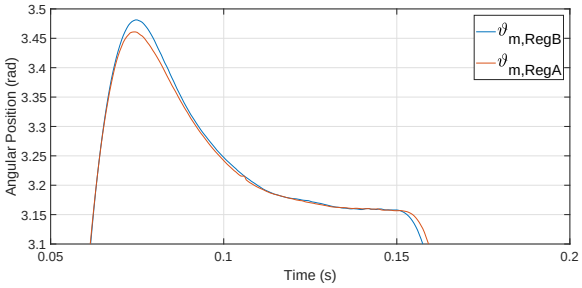

(b) A close up on the peak of the first movement

Figure 3.14: Comparison between the measured position of the model in the two configuration: *in blue the response of the deviator with the configuration B installed and in red the response with the A configuration mounted on the machine.*

The first thing to notice is that, unlike in the speed loop model estimate of configuration A, the values of both Complexity Terms lowered significantly. This could be a sign of a better estimate of the model. The second thing to notice is that there are two models that performs equally ($\mathcal{M}^B_{BJ_9}$ and $\mathcal{M}^B_{BJ_{10}}$). Notice that both the models have a degree of $\mathcal{F}(z)$ equal or close to the one that was chosen for the optimal model in configuration A ($\mathcal{M}^A_{BJ_{10}}$).

Like in the previous validation analysis, the conclusion obtained with the AIC and BIC terms can also be found by looking at the Residual Analysis plots reported in Fig. 3.16. More specifically, it can be observed that the models $\mathcal{M}^B_{BJ_9}$ and $\mathcal{M}^B_{BJ_{10}}$ have an optimal residuals plot. With the decrease of all the Complexity Terms values it correspond to a worsening of the Residual Analysis. It is safe to assume that the optimal model should be searched between these two models and, as it will be clear shortly, this will be confirmed also by the Cross-Validation tests.

Analysing the Cross-Validation results obtained with the different dataset it can be seen that, unlike in the previous cases, only the slowest dataset gives opposite results with respect to the previous validation tests. On the other hand, as it will be showed shortly, there is a significant increment of all the Fit term percentage which are all close to 100%. Furthermore, the Fit terms obtained evaluating the response of the four models with the Medium dataset are here reported:

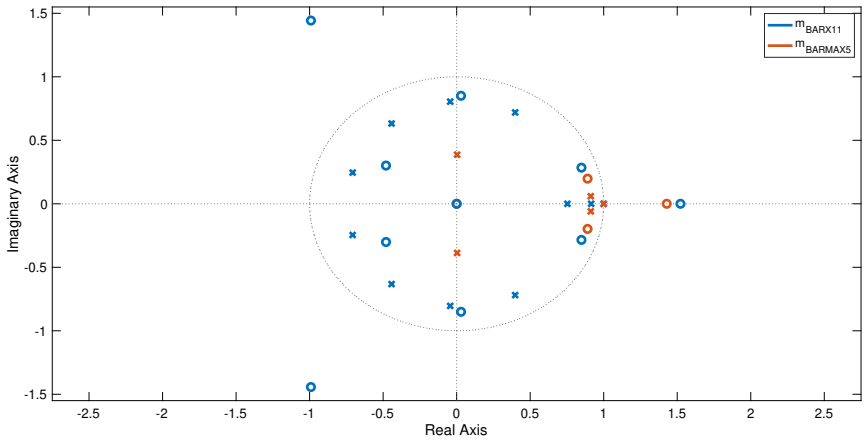

(a) Zero-pole diagram of models $\mathcal{M}^B_{ARX_{11}}$ (blue) and $\mathcal{M}^B_{ARMAX_5}$ (red)

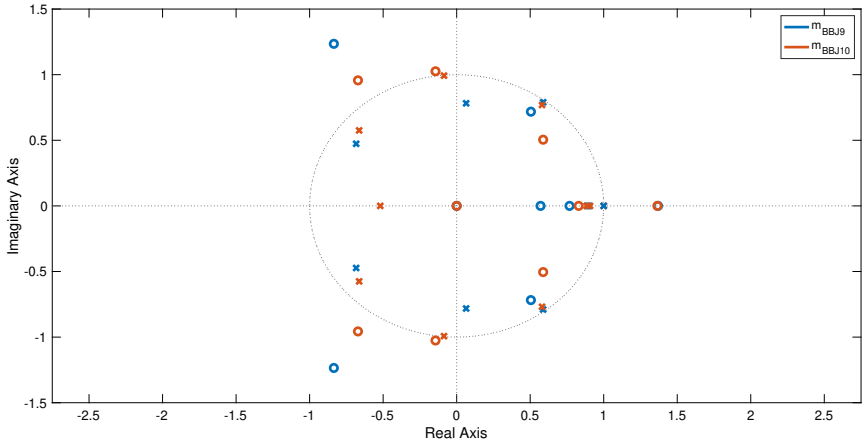

(b) Zero-pole diagram of models $\mathcal{M}^B_{BJ_9}$ (blue) and $\mathcal{M}^B_{BJ_{10}}$ (red)

Figure 3.15: Zero-pole diagram of the estimated position loop models with configuration B: *in Fig. 3.15(a) models* $\mathcal{M}^B_{ARX_4}$ *in blue and* $\mathcal{M}^B_{ARMAX_5}$ *in red. In Fig 3.15(b) models* $\mathcal{M}^B_{BJ_9}$ *in blue and* $\mathcal{M}^B_{BJ_{10}}$ *in red.*

$$\begin{aligned} \text{Fit}_{Med}\left(\mathcal{M}^B_{ARX_{11}}\right) &= 99.855\% \quad \text{Fit}_{Med}\left(\mathcal{M}^B_{ARMAX_5}\right) = 99.86\% \\ \text{Fit}_{Med}\left(\mathcal{M}^B_{BJ_9}\right) &= 99.861\% \quad \text{Fit}_{Med}\left(\mathcal{M}^B_{BJ_{10}}\right) = 99.861\% \end{aligned} \tag{3.12}$$

As it was guessed before, the results that are showed in (3.12) are good and, more importantly, those high percentage shows that all the models can capture the dynamics of the underlying system. Moreover, the Residual Analysis and the Complexity Terms test the provide as best models $\mathcal{M}^B_{BJ_9}$ and $\mathcal{M}^B_{BJ_{10}}$. Moving on the second dataset, the results are the following ones:

$$\begin{aligned} \text{Fit}_{Trp}\left(\mathcal{M}^B_{ARX_{11}}\right) &= 99.471\% \quad \text{Fit}_{Trp}\left(\mathcal{M}^B_{ARMAX_5}\right) = 99.381\% \\ \text{Fit}_{Trp}\left(\mathcal{M}^B_{BJ_9}\right) &= 99.356\% \quad \text{Fit}_{Trp}\left(\mathcal{M}^B_{BJ_{10}}\right) = 99.355\%. \end{aligned} \tag{3.13}$$

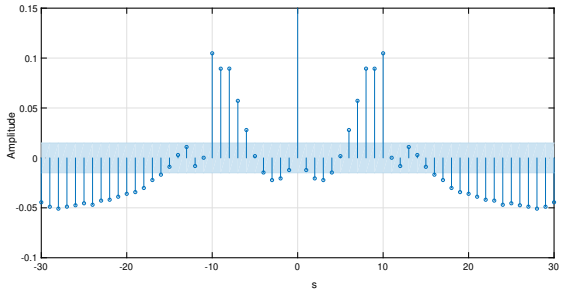

(a) Residual Analysis of $\mathcal{M}^B_{ARX_{11}}$

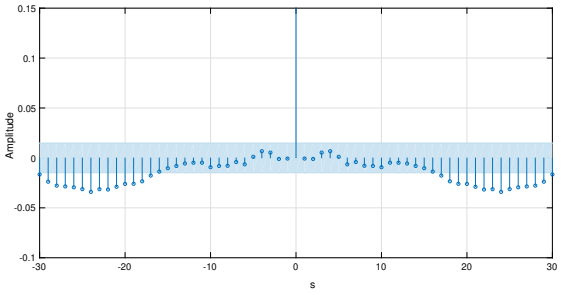

(b) Residual Analysis of $\mathcal{M}^B_{ARMAX_5}$

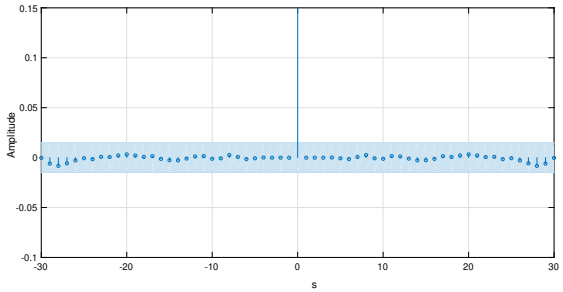

(c) Residual Analysis of $\mathcal{M}^B_{BJ_9}$

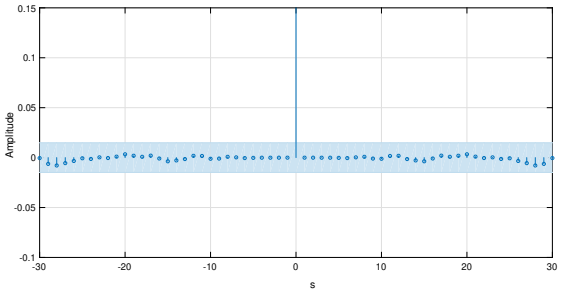

(d) Residual analysis of $\mathcal{M}^B_{BJ_{10}}$

Figure 3.16: Residual Analysis of the estimated models with configuration B: *the light blue area is the confidence region that* $r_{\varepsilon_{\hat{\theta}_{PEM}}}(s)$ *should not exceed. As it can be seen Fig. 3.16(a) model* $\mathcal{M}^B_{ARX_{11}}$ *is the one that has the poorest performances. The other three models (*$\mathcal{M}^B_{ARMAX_5}$, $\mathcal{M}^B_{BJ_9}$ *and* $\mathcal{M}^B_{BJ_{10}}$*) have a nearly optimal residual response.*

As it has been said before, with the Trp_60 dataset, there is a different picture with respect to the previous cases. On the other hand, since the percentage are near 100% for all the models, it can be safely assumed that also $\mathcal{M}^B_{BJ_9}$ and $\mathcal{M}^B_{BJ_{10}}$ capture almost all the dynamics of the underlying system.

Passing on the Med_60 dataset, the fits are reported in (3.14). $\mathcal{M}^B_{BJ_9}$ and $\mathcal{M}^B_{BJ_{10}}$ are the ones with the highest Fit percentage and, as before, with also the same value:

$$\begin{aligned} \text{Fit}_{03}\left(\mathcal{M}^B_{ARX_{11}}\right) &= 99.865\% \quad \text{Fit}_{03}\left(\mathcal{M}^B_{ARMAX_5}\right) = 99.869\% \\ \text{Fit}_{03}\left(\mathcal{M}^B_{BJ_9}\right) &= 99.872\% \quad \text{Fit}_{03}\left(\mathcal{M}^B_{BJ_{10}}\right) = 99.872\%. \end{aligned} \tag{3.14}$$

Passing on the conclusion on the obtained results in this configuration, it can be safely said that this identification has optimal results over all. An explanation could be that, due to added weight on the ferrule, the system was exited sufficiently from the designed input and as a consequence the estimated model describes in a better way the real dynamics of the deviator. As it will be showed shortly, this will conclusion can be also applied to the speed loop estimate in configuration B.

Finally, for the choice of the optimal model the two candidate for the optimal model are $\mathcal{M}^B_{BJ_9}$ and $\mathcal{M}^B_{BJ_{10}}$. Since their results on all the validation tests were identical the only way to chose the optimal model is to chose the one with fewer number parameters.

With this in mind, the optimal model for the position loop estimate in configuration B is $\mathcal{M}^B_{BJ_9}$.

In Figure 3.8 it is reported a clearer image of the zeros and poles of $\mathcal{M}^B_{BJ_9}$. For a more detailed structure of $\mathcal{F}^B_{BJ_9}(z)$ it is recommended to consult the MATLAB file.

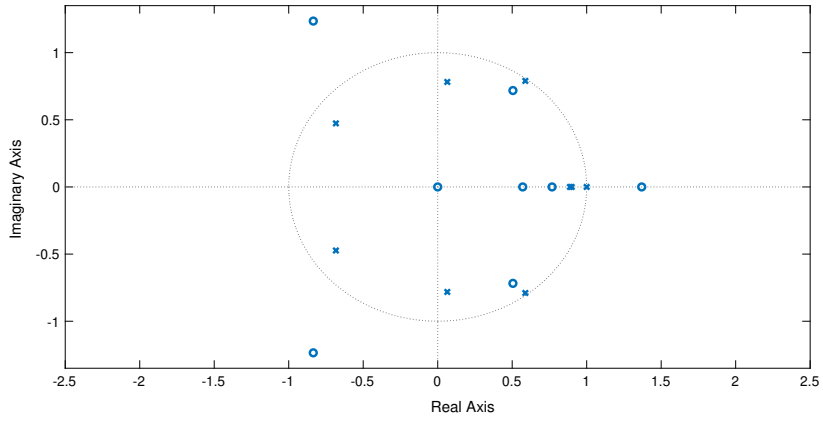

Figure 3.17: Zero-pole diagram of the chosen model $\mathcal{M}^B_{BJ_9}$ for the position loop identification in configuration B

3.5.2 Speed Loop

Finally, in this Section the validation results of speed loop model identification in the configuration B will be explained and analysed. Part of the dataset used for the identification is reported in Fig. 3.18. Here it is showed only the input $\tau_{ref}(t)$ used since the output $\omega_m(t)$ was already reported in Fig. 3.13(a) (red signal). As it was said before, here it is even more evident the difference between the two configuration of the deviator. Here it can be noted that the requested torque over the time is a lot higher with respect to the previous configuration. Again this is caused by the increased inertia that the motor must move in order to perform the movement.

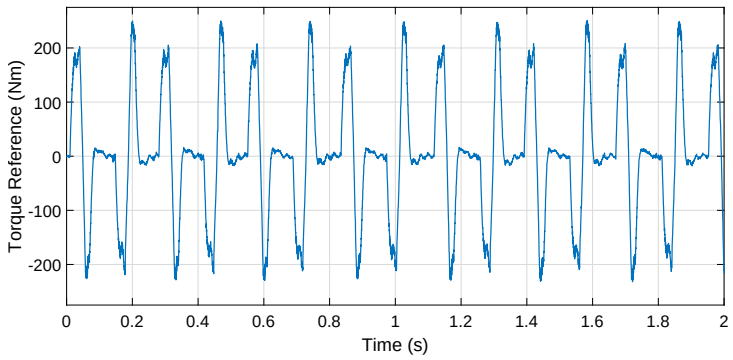

Figure 3.18: Segment of the reference signal $\tau_{ref}(t)$ with configuration B.

The last four models analysed are the following ones:

- $\mathcal{M}^{B_V}_{ARX_9}$: ARX model structure with number of parameters $n_A = n_B = 9$ and $n_k = 1$;
- $\mathcal{M}^{B_V}_{ARMAX_7}$: ARMAX model structure with number of parameters $n_A = n_B = n_C = 7$ and $n_k = 1$;
- $\mathcal{M}^{B_V}_{BJ_5}$: BJ model structure with number of parameters $n_B = n_C = n_D = n_F = 5$ and $n_k = 1$;
- $\mathcal{M}^{B_V}_{BJ_7}$: BJ model structure with number of parameters $n_B = n_C = n_D = n_F = 7$ and $n_k = 1$.

Figure 3.19 shows the zero pole diagram of the four models. The only notable thing to highlight is that model $\mathcal{M}^{B_V}_{ARMAX_7}$, showed in red in Fig. 3.19(a), has a close zero-pole quasi-cancellation near 1.

Starting now with the Complexity Terms test, in (3.15), the values of obtained for the four models are reported:

$$\begin{aligned} J_{AIC}\left(\mathcal{M}^{B_V}_{ARX_9}\right) &= 1.785 & J_{BIC}\left(\mathcal{M}^{B_V}_{ARX_9}\right) &= 1.389 \cdot 10^5 \\ J_{AIC}\left(\mathcal{M}^{B_V}_{ARMAX_7}\right) &= 1.736 & J_{BIC}\left(\mathcal{M}^{B_V}_{ARMAX_7}\right) &= 1.373 \cdot 10^5 \\ J_{AIC}\left(\mathcal{M}^{B_V}_{BJ_5}\right) &= 1.68 & J_{BIC}\left(\mathcal{M}^{B_V}_{BJ_5}\right) &= 1.356 \cdot 10^5 \\ J_{AIC}\left(\mathcal{M}^{B_V}_{BJ_7}\right) &= 1.694 & J_{BIC}\left(\mathcal{M}^{B_V}_{BJ_7}\right) &= 1.361 \cdot 10^5. \end{aligned} \tag{3.15}$$

As it was expected, the AIC and BIC values increased with respect to the position loop in configuration B but, like it was pointed out previously, those values are significantly lower than the ones obtained in the first speed loop identification. Passing on the analysis of the Complexity Terms results, the two BJ models have the best performances for both terms. As usual, this picture is confirmed by the Residual Analysis test (Fig. 3.20). It is clear that $\mathcal{M}^{B_V}_{ARX_9}$, as in the Complexity Terms test, is the model with the worst performances.

Passing on the Cross-Validation tests, it can be expected a higher percentage of all the Fit terms. Those analyses have a first confirm in (3.16) were the results obtained with the Med_60 dataset are reported. Notice that the values are similar to the position loop estimate in configuration B:

$$\begin{aligned} \text{Fit}_{Med}\left(\mathcal{M}^{B_V}_{ARX_9}\right) &= 99.418\% & \text{Fit}_{Med}\left(\mathcal{M}^{B_V}_{ARMAX_7}\right) &= 99.435\% \\ \text{Fit}_{Med}\left(\mathcal{M}^{B_V}_{BJ_5}\right) &= 99.441\% & \text{Fit}_{Med}\left(\mathcal{M}^{B_V}_{BJ_7}\right) &= 99.442\%. \end{aligned} \tag{3.16}$$

As it can be seen in (3.17), by changing dataset the performances remains pretty much good. It can be noted that, up until now, all the models that performed well in the previous validation tests have always one of the best performances of the Cross-Validation test:

$$\begin{aligned} \text{Fit}_{Trp}\left(\mathcal{M}^{B_V}_{ARX_9}\right) &= 99.355\% & \text{Fit}_{Trp}\left(\mathcal{M}^{B_V}_{ARMAX_7}\right) &= 99.376\% \\ \text{Fit}_{Trp}\left(\mathcal{M}^{B_V}_{BJ_5}\right) &= 99.370\% & \text{Fit}_{Trp}\left(\mathcal{M}^{B_V}_{BJ_7}\right) &= 99.373\%. \end{aligned} \tag{3.17}$$

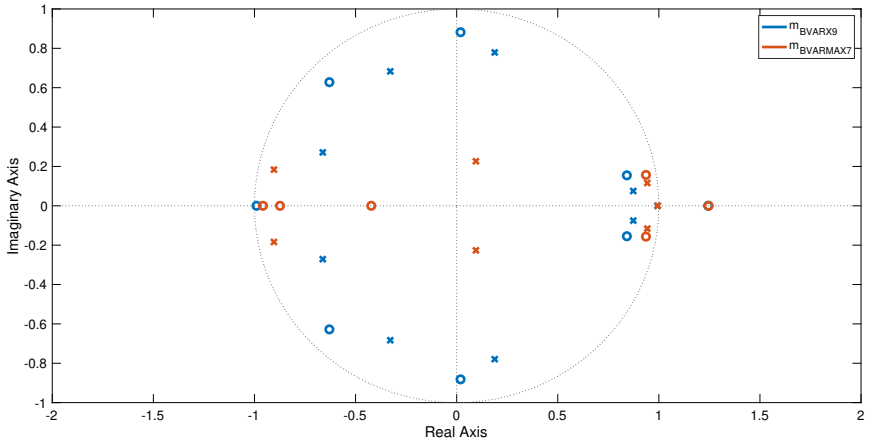

(a) Zero-pole diagram of models $\mathcal{M}^{B_V}_{ARX_9}$ (blue) and $\mathcal{M}^{B_V}_{ARMAX_7}$ (red)

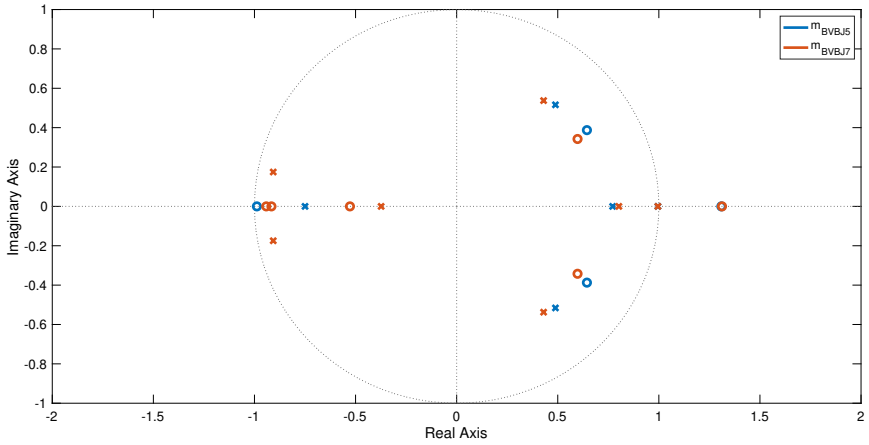

(b) Zero-pole diagram of models $\mathcal{M}^{B_V}_{BJ_5}$ (blue) and $\mathcal{M}^{B_V}_{BJ_7}$ (red)

Figure 3.19: Zero-pole diagram of the estimated speed loop models with configuration B: *in Fig. 3.19(a) models* $\mathcal{M}^{B_V}_{ARX_9}$ *in blue and* $\mathcal{M}^{B_V}_{ARMAX_6}$ *in red. In Fig 3.19(b) models* $\mathcal{M}^{B_V}_{BJ_5}$ *in blue and* $\mathcal{M}^{B_V}_{BJ_7}$ *in red.*

Finally, for the last dataset of the Cross-Validation test, the results are reported in (3.18). The conclusion that can be drawn from all the dataset remains the same as the one deduced with the previous validation tests. More specifically, $\mathcal{M}^{B_V}_{BJ_5}$ and $\mathcal{M}^{B_V}_{BJ_7}$ are the two models that have the highest Fit term in almost all the dataset:

$$\begin{aligned} \text{Fit}_{03}\left(\mathcal{M}^{B_V}_{ARX_9}\right) &= 99.353\% \quad \text{Fit}_{03}\left(\mathcal{M}^{B_V}_{ARMAX_7}\right) = 99.371\% \\ \text{Fit}_{03}\left(\mathcal{M}^{B_V}_{BJ_5}\right) &= 99.386\% \quad \text{Fit}_{03}\left(\mathcal{M}^{B_V}_{BJ_7}\right) = 99.381\%. \end{aligned} \tag{3.18}$$

From the analysis of the different validation tests it can be observed that, unlike the previous speed loop estimate, the estimation of the underlying system is more accurate. As it will be showed in Section 4.1, this is not so precise but it is enough for the task that will be done with it.

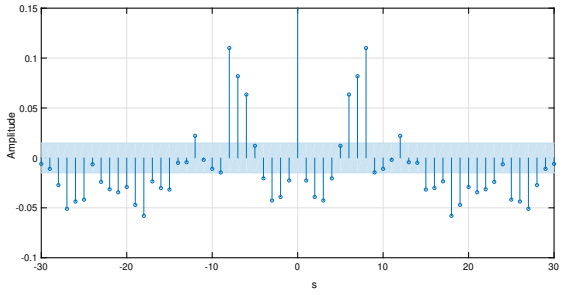

(a) Residual Analysis of $\mathcal{M}_{ARX_9}^{B_V}$

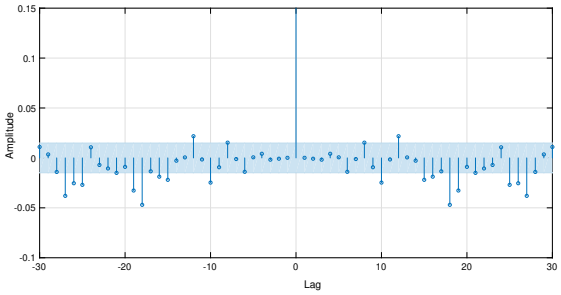

(b) Residual Analysis of $\mathcal{M}_{ARMAX_7}^{B_V}$

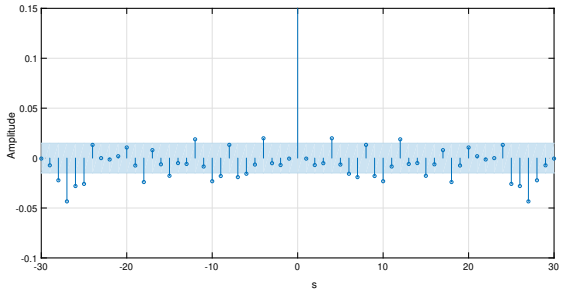

(c) Residual Analysis of $\mathcal{M}_{BJ_5}^{B_V}$

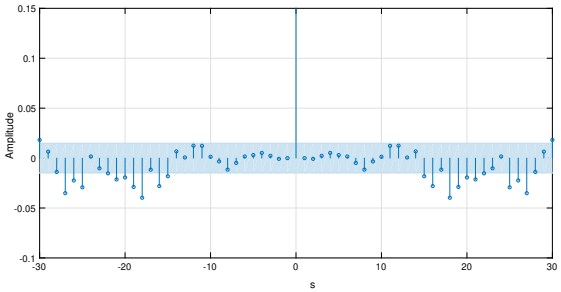

(d) Residual analysis of $\mathcal{M}_{BJ_7}^{B_V}$

Figure 3.20: Residual Analysis of the estimated models with configuration A: *the light blue area is the confidence region that* $r_{\varepsilon_{\hat{\theta}_{PEM}}}(s)$ *should not exceed. As it can be seen in Fig. 3.20(a) the estimated model* $\mathcal{M}_{ARX_9}^{B_V}$ *is the one with the poorest performances among all the four models.* $\mathcal{M}_{ARMAX_7}^{B_V}$, $\mathcal{M}_{BJ_5}^{B_V}$ *and* $\mathcal{M}_{BJ_7}^{B_V}$ *have almost the same performances.*

Finally, for the optimal model choice, $\mathcal{M}_{BJ_5}^{B_V}$ is selected as best model. This choice was made due to the high performances overall and, additionally, it has a fewer number of parameters than the other BJ model.

In Fig. 3.8 a clearer image of the zeros and poles of $\mathcal{M}_{BJ_5}^{B_V}$ is reported. For a more detailed structure of $\mathcal{F}_{BJ_5}^{B_V}(z)$ it is recommended to consult the MATLAB file.

3.6 System Identification Conclusions

In this final Section of this Chapter there will be a quick conclusion on the design of the performed experiment on the brushless eccentric deviator and on the utility of the different validation tests.

Starting with the input design it can be said that the input used to perform the identification of the position loop was correctly designed because the identification had good results in both configurations. Moreover, it is clear from the validation results that, for the configuration A, the input is not optimal. It is clear that in configuration A the deviator is not sufficiently excited to perform the identification. On the other hand, for the configuration B the results are adequate. A solution to the input problem in configuration A will be proposed in Chapter 5.

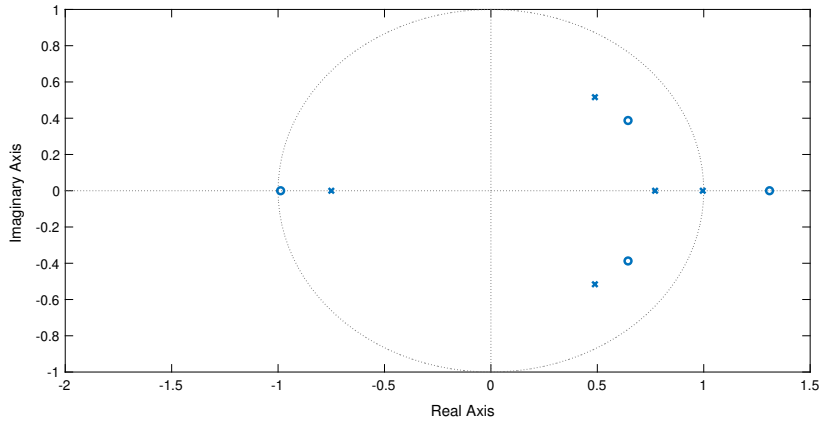

Figure 3.21: Zero-pole diagram of the chosen model $\mathcal{M}_{BJ_5}^{B_V}$ for the speed loop identification in configuration B

Passing on the validation test, regarding the Zero-Pole Cancellation method it can be said that it is a useful method when a there are a lot of models that need to be discarded. In fact, during the first validation procedure, there were a lot of models that had exact zero-pole cancellations that were immediately discarded from the pool of optimal model. Moreover, in some cases it was a good method to use at the final decision of the optimal model.

For the Residual Analysis test it can be affirmed that it was a good indicator of the goodness of the performances of the identified models but it was difficult to draw a conclusion on which model could be the optimal one. Furthermore, in the case of the speed loop identification in configuration A, the chosen optimal model was one with the worst residual plot.

On the other hand, the Complexity Terms even thought give in almost all the cases the same information of the Residual Analysis test, were a good way to obtain a good idea on which were the models that had the best performances and how good it was the estimate of the underlying system. Moreover, between the AIC and BIC terms there were not big differences and gave almost every time the same response. This validation method was always crucial for the optimal model choice.

Finally, the Cross-Validation test was, together with the Complexity Terms test, one of the key to determine the optimal model. Moreover, it was a good way to confirm if the identification procedure had a good or bad result overall. In Section 4.1 there will be a more challenging validation method and, as it will be showed, it confirms what deduced with the help of the Validation tests.

Chapter 4

Control Design for the Brushless Eccentric Deviator

4.1 A preliminary performances Comparison

In this Section there will be a comparison of the performances among the four identified models in the previous chapter. This analysis was performed to see if, these models can capture the dynamics of the system also in a simulated environment developed in MATLAB SIMULINK. Additionally, these results are going to be compared also with the one that can be obtained from the physical modellization.

This comparison was performed using a block diagram scheme similar to the one reported in Fig. 3.1 and the identical input and values of the controller that were used to generate the dataset with the underlying system. More specifically, these inputs were obtained in different conditions of the system but always with a significantly long delay between two different movements. Another important aspect about the MATLAB simulations is that all the tests were performed without the error of the estimated models or, in other words, with a model that had only the transfer function $\mathcal{F}(z)$ of the analysed optimal model.

The comparison was performed in the following conditions:

1. In normal condition (i.e. $C_\theta(z) = K_{P_\vartheta} = 450$) and with Regular input;
2. With a low value of $K_{P_\vartheta} = 150$ and with the Regular input;
3. With a high value of $K_{P_\vartheta} = 600$ and with the Regular input;
4. In normal condition and with the Run-Up input;
5. in normal condition with the Regular input and torque feed-forward action (only for the speed loops estimate).

Since some of the plot are similar to each other only a few of them will be reported in this thesis. However, all the plots can be consulted on the MATLAB file.

4.1.1 Configuration A

Position Loop: Starting with the position loop estimated model, in Fig. 4.1 two movements of the system performed with usual $K_{P_\vartheta} = 450$ and Regular input are reported. As it can be seen the response of the estimated model $\vartheta_{m,\mathcal{M}^A}(t)$ (in blue in the picture) is almost identical to the response of the real model $\vartheta_{m,R}(t)$ (in red).

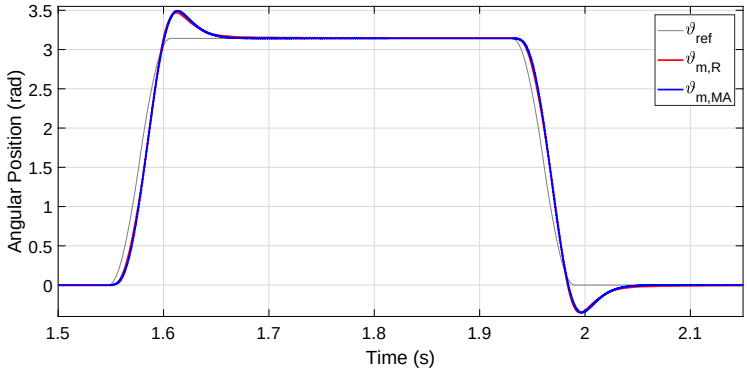

Figure 4.1: Comparison between the underlying system $\vartheta_{m,R}(t)$ (red signal) and the estimated position loop model response $\vartheta_{m,\mathcal{M}^A}(t)$ (blue signal).

A clearer view can be obtained by looking at the difference between the two signal (Figure 4.2). As it can be seen, for the same movements reported in Fig. 4.1 the error takes values that are lower than $\Delta\vartheta_{MAX,\mathcal{M}^A} < 0.08\,\text{rad}$, which can be considered a good result. Moreover, notice that in the most significant part for the control design task, the final part of the movement (i.e. $t > 1.6\,s$), the error is even lower.

It can be noted that the error of the two movements, the one from 0 to π and the reverse one from π to 0, are not perfectly symmetrical. This may seem a small difference given by the presence of some errors on the data but this is not the case. As matter of fact, recalling the shape of the eccentric shaft (Fig. 1.6) it can be noted that its profile is not regular and this implies small changes on the system dynamics. Furthermore, since the PEM estimate creates model that are linear and stable around zero, this non-regularity on the eccentric shaft cannot be captured or, more specifically, the PEM estimate tries to find a model that is a compromise between all the used data. This implies that all the identified models will have a dynamic that is a compromise between the movement from 0 to π and the reverse one from π to 0.

More importantly, in Fig. 4.2(b) it can be noted that the response of the model derived with the physical modellization have performances that are worse than the one with the identified model. This is due to the lack of information on the system, especially on the part of the frictions that affect the model and the presence of the ferrule.

Notice also that even in the physical modellization there is a difference between the movement from 0 to π and the one from π to 0. This is due to the fact that the modellization derived in Section 1 is regular and symmetric.

Similar considerations can be performed also for the Run-Up input test. More specifically, Figure 4.3 shows the error of the two proposed modellization. In the picture it can be easily seen that, with this input, $\mathcal{M}^A_{BJ_{10}}$ has discrete performances even if the

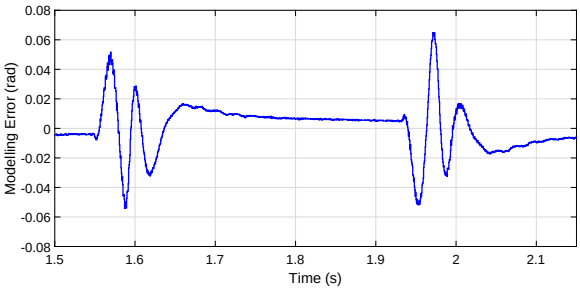

(a) Difference between the real model response $\vartheta_{m,R}(t)$ and the estimated model response $\vartheta_{m,\mathcal{M}^A}(t)$.

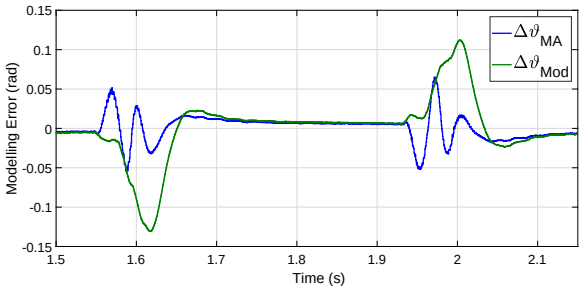

(b) Comparison between the error of the estimated model $\mathcal{M}^A_{BJ_{10}}$ (blue) and the simulation performed with physical model (green).

Figure 4.2: Difference between the underlying system response $\vartheta_{m,R}(t)$ and the estimated model response $\vartheta_{m,\mathcal{M}^A}(t)$ (left), and in comparison with the difference between the underlying system response $\vartheta_{m,R}(t)$ and the response of the model derived by the physical modellization $\vartheta_{m,Mod}(t)$ (right).

working condition is quite different with respect to the one that was identified with the PEM method. Moreover, like before, it is clear that the physical modellization response (in green in the picture) is good but is far from the performance of the identified model.

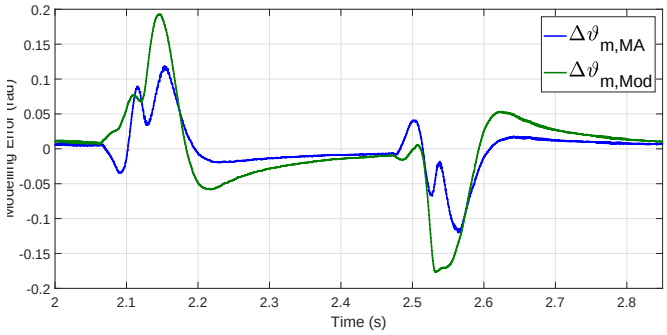

Figure 4.3: Comparison between the estimated position loop model error (blue signal) and the physical modellization error (green signal) when at the model is applied the Run-Up input.

Figure 4.4 shows the comparison between the underlying system (in red) and the estimated position loop model (in blue) when the plant is used with a different controller. More specifically, in Fig. 4.4(a) is reported the system response when both model are used with a proportional position gain equal to $K_{P_\vartheta} = 150$; similarly Figure 4.4(b) shows the case with a proportional position gain equal to $K_{P_\vartheta} = 600$. As it can be seen in both pictures the performances are identical to the normal case (with $K_{P_\vartheta} = 450$). These results confirms that the System Identification procedure provides a good model.

From this test it can be deduced that the optimal model $\mathcal{M}^A_{BJ_{10}}$ has optimal performances also in this test conditions. This confirms the decision that was made previously and confirms the analysis done with validation tests. Moreover, the good results obtained with different values of K_{P_ϑ} sets a good base for the design of the controller because it shows us that the estimated model captures the dynamics also when the model is used

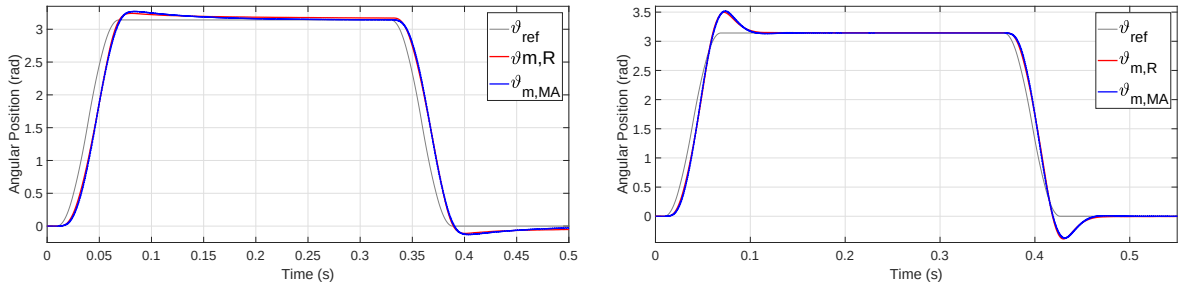

(a) Difference between the underlying system response $\vartheta_{m,R}(t)$ and the estimated model response $\vartheta_{m,\mathcal{M}^A}(t)$ with low K_{P_ϑ}.

(b) Difference between the underlying system response $\vartheta_{m,R}(t)$ and the estimated model response $\vartheta_{m,\mathcal{M}^A}(t)$ with high K_{P_ϑ}.

Figure 4.4: Difference between the real model response $\vartheta_{m,R}(t)$ and the estimated model response $\vartheta_{m,\mathcal{M}^A}(t)$ with various K_{P_ϑ}: *In Fig. 4.4(a) the comparison with a low value of K_{P_ϑ}, in Fig. 4.4(b) the comparison with a high value of K_{P_ϑ}.*

with different values on the position loop controller. This implies that a controller designed to obtain specific performances with the estimated model can be used with the real system and obtain similar performances. In Chapter 5 these results will be compared with a model obtained whith a PEM estimate performed with a more exciting input to see if this can further reduce the error between the identified and real system.

Speed Loop: Passing on the speed loop estimated model, Fig. 4.5, as it was expected from the validation tests analysis, there is a significant loss on the performances of the estimated model. This may seem a bad result but, as it will be showed shortly, these results will be a good starting point for the feed-forward input design and, more importantly, it is still a better description of the underlying system than the modelling used in Section 1 since the proposed physical modellization had a completely different dynamic when it was applied the torque feed-forward input. Here are not reported all the comparison that were performed in the previous analysis because the conclusions that can be made are similar to the one obtained with the regular conditions.

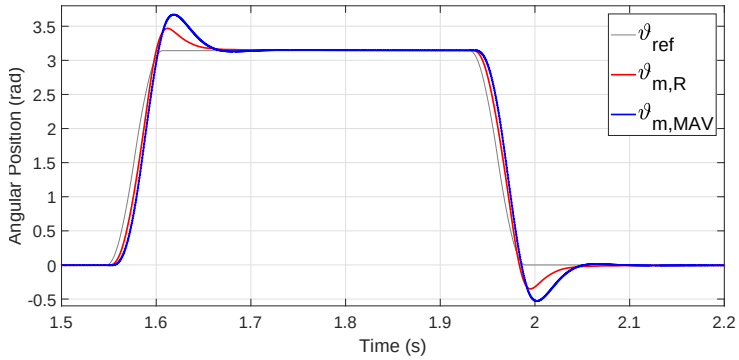

Figure 4.5: Comparison between the underlying system $\vartheta_{m,R}(t)$ (red signal) and the estimated speed loop model response $\vartheta_{m,\mathcal{M}^{A_V}}(t)$ (blue signal).

More in detail, if the feed-forward action is applied to the estimated model, the system response is like the one reported in Fig. 4.6 in blue. It can be clearly seen that there is

a resemblance between the underlying system and the estimated model angular response. Again the results are not optimal but this will be a excellent starting point for the design of a new input. Furthermore, it can be noted that, with this control law, the model response is affected by a lower overshoot but now it is present also a small undershoot; more details on the feed-forward input will be discussed in Section 4.3.

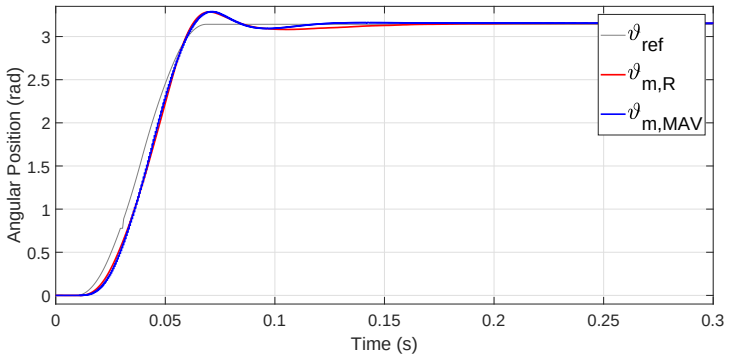

Figure 4.6: Comparison between the underlying system $\vartheta_{m,R}(t)$ (red signal) and the estimated speed loop model response $\vartheta_{m,\mathcal{M}^{A_V}}(t)$ (blue signal) with the action of the torque feed-forward action.

A clearer view on the estimated model and the underlying system resemblances when the feed-forward input is applied can be found in Fig. 4.7 where it is plotted the simulation error between $\mathcal{M}^{A_V}_{BJ_{11}}$ and the underlying system (in blue in the picture). It is clear from the plot that the identified system can be used to simulate the underlying system and, as it will be clarified in the following Sections, used to design a new input since $\mathcal{M}^{A_V}_{BJ_{11}}$ has a similar dynamic with respect to the underlying system during the parts of the movement that are interesting for the eccentric deviator specific application. Moreover, in the picture it is reported also the simulation error between the physical modellization and the real model. As it can be easily seen, the physical model response cannot be used as a simulation set-up to design a feed-forward torque input.

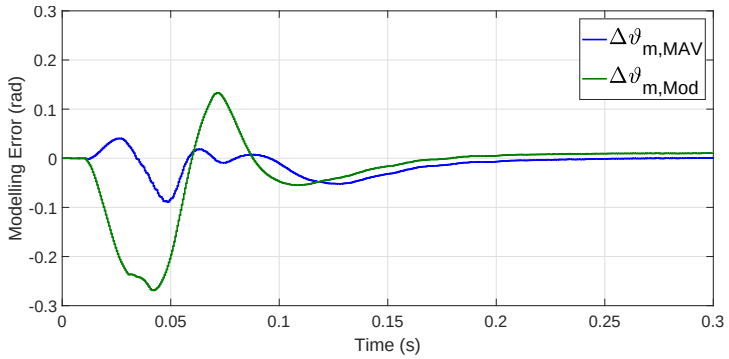

Figure 4.7: Comparison between speed loop estimated model and the modellization with the torque feed-forward input: *as it can be seen the modellization of the eccentric deviator (in green) has performances that are evidentially worse than the estimated speed loop model (in blue).*

As it will be explained in the next Sections, one of the key factor during the design

of the new controller is the shape of the brushless motor torque reference or, if possible, the generated torque of the motor. Obviously, since for the simulations performed with the estimated speed loop models it was not possible to acquire the generated torque, all the performed analysis are going to be carried out with the torque reference of the system. Furthermore, to confirm that $\mathcal{M}^{A_V}_{BJ_{11}}$ in Figure 4.8 it is showed the torque reference generated by the estimated model (in blue) and the underlying system (in red). As it can be seen, especially during the start of the movement, the signals are similar and this will be very useful later on. The disturbance in the estimated reference (in the blue signal between 0.02 and 0.04) is probably due to a the presence of a numerical derivatives.

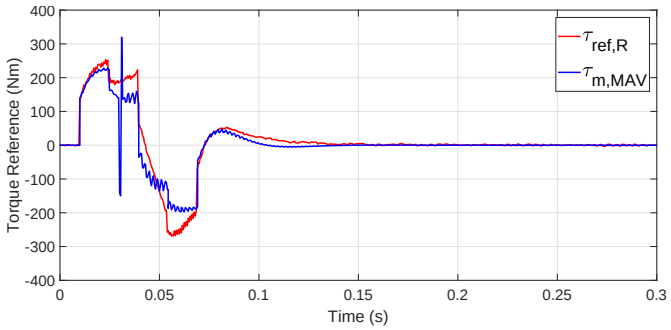

Figure 4.8: Comparison between the torque reference of the underlying system $\tau_{ref,R}(t)$ (red signal) and the torque reference of the estimated speed loop model $\tau_{ref,\mathcal{M}^{A_V}}(t)$ (blue signal) with the action of the torque feed-forward action for a movement from 0 to π.

Notice that, as showed in Fig. 4.6, the requested torque takes values outside the interval $\pm 200\,Nm$ which is almost the 300% of the nominal torque. As it will be explained later, even if the deviator's motor can sustain high quantities of requested (and consequently generated) torque for short a period this situation should be, if possible, avoided.

In the case of the feed-forward design, the part of the model response that is of interest for the thesis is the first and central part of the movement. Again, all the detail on how the new control law should be designed will be explained in Section 4.2.

4.1.2 Configuration B

Position Loop: Passing on the configuration B, for the position loop the results are similar to the previous position loop estimate. As a matter of fact, Figure 4.9 shows that the underlying system and $\mathcal{M}^{B}_{BJ_{10}}$ have an almost identical response.

Like in the previous position loop estimate, by looking at the difference between the underlying system response $\vartheta_{m,R}(t)$ and the estimated model response $\vartheta_{m,\mathcal{M}^B}(t)$ (Fig. 4.10(a)) it can be noted that the performances are again good. Moreover, in Fig. 4.10(b) it can be noticed that the estimated model can capture the dynamic of the underlying system in a more efficient way than the physical modellization as it was already clear from the previous comparison.

It is worth noting that, the simulation with the physical modellization was done with the same model used for the analysis of configuration A. This was the only feasible solution

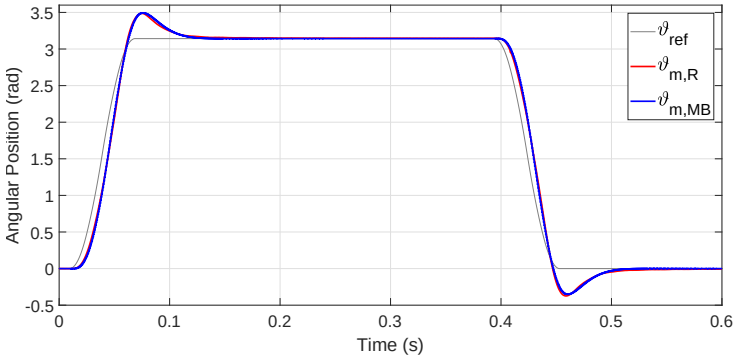

Figure 4.9: Comparison between the underlying system $\vartheta_{m,R}(t)$ (red signal) and the estimated position loop model response $\vartheta_{m,\mathcal{M}^B}(t)$ (blue signal).

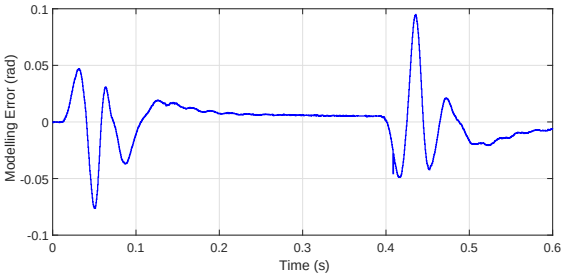

(a) Difference between the underlying system response $\vartheta_{m,R}(t)$ and the estimated model response $\vartheta_{m,\mathcal{M}^B}(t)$.

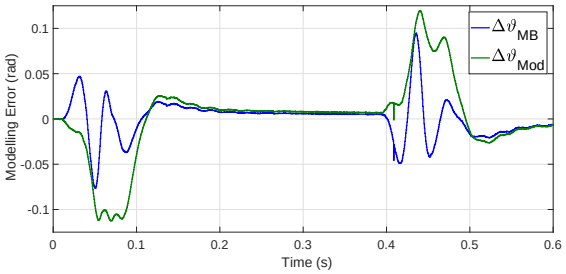

(b) Comparison between the error of the $\mathcal{M}^B$ (blue) and the simulation performed with physical model (green).

Figure 4.10: In Fig. 4.10(a) it is reported the difference between the underlying system response $\vartheta_{m,R}(t)$ and the estimated model response $\vartheta_{m,\mathcal{M}^B}(t)$ and, in Fig. 4.10(b) it is reported in blue in comparison with the difference between the underlying system response $\vartheta_{m,R}(t)$ and the response of the model derived by the physical modellization $\vartheta_{m,Mod}(t)$.

because there was no way to easily add the weight attached to the ferrule in configuration B on the modellization. With the analysis of the performances of both configuration it can be preliminary said that performing System Identification was a good way to obtain a information about the underlying system.

Furthermore, even in this configuration there is a difference in the response of the underlying system during the first movement, from 0 to π, and the second one, from π to 0. Consequentially also in this case the PEM method tries to obtain a compromise between the two different movements.

Since the results are similar to the previous position loop analysis, the comparison plot of the different work conditions are not reported. If needed, all the graph can be consulted on the MATLAB file which is available up on request.

Speed Loop: Finally, here are reported the performances of the speed loop estimate with configuration B. As it will be showed, even if the validation results were better than the previous speed loop identification, the estimated model had simulated performances similar to the ones obtained previously. In fact, as it can be seen in Fig. 4.11, as for

$\mathcal{M}_{BJ_{11}}^{A_V}$, the estimated model has a response that resembles the underlying system.

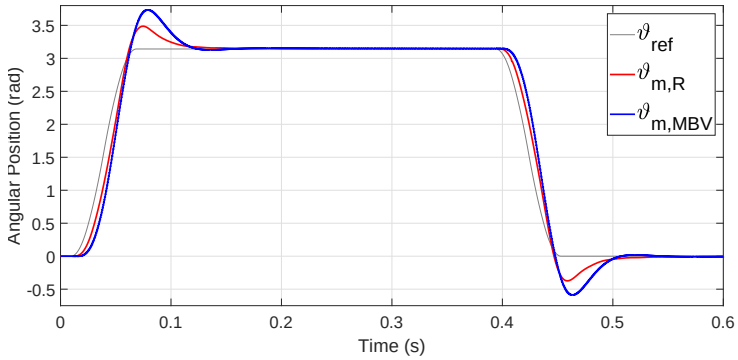

Figure 4.11: Comparison between the underlying system $\vartheta_{m,R}(t)$ (red signal) and the estimated speed loop model response $\vartheta_{m,\mathcal{M}^{B_V}}(t)$ (blue signal).

As in the previous speed loop case, if the torque feed-forward action is applied to the system the estimated model can give good hints for the design of a new feed-forward action. In Fig. 4.12 it is showed the comparison between the estimated and the real model when is applied also the torque feed-forward. As it can be noted the response is similar and this is an optimal result to perform a preliminary analysis on the feed-forward input design.

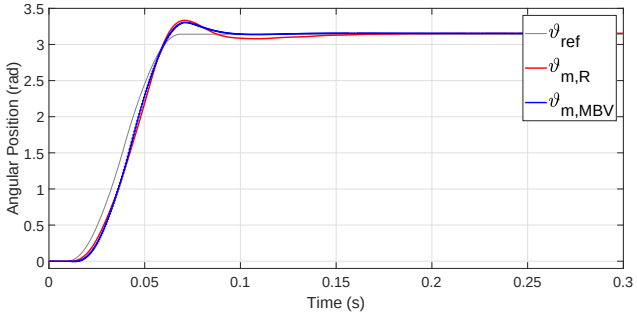

Figure 4.12: Comparison between the underlying system $\vartheta_{m,R}(t)$ (red signal) and the estimated speed loop model response $\vartheta_{m,\mathcal{M}^{B_V}}(t)$ (blue signal) with the action of the torque feed-forward action.

As in the previous speed loop identification, similar considerations can be performed also on the requested torque and the comparison with the physical modellization of the eccentric deviator. The only thing that it is worth noting is that, as it was observed in Section 3.5.2, the requested torque has higher values than the tests with the configuration A.

4.2 PID Design for the Position Loop

In this Section there will be the design of the new PID controller for both configuration but, before doing so it will be given a quick overview on the objective that the new

controller should satisfy. The following considerations will be also applied for the design of the new torque feed-forward input.

Starting with the more obvious part, one of the main objective is to reduce the system over-shoot. The main advantage that comes from this reduction is that this there is a significant decrease of the eccentric deviator mechanical wear. Moreover, a significant reduction of the over-soot can improve the durability of the mechanical parts of the deviator since those parts are the one that have the more significant impact on the machine life.

Another important objective is to have a system that respond quickly and, in the case of the deviator, a system that has a response that is repetitive. In other words, the new controller should provide a response of the system that is as quick as possible and, more importantly, have a response as similar as possible to the reference signal. This is crucial because the task that the deviator perform highly relies on the synchronization with the shear and, knowing where the ferrule might be at a specific time is a decisive information. Specifically, the cut of the iron rod is performed when the deviator is approximately in a window centred in the middle point of the movement (i.e. at $t_c = 0.03\,s$ for a Regular input that starts at $t_0 = 0\,s$) and consequentially it is desired that in a neighbourhood of the cutting window the response should be as close and similar to the reference as possible. This is the reason why the focus should be put onto the first and central part of the movement during the controller design.

Finally, one of the most important objective of the new controller is that it should reduce as much as possible the requested and generated torque of the motor. As it was showed in the previous Sections, the motor installed on the eccentric deviator can easily handle torque with this high values for small periods of time like in this case but this comes at a cost. In fact, this condition of work stresses the motor and leads to a shortening of its total life on the plant or, in other words, it will be substituted in a shorter time compared to a use of the motor in normal conditions. These are the main problems that impact on the eccentric deviator life and performances.

Due to the lack of time, to design the PID controller it was used the function *pidTuner* of the MATLAB environment. Moreover, since the old PID controller used only the proportional action, the search of the new PID controller was performed on controllers with also an integral part. As it will be reported, sometimes the performances of the new PID will not be so optimal but the results can still be used because, as it was shown in the previous section, position loop identified models can capture the underlying system dynamics and can be used to simulate the eccentric deviator performances. Moreover, these simulations are a good way to obtain a rough idea of the response of the real system with a different control law.

As it will be showed later, it is difficult to satisfy all the request, especially with only the change of the PID controller. Luckily, as it will be reported at the end of this chapter, the obtained results with the new PID controller and the new feed-forward input are a huge improvement for the control of the eccentric deviator.

4.2.1 Configuration A

Starting with the PID tuning of the position loop with the deviator in configuration A, by running the *pidTuner* function and searching for a PI controller, after a small tuning the PID had the following structure:

$$C_{\vartheta}^{N_A}(z) = K_{P_\vartheta} + \frac{K_{I_\vartheta}}{z-1} = 406 + \frac{3680}{z-1}. \tag{4.1}$$

As in the previous case, the response of $\mathcal{M}_{BJ_{10}}^{A}$ with the new controller $C_{\vartheta}^{N_A}(z)$ is close to the one of the underlying system. The comparison can be found in the MATLAB file which can be consulted up on request.

As it is showed in Fig. 4.13, the old controller $C_{\vartheta}^{O}(z) = 450$ performances are still better than the one with new controller where it was added also the integral part. More in detail, it can be easily noted that the deviator response with the old values of the PID controller (blue signal) is slightly better since it is affected by a lower overshoot. In Fig. 4.13 it is reported only the 0 to π movement but the same observation can be done also for the inverse movement.

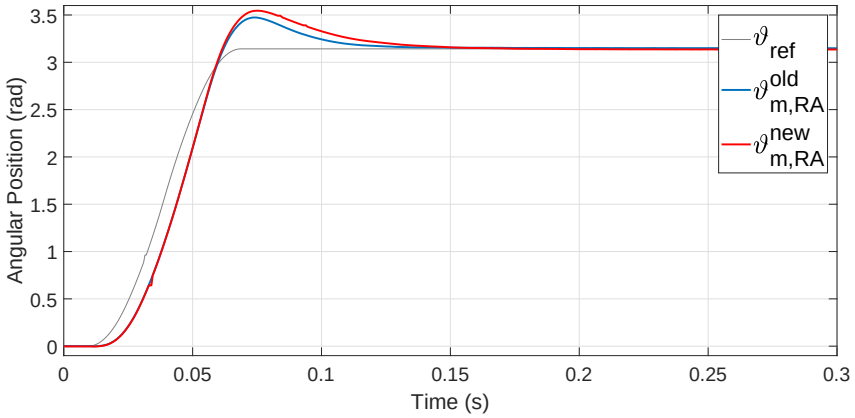

Figure 4.13: Comparison between the response of the deviator in configuration A with the new and the old controller: *Response of the deviator with the old controller* $C_{\vartheta}^{O}(z)$ *(red signal) and the new controller* $C_{\vartheta}^{N_A}(z)$ *(in red). As it can be seen the old controller has a slightly better performances than the new one.*

On the other hand, $C_{\vartheta}^{N_A}(z)$ may be a better solution when the deviator operates under production conditions because, thanks to the presence of the integral part, the system is more robust to the presence of disturbances or errors on the modellization. Unfortunately, the production conditions could not be tested for obvious reason. Moreover, this is a condition that changes again the dynamics of the system and more importantly it comes with a lot of additional disturbances and error. Those changes are a consequence of the iron rod that flows trough the tube during the usual usage of the eccentric deviator. More specifically, the iron rod presence does not only change the inertia of the tube but, since it moves trough the tube it also produces vibrations that can be considered as error that are added to the system.

For the rise up time it can be seen that the old and new controller have almost no differences. Moreover, the same reasoning can be applied to the torque, reference or generated, where both PID have a response which is almost identical.

4.2.2 Configuration B

For the configuration B the results are more performing. This is probably explained by the fact that the controller is usually tuned and optimized for the small ferrule and consequentially it cannot take in consideration also the other working conditions. As before, by using the *pidTuner* function in MATLAB with the selected optimal model $\mathcal{M}^B_{BJ_9}$, after some minor tuning, the new PID controller was selected and the controller was designed with only integral and proportional gains. Its values are the following ones:

$$C_\vartheta^{N_B}(z) = K_{P_\vartheta} + \frac{K_{I_\vartheta}}{z-1} = 395 + \frac{3435}{z-1}. \tag{4.2}$$

Figure 4.14 reports the system response with the old values of the PID ($C_\vartheta^O(z) = 450$) and the one with $C_\vartheta^{N_B}(z)$. As it can be seen there is a small improvement on the over-shoot values but it is difficult to evaluate it.

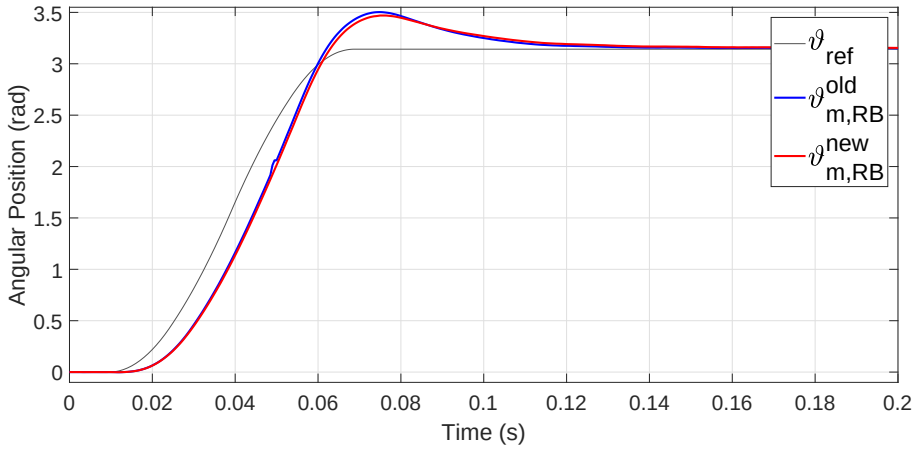

Figure 4.14: Comparison between the response of the deviator in configuration B with the new and the old controller: .

To have a better idea in Fig. 4.15 it is reported the tracking error ($\Delta\vartheta(t) = \vartheta_{ref}(t) - \vartheta_m(t)$). As it can be seen, the system with the new controller is just a bit slower than the system with the previous control law (from $t_0 = 0$ to $t_1 = 0.06$) but it can count on a lower overshoot value. More importantly, like in the previous case, the presence of the integral part may become useful when the system operates under working conditions.

Like in the previous case, for the reference and generated torque both controller perform equally and there are no significant differences between the two controllers.

With this result it can be seen that the by adjustment of the controller for each configuration may help obtain a system that adapts and gives always the best response. Unfortunately this is still difficult to implement on the system. In Chapter 6 will be explained why and what should be the steps that need to be performed to achieve this goal.

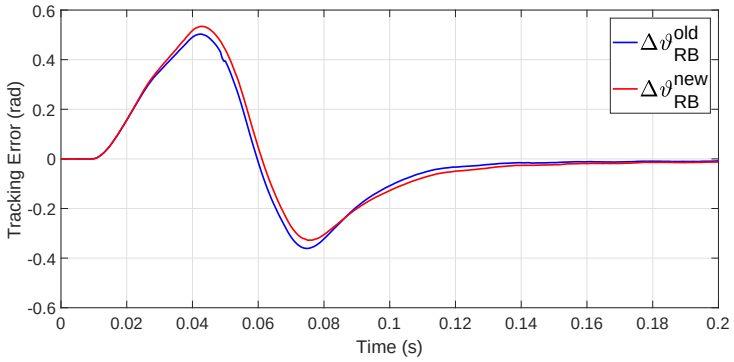

Figure 4.15: Comparison of the tracking error between the old PID (blue) and the new one (in red): *as it can be seen the system with the new controller respond slightly slower in the first part of the movement but has a lower overshoot.*

4.3 Torque Feed-Forward Design

Before going on with the feed-forward design a quick explanation on why it was and how it was designed is needed. The feed-forward input was firstly added to help the motor start the movement and, more importantly, make the system response quicker and repetitive especially in the central part of the movement. The input that was designed by the SMS Group, reported in Fig. 4.16, was a step signal composed by four different steps with amplitude proportional to the angular acceleration of the relative angular velocity segment. It is clarified to the reader that the designed input was different for each speed profile but here it will be reported only the analysis with the Regular profile. Moreover, the feed-forward design will be performed only for the configuration A since the difference between the two cases were only just a higher values of the generated and reference torque of the motor and a position response that was just a bit slower in the second configuration. A final note on the design is that the analysis will be performed using only the old PID controller $C^{O}_{\vartheta}(z) = 450$. This is a consequence of the fact that the implementation of an adaptive controller is still difficult to implement on the system. More detail on the difficulties of the adaptive controller will be explained in Chapter 6.

Additionally, one of the most important reason that forced the introduction of a torque feed-forward input was to help the system, to stop the movement and reduce drastically the over-shoot. More specifically, with an input like the one that was previously described, the over-shoot reduction was significant but it added also an unwanted under-shoot. This can be easily noted in Fig. 4.17 and was probably caused by the last step of the feed-forward input. More in detail, the last step of the input was responsible of a high values of the reference torque and, consequentially, the motor input forced the system to move in the opposite direction of the performed movement. In other words, when the system is starting to stop and both the speed and position controller would set a low value of torque the feed-forward input sets a high and unnecessary value of requested torque that induces an opposite action.

A clear view of the advantages that comes form the feed-forward addition can be found in Fig. 4.18(a) where is reported the comparison between the tracking error before (in blue) and after (in red) the addition of the torque input during one movement. As it

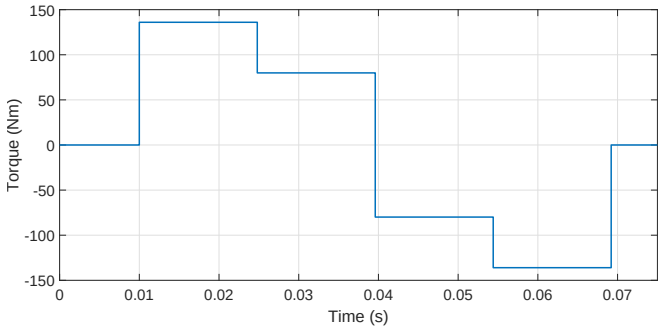

Figure 4.16: Old feed-forward torque input of the Regular profile during the 0 to π movement: *the for step derived by the segment of the speed profile can be easily spotted. The first two steps ($t < 0.04\,s$) are the ones that help the system start the movement, the last two the ones that helps the system stop. The torque value of the two higher steps is equal to $136\,Nm$ (approximately the 200%); the two central steps have a instead a value equal to $79.9\,Nm$ (approximately the 115%). Moreover, this input refers as a movement that starts at $t_0 = 0.01\,s$.*

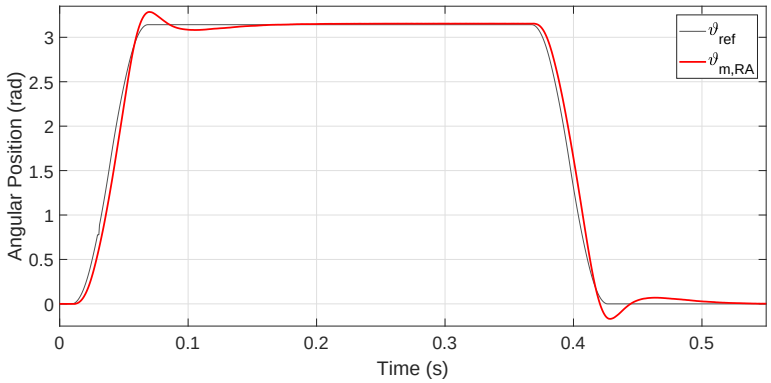

Figure 4.17: Response of the system with the old feed-forward torque input: *as it can be seen the response of the system is quicker than the situation without the feed-forward input and is affected by a lower overshoot. Unfortunately this comes with an unwanted undershoot of the eccentric deviator response.*

can be seen, the advantages are evident and can be considered good even with the small undershoot that is present. Unfortunately, this better performances come with a high value of generated (and also reference) motor torque (Fig. 4.18(b)). More specifically, as it can be noted in the picture, the motor generated torque with the feed-forward input (in red) have a higher negative peak and, by computing the mean of the signal during one movement, it can be seen that when the feed-forward input is not applied its mean is equal to $\bar{\tau}_m = 7.7255$ which is a lower value with respect to $\bar{\tau}_m^{FF} = 8.3699$, which is the one obtained when the input is applied.

Another thing that is worth to point out is that, with the old input, the motor generated torque had some discontinuities. This can be noted in the red signal during the positive peak reported in Fig. 4.18(b) and is another thing that impacts on the durability of the brushless motor.

Passing now on the design of the new input, the goals that were setted during the

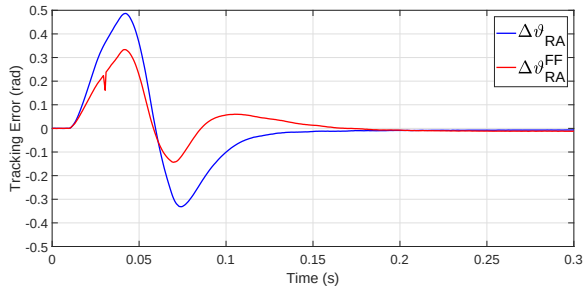

(a) Comparison between the tracking error of the system with (in red) or without (in blue) the old feed-forward input

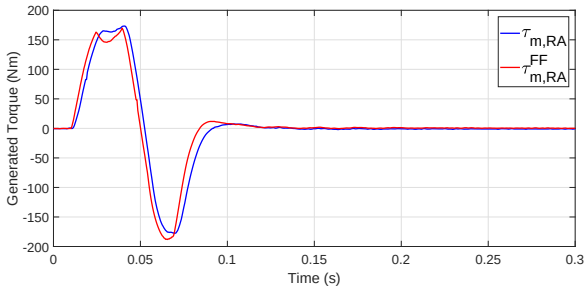

(b) Comparison between the generated torque of the motor (in red) or without (in blue) the old feed-forward input

Figure 4.18: Comparison of the performances of the system with or without the old feed-forward input: *in Fig. 4.18(a) it is reported the tracking error of the model and it can be seen that adding the feed-forward input gives great advantages. In Fig. 4.18(b) it is reported the comparison between generated torques and it can be noted that this advantages comes with a higher overall generated torque.*

tuning are the following ones:

- Obtain a similar response as the one with the old feed-forward input, especially in the first and central part of the movement;
- Reduce, if possible, the over-shoot and get rid of the under-shoot;
- Reduce the generated (and reference) torque of the system.

Moreover, this tuning was performed by looking at the position response of the estimated model and, more importantly, its torque reference. In principle, one would be intrested in the torque applied from the motor rather than the torque reference. On the other hand, this choice was forced by the fact that in the identified model was not possible measure of the applied motor torque. Notice that, from Section 4.1.1, is known that the underlying system and the estimated model have similar performances for both the angular position and the torque reference. These resemblances were used to obtain a rough idea on how the system could have responded to a different input.

The first idea for the new input was to use a signal like the one reported in Fig. 4.19. This shape was designed to keep the first part of the signal and obtain the same quick response as the one with the old feed-forward. For the central part and the final part of the movement it was developed this profile with two linear functions that were added to reduce as much as possible the jumps from different values of torque and to leave the controllers determin the right torque input that the system needed at the moment. Moreover, the linear increase that can be noted after $t_3 \approx 0.04\,s$ was added to help the controllers start stopping the deviator movement. Ideally, this input was designed to help the deviator only in the first part of the movement but leave the controllers decide in an almost independent way the torque reference that has to be applied to the system. Furthermore, the step amplitude and value at which the linear increase starts are equal to the amplitude of the maximum and minimum step of the old fed-forward input ($\pm 136\,Nm$).

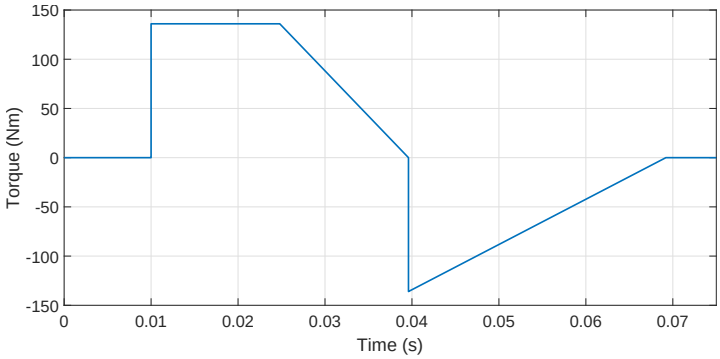

Figure 4.19: Proposed torque feed-forward input: *the input was designed to keep the same performances in the first part of the movement and the let the controllers decide almost in an independent way the torque reference that has to be applied to the system.*

By performing the simulation with this preliminary input on $\mathcal{M}_{BJ_{11}}^{A_V}$, the system response was like the one reported in Fig. 4.20(a) (the obtained signals are compared with the underlying system response with the old feed-forward input applied). The first notable thing is that, as it is showed in Fig. 4.20(a), the system is again affected by an over-shoot. This can be the consequence of a too low value of torque reference in the final part of the movement; this is also confirmed in Fig. 4.20(b) where it can be clearly seen that the reference torque of $\mathcal{M}_{BJ_{11}}^{A_V}$ in the second part of the signal is significantly lower than the previous one. Moreover, the first part of the movement is optimal for both the torque and the position response. These consideration sets the first guidelines for the new feed-forward input which should similar to the one reported previously in the first part of the signal and have a shape that forces a higher negative value on the torque during the final part of the movement. This design guidelines are justified by two facts: the higher over-shoot that affects the system and the low values on the torque reference in the final part of the movement.

With the considerations of the previous paragraph it was designed the input reported in red Fig. 4.21. As it can be seen the first step duration was reduced and the linear decrease was stretched as a consequence. For the second half of the movement it was used a similar structure as the first half of the input in fact. As it is showed in the picture, there is a negative step followed by a linear increase. The values of the steps are like before. Notice that this input does not end at the same time of the desired speed profile. The reason for this is that, since this last input was adjusted a bit with some test on the underlying model, it was noted that helping the controllers even after the end of the input improved the performances of the system. Furthermore, the tuning performed on the deviator were only small adjustment of the duration of the different part of the signal that are not going to be covered in this thesis.

By performing again a simulation with the $\mathcal{M}_{BJ_{11}}^{A_V}$ and applying the new feed-forward input the results are the one showed in Fig. 4.22 (the obtained signals are compared with the underlying system response with the old feed-forward input applied). The first notable thing is that the position response, reported in Fig. 4.22(a), is almost good. More in the detail, the identified model keeps the quick starting response and it has a smooth convergence to the final reference as it was requested. A practical note: since the shear

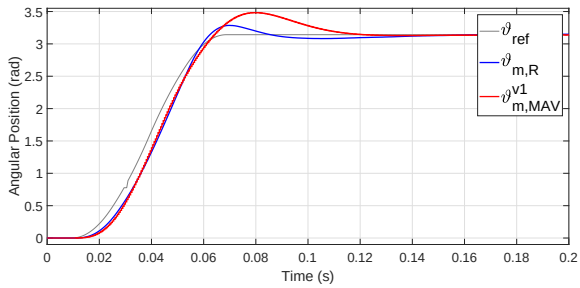

(a) Response of the estimated system with the with the proposed feed-forward input (in red).

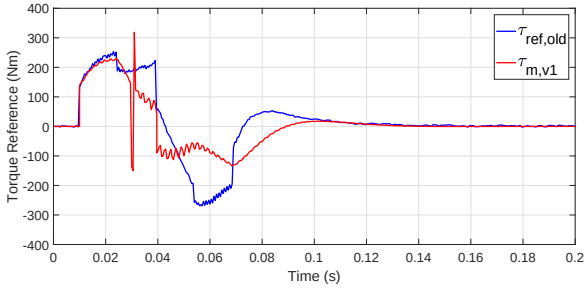

(b) Torque reference of the estimated model with the with the proposed feed-forward (in red).

Figure 4.20: Estimated system simulations with the proposed feed-forward input: *in Fig. 4.20(a) it is reported the response of the system in red compared with the response of the real model with the old input; as it can be seen the response is good for the first half of the movement but it suffers of a high unwanted overshoot. In Fig. 4.20(b) it is reported the requested torque by the estimated system in red and the previous requested torque of the real system; notice that here the torque reference is still too high for the first part of the movement.*

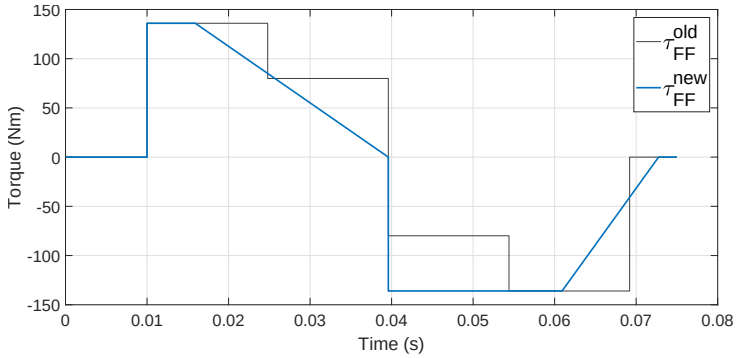

Figure 4.21: New feed-forward torque input: *in the picture it is showed also the old input to compare the two. As it can be seen both the start and the stop of the movement have a similar design.*

knives cuts the material in a position that is around the middle point of the movement (in this case around $0.04\,s$ since it starts at $t_0 = 0.01\,s$), the response obtained with the new input can be considered good. Moreover, the slow convergence to the final value of the input can be considered a good feature because, if maintained also in the underlying system, it can bring a sensitive reduction of the mechanical stress on the deviator and also because it is not crucial for the deviator application to quickly reach the final value. Passing on the torque, as it is showed in Fig. 4.22(b), the over all performances are acceptable because it can be hypothesized that even the underlying system reference will not exceed too much the 300% of the nominal torque.

Finally, in Fig. 4.23 it is reported the eccentric deviator response with the new feed-forward input applied. It can be clearly seen that the system has a response with even better performances than the ones obtained with the identified model. More specifically, the model has almost no overshoot like it was hypnotized previously.

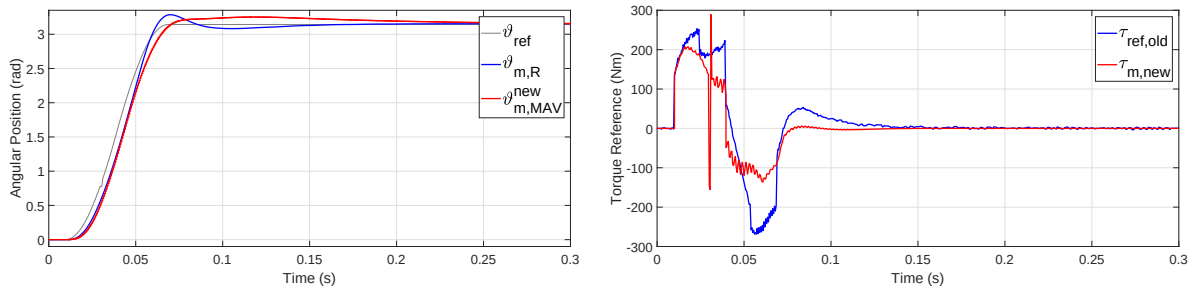

(a) Response of the estimated system with the with the new feed-forward input (in red).

(b) Torque reference of the estimated model with the new feed-forward (in red).

Figure 4.22: Estimated system simulations with the new feed-forward input: *in Fig. 4.22(a) it is reported the response of the system in red compared with the response of the real model with the old input; as it can be seen with the new input there is an acceptable response of the estimated model. In Fig. 4.22(b) it is reported the requested torque by the estimated system in red and the previous requested torque of the real system; notice that the torque reference is almost always under the* 300% *of the nominal torque.*

To have a clearer view, Fig. 4.24(b) shows the comparison between the tracking error with the new feed-forward input, in red, with the previous one, in blue. It can be seen that the two tracking errors are similar especially during the first half of the movement. Moreover, with the new input there is a smoother convergence to zero of the error. As it was already said, this smooth response is optimal because it reduces drastically the stress on the mechanical parts of the deviator.

Passing on the analysis of the torque and, in this case, by putting the focus on the generated torque showed Fig. 4.24(b), it can be seen there is a small improvement during the acceleration that comes also with the disappearance of the discontinuities that affected the system when the torque was at its peak. Moreover, there is a significant improvement on the deceleration which is kept always under the 250% of the nominal torque. A similar analysis can be performed also for the reference signal or the inverse movement. All the plots can be found in the MATLAB file.

As it was explained, with this new input, the eccentric deviator has improved a lot the performances with respect to the previous input or the system without feed-forward action. The deviator response keeps the quick reaction at the beginning of the movement, which is useful for the application, and low values of reference or generated torque, which is good for the durability of the brushless motor.

This new control law has already been implemented on the system since it was easy to customize for the different inputs that the SMS Group uses on the eccentric deviator.

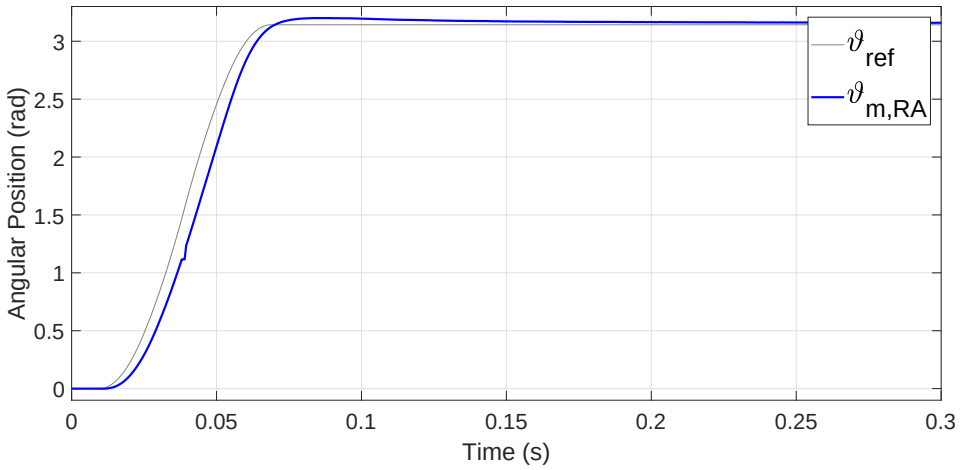

Figure 4.23: Response of the eccentric deviator with the new feed-forward input: *as it can be seen the performances are optimal and there is almost no overshoot.*

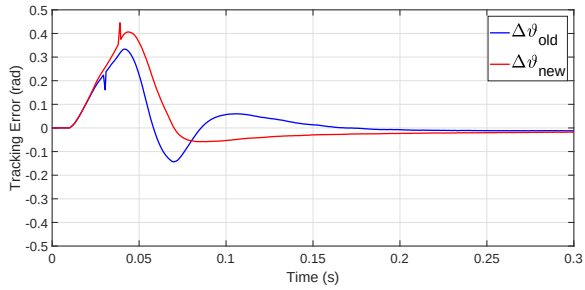

(a) Comparison of the tracking error of the system with the old feed-forward input (in blue) and with the new one (in red).

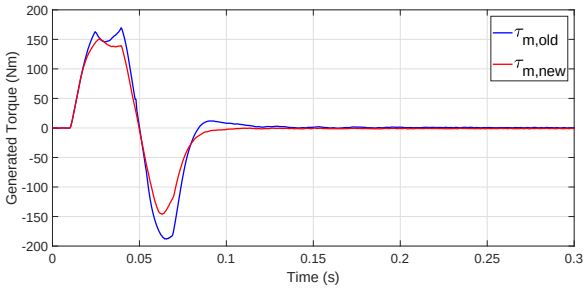

(b) Comparison of the generated torque of the system with the old feed-forward input (in blue) and with the new one (in red).

Figure 4.24: Eccentric deviator tracking error and generated torque with the new torque input: *in red the signals measured on the system with the new input, in blue the ones measured with the old input. In Fig. 4.24(a) it can be seen that the deviator with the new input has a better response than the old one. In Fig. 4.24(b) it can be seen that with the new input the generated torque is lower.*

Chapter 5

More Exciting Input for the Brushless Eccentric Deviator

In the previous Chapter it was clear that the input used for the identification procedure was one of the key element to obtain a performing estimate of the brushless eccentric deviator. More in detail, it was clear that both PEM estimate performed on the configuration B was conducted with an input that was designed accordingly to the identification constrains. On the other hand, the PEM estimate of the configuration A models was good for their results but it was clear from the validation tests that the input was not sufficiently exciting to perform the identification especially for the speed loop. To solve this, during the tests on the deviator, it was acquired an additional dataset that was similar to the one used in the previous cases to perform the PEM estimate but with a delay time from two different movements equal to $T'_{delay} = 0\,s$, instead of $T_{delay} = 2\,ms$[1].

In this Chapter there will be a quick analysis on the results obtained with this new dataset. To ease the analysis the model structures that were analysed are the Box Jenkins and the ARMAX model structures. Moreover, here it is reported only a quick analysis so the most of the plots will be omitted but, as usual, the plots can be found on the MATLAB file.

5.1 Position Loop

As it was said before, the model structures analysed were only the BJ and the ARMAX and, for the position loop model, the four model selected were:

- $\mathcal{M}^{A_{ND}}_{ARMAX_8}$: ARMAX model structure with number of parameters $n_B = n_C = n_D = n_F = 11$ and $n_k = 1$;
- $\mathcal{M}^{A_{ND}}_{BJ_5}$: BJ model structure with number of parameters $n_B = n_C = n_D = n_F = 5$ and $n_k = 1$;

[1]It is reminded to the reader that the delay period is the time that passes from the acknowledgement of reached position and the start of the next movement.

- $\mathcal{M}_{BJ_8}^{A_{ND}}$: BJ model structure with number of parameters $n_B = n_C = n_D = n_F = 8$ and $n_k = 1$;
- $\mathcal{M}_{BJ_{13}}^{A_{ND}}$: BJ model structure with number of parameters $n_B = n_C = n_D = n_F = 13$ and $n_k = 1$.

The zero-pole diagrams of the different models will not be reported since all of them are optimal for the validation tests. Passing on the analysis with the Complexity Terms, the values of the BIC and AIC terms of the different models are the following one:

$$\begin{aligned} J_{AIC}\left(\mathcal{M}_{ARMAX_8}^{A_{ND}}\right) &= -12.52 \quad J_{BIC}\left(\mathcal{M}_{ARMAX_8}^{A_{ND}}\right) = -2.900 \cdot 10^5 \\ J_{AIC}\left(\mathcal{M}_{BJ_5}^{A_{ND}}\right) &= -12.51 \quad J_{BIC}\left(\mathcal{M}_{BJ_5}^{A_{ND}}\right) = -2.899 \cdot 10^5 \\ J_{AIC}\left(\mathcal{M}_{BJ_8}^{A_{ND}}\right) &= -12.55 \quad J_{BIC}\left(\mathcal{M}_{BJ_8}^{A_{ND}}\right) = -2.909 \cdot 10^5 \\ J_{AIC}\left(\mathcal{M}_{BJ_{13}}^{A_{ND}}\right) &= -12.55 \quad J_{BIC}\left(\mathcal{M}_{BJ_{13}}^{A_{ND}}\right) = -2.908 \cdot 10^5. \end{aligned} \tag{5.1}$$

As it can be easily noted, both terms have a lower values than the ones obtained with the estimate performed in Section 3.4.1. These results confirm the hypothesis that was stated previously, more specifically, it can be said that in order to perform a good estimate it is crucial to design an input that excite the system. This will be confirmed also for the speed loop estimate. Passing on the analysis of these results, it can be seen that all the models perform almost equally but $\mathcal{M}_{BJ_8}^{A_{ND}}$ and $\mathcal{M}_{BJ_{13}}^{A_{ND}}$ are the ones that have the lower values in both terms. The Residual analysis plots are not reported since they gave the same results given by as the complexity terms tests.

Moving on the Cross-Validation test it can be seen in (5.2) the Fit terms obtained evaluating the estimated models with the Med_60 dataset. Like for the previous validation test, it can be clearly seen that there is a significant improvement with respect to the previous PEM estimates. As a matter of fact, all the models have percentage that are near to 100% and the ones with the best performances are like before $\mathcal{M}_{BJ_8}^{A_{ND}}$ and $\mathcal{M}_{BJ_{13}}^{A_{ND}}$:

$$\begin{aligned} \mathrm{Fit}_{Med}\left(\mathcal{M}_{ARMAX_8}^{A_{ND}}\right) &= 99.890\% \quad \mathrm{Fit}_{Med}\left(\mathcal{M}_{BJ_5}^{A_{ND}}\right) = 99.889\% \\ \mathrm{Fit}_{Med}\left(\mathcal{M}_{BJ_8}^{A_{ND}}\right) &= 99.891\% \quad \mathrm{Fit}_{Med}\left(\mathcal{M}_{BJ_{13}}^{A_{ND}}\right) = 99.891\%. \end{aligned} \tag{5.2}$$

The previous considerations are valid also for the other two datasets. More specifically, in (5.3) and in (5.4) are reported, respectively, the Fit percentage with the Trp_60 and 03_60 datasets. As expected, all the percentage are close to the 100% and it can be noted that the slower dataset has the higher performances and all the model performs equally:

$$\begin{aligned} \mathrm{Fit}_{Trp}\left(\mathcal{M}_{ARMAX_8}^{A_{ND}}\right) &= 99.912\% \quad \mathrm{Fit}_{Trp}\left(\mathcal{M}_{BJ_5}^{A_{ND}}\right) = 99.914\% \\ \mathrm{Fit}_{Trp}\left(\mathcal{M}_{BJ_8}^{A_{ND}}\right) &= 99.914\% \quad \mathrm{Fit}_{Trp}\left(\mathcal{M}_{BJ_{13}}^{A_{ND}}\right) = 99.914\% \end{aligned} \tag{5.3}$$

$$\begin{aligned} \mathrm{Fit}_{03}\left(\mathcal{M}_{ARMAX_8}^{A_{ND}}\right) &= 99.878\% \quad \mathrm{Fit}_{03}\left(\mathcal{M}_{BJ_5}^{A_{ND}}\right) = 99.877\% \\ \mathrm{Fit}_{03}\left(\mathcal{M}_{BJ_8}^{A_{ND}}\right) &= 99.880\% \quad \mathrm{Fit}_{03}\left(\mathcal{M}_{BJ_{13}}^{A_{ND}}\right) = 99.880\%. \end{aligned} \tag{5.4}$$

As it is clear with this analysis, with a more exciting input, the PEM estimate gives a more satisfying result. This is confirmed also in the comparison with the real model where there is a small improvement as it can be seen in Fig. 5.1.

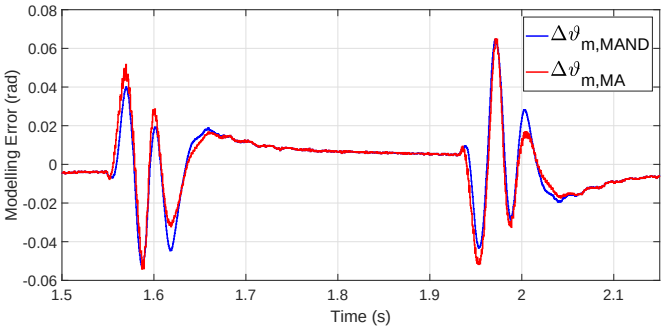

Figure 5.1: Comparison between the estimated position loop model with the new dataset (blue signal) and with the old one (red signal).

To conclude, the estimate of the models can be improved if the PEM estimate is performed with a more exiting input. More specifically, this requirment can be obtained by reducing the delay between two consecutive movements. As it will be clear shortly, these improvements will be found also in the estimate of the speed loop.

5.2 Speed Loop

Passing on the analysis of the validation results of the speed loop PEM estimate with the new dataset, the four selected models were:

- $\mathcal{M}_{ARMAX_5}^{A_{V,ND}}$: ARMAX model structure with number of parameters $n_A = n_B = n_C = 6$ and $n_k = 1$;
- $\mathcal{M}_{BJ_6}^{A_{V,ND}}$: BJ model structure with number of parameters $n_A = n_B = n_C = 6$ and $n_k = 1$;
- $\mathcal{M}_{BJ_7}^{A_{V,ND}}$: BJ model structure with number of parameters $n_B = n_C = n_D = n_F = 7$ and $n_k = 1$;
- $\mathcal{M}_{BJ_8}^{A_{V,ND}}$: BJ model structure with number of parameters $n_B = n_C = n_D = n_F = 8$ and $n_k = 1$.

As before, the zero-pole plots of the models are not reported but are all available for consultation on the MATLAB file.

As it was expected, for the Complexity Terms test, reported in (5.5), there is a significant increase of their values with respect to the position loop estimate. On the other hand, it is clear that the estimate performed with this dataset has better performances with respect to the previous speed loop estimate in configuration A. From the values reported it can be seen that $\mathcal{M}_{ARMAX_5}^{A_{V,ND}}$, $\mathcal{M}_{BJ_6}^{A_{V,ND}}$ and $\mathcal{M}_{BJ_7}^{A_{V,ND}}$ have good performances both of the terms. Moreover, the tests suggests model structures with a number of parameters

that is too high. Again, the Residual Analysis plots are omitted because their results was similar to the ones that were obtained with the Complexity Terms test:

$$\begin{aligned} J_{AIC}\left(\mathcal{M}_{ARMAX_5}^{A_{V,ND}}\right) &= 1.668 \quad J_{BIC}\left(\mathcal{M}_{ARMAX_5}^{A_{V,ND}}\right) = 1.352 \cdot 10^5 \\ J_{AIC}\left(\mathcal{M}_{BJ_6}^{A_{V,ND}}\right) &= 1.635 \quad J_{BIC}\left(\mathcal{M}_{BJ_6}^{A_{V,ND}}\right) = 1.343 \cdot 10^5 \\ J_{AIC}\left(\mathcal{M}_{BJ_7}^{A_{V,ND}}\right) &= 1.635 \quad J_{BIC}\left(\mathcal{M}_{BJ_7}^{A_{V,ND}}\right) = 1.344 \cdot 10^5 \\ J_{AIC}\left(\mathcal{M}_{BJ_8}^{A_{V,ND}}\right) &= 1.605 \quad J_{BIC}\left(\mathcal{M}_{BJ_8}^{A_{V,ND}}\right) = 1.335 \cdot 10^5. \end{aligned} \tag{5.5}$$

Moving the focus on the Cross-Validation tests the results are, as expected, good. In 3.8 are reported the Fit terms obtained with the Med_60 dataset. Moreover, it can be seen that there are two models, $\mathcal{M}_{BJ_6}^{A_{V,ND}}$ and $\mathcal{M}_{BJ_7}^{A_{V,ND}}$ having performances that are slightly better than the other two proposed models:

$$\begin{aligned} \text{Fit}_{Med}\left(\mathcal{M}_{ARMAX_5}^{A_{V,ND}}\right) &= 99.474\% \quad \text{Fit}_{Med}\left(\mathcal{M}_{BJ_6}^{A_{V,ND}}\right) = 99.481\% \\ \text{Fit}_{Med}\left(\mathcal{M}_{BJ_7}^{A_{V,ND}}\right) &= 99.482\% \quad \text{Fit}_{Med}\left(\mathcal{M}_{BJ_8}^{A_{V,ND}}\right) = 99.480\%. \end{aligned} \tag{5.6}$$

This is confirmed also in the Cross-Validation test with the slower dataset whose results are reported in (5.7). Notice that, unlike in the previous configuration A speed loop estimate, the percentage are almost constant between different dataset:

$$\begin{aligned} \text{Fit}_{Trp}\left(\mathcal{M}_{ARMAX_5}^{A_{V,ND}}\right) &= 99.401\% \quad \text{Fit}_{Trp}\left(\mathcal{M}_{BJ_6}^{A_{V,ND}}\right) = 99.409\% \\ \text{Fit}_{Trp}\left(\mathcal{M}_{BJ_7}^{A_{V,ND}}\right) &= 99.41\% \quad \text{Fit}_{Trp}\left(\mathcal{M}_{BJ_8}^{A_{V,ND}}\right) = 99.401\%. \end{aligned} \tag{5.7}$$

Finally, for the last dataset the Cross-Validation results are the following ones:

$$\begin{aligned} \text{Fit}_{03}\left(\mathcal{M}_{ARMAX_5}^{A_{V,ND}}\right) &= 99.425\% \quad \text{Fit}_{03}\left(\mathcal{M}_{BJ_6}^{A_{V,ND}}\right) = 99.423\% \\ \text{Fit}_{03}\left(\mathcal{M}_{BJ_7}^{A_{V,ND}}\right) &= 99.423\% \quad \text{Fit}_{03}\left(\mathcal{M}_{BJ_8}^{A_{V,ND}}\right) = 99.408\%. \end{aligned} \tag{5.8}$$

As it can be seen, $\mathcal{M}_{BJ_8}^{A_{V,ND}}$ is the one with the worst performances. On the other hand all the other models have almost good performances.

Furthermore, with all the validation tests results, $\mathcal{M}_{BJ_7}^{A_{V,ND}}$ is as chosen optimal model for the speed loop estimate in configuration A. This is supported by a good response across all the validation tests.

Finally, as in the speed loop estimate of configuration B, these good results on the validation test are not sufficient to have a model that has similar performances if it is used in a simulation environment. Luckily, as it is showed in Fig. 5.2, there is a small improvement with respect to the previous configuration A speed loop estimate. The estimated model performances when it is applied also the feed-forward input are almost identical with respect to the previous one.

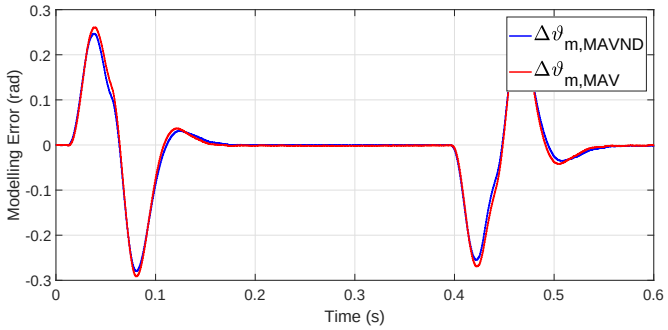

Figure 5.2: Comparison between the estimated speed loop model with the new dataset (blue signal) and with the old one (red signal).

5.3 Input Design Conclusions

It is clear from this Chapter that the input used to acquire the dataset is a key element during the System Identification procedure. More specifically, for the brushless eccentric deviator case, it is clear that sometimes, the input should be designed, case by case for each configuration under which the deviator works. More in detail, for configurations that are characterized by a low weight ferrule the dataset should be obtained with a low period between two consecutive movements. Obviously this has the constrains imposed by the brushless motor limits. Luckily, for low weighted ferrule, this problem is not relevant since, like in the case of the no delay dataset, it was possible to perform the movements without problems.

Furthermore, as it is clear, even with a low delay input, it is not possible to obtain a speed loop model that can describe optimally the eccentric deviator during the simulation with the MATLAB SIMULINK environment. A possible solution to this problem could be obtained with the addition of a well-designed feed-forward torque input that makes the torque reference signal a more suitable input for the System Identification procedure.

Moreover, by looking at the Cross-Validation results obtained in this section it is clear that this validation method highly rely on the goodness of the PEM estimate. More specifically, it can be noted that when the PEM estimate is performed with an exciting input, like the one used for the identification in this Chapter or in Section 3.5.2, the Fit terms of all dataset have always high percentage and, more importantly, the consideration on the optimal model that can be done on one set of data are usually confirmed also in the other Cross-Validation tests.

Chapter 6

Conclusion

In this final chapter are reported the conclusions on all the work performed during this thesis. First there will be an additional conclusion on the System Identification procedure with a close look at the validation tests. Afterwards there will be the final conclusion on the new proposed control law and the possibility to implement them. Finally, some idea for the future works are given.

As it was seen in Section 3.4, the test performed on the eccentric deviator gave good results for almost all the estimate models. Moreover, the two position loop models had good performances and, for the configuration B, the validation scores were also good. These results were confirmed also in Section 4.1 where, thanks to the simulated environment, it was observed that the estimated models are a good representation of the eccentric deviator and also that the data driven method is a valid option to obtain a modellization of the system. These good results were given by the possibility to easily design the input $\omega_{ref}(t)$ of the identification procedure. More in detail, this was a consequence of the fact that the signal $\omega_{ref}(t)$ was partially forced to have a structure like the one that was designed off-line during the preliminary set-up of the tests. Furthermore, from the validation tests of both position loop estimate, it was clear that, with the additional weight on the ferrule, the system was better excited by the input and this had a positive impact on the estimated model performances. On the other hand, from the validation results of the configuration A position loop it was clear that the input had to be revisited. Chapter 5 showed that to overcome this small problem it is sufficient to reduce the waiting period between two different movements. This change impacted positively on the validation results and partially on the comparison with the real model. Additionally, this shows the guidelines to set the right input for each configuration of the brushless eccentric deviator.

Differently, it was clear that the speed loop models validation performances are highly dependent to the excitement of the system. This is confirmed by the two identification performed for the configuration A where the validation result had a significant improvement when the identification was performed with a more exciting dataset. Furthermore, from the simulation with the estimated model it was clear that the models could not describe the eccentric deviator dynamics as well as the position loop estimate. This is probably a consequence of the difficulties on the design of a structured input for the PEM estimate. A possible solution to improve these performances is to perform the identification proce-

dure with a more structured input. For example, the procedure can be performed when the eccentric deviator is fed up also with a torque feed-forward input designed specifically to obtain an interesting input for the identification procedure. Moreover, future System Identification works on the brushless eccentric deviator should put a focus on the research of this input because with more performing model it is possible to design a more reliable control law for the eccentric deviator.

With all the results obtained from the System Identification procedure is safe to conclude that the optimal model should be searched in the ARMAX or in the Box-Jenkins model structure. This is supported especially by the Residual Analysis tests and the two Complexity Terms tests. Moreover, these two tests were always the best way to identify if the model. Furthermore, another key validation test was the Zero-Pole Cancellation because, thanks to this validation technique, a lot of the estimated models were discarded since they were affected by zero-pole cancellations. As it was said before, the Cross-Validation tests were useful and helped a lot during the decision of the optimal model but sometimes, when the performances of the identification process was not optimal, it added confusing information like in the case of the first speed loop estimate in configuration A.

Passing on the simulations with the MATLAB SIMULINK model, the first result that need to be noted is that performing the System Identification procedure is the right choice to obtain information on an unknown system like the brushless eccentric deviatior. As it was clear in Section 4.1 the model derived by the mechanics that was introduced in Section 1 had performances significantly worse than the one performed with the identified models. This is a consequence of the small amount of collected information on the system. An additional note is that the derived model was inadequate even for the design of the feed-forward torque input since its response was too different from the real response of the eccentric deviator. Furthermore, the modellization could not add the information of the different configuration and this is another important disadvantage of this procedure. Additionally, all the proposed modellizations were not capable to fully capture the non-linearity of the model. More specifically, for the model derived by the physical model was a consequence of the fact that the given modellization was symmetric and could not take into consideration the shape of the eccentric deviator. For the identified models, this is because the they give only linear models and consequentially it gives the model that better explains both movement, from 0 to π and from π to 0.

For the part concerning the design of the new control law for the system it can be said that for the feed-forward action there are visible improvements; more importantly, it has been already implemented in the deviator controller. For the PID design the results are good but, as it was showed, the advantages that could be obtained were limited. This may seem poor result but, as it was already explained, the main objective was to show that it was possible to design a controller using the information derived from the estimated models and predict its performances. Section 4.1 showed exactly this, in fact, the identified models were good tools to reproduce these simulations since they captured almost all the dynamic of the eccentric deviator. Furthermore, these results can also be used in a simulation environment to create new control laws for the brushless eccentric deviator.

Passing on the practical notes it can be said that the first thing that should be performed is an analysis for all the ferrules and choose the best set-up to identify the models.

During this process, a special eye must be put on the input design for the lighter ferrules. Secondly, it should be performed an estimate of the models with all the different ferrules that are used by the SMS Group. This should be performed in order to obtain all the models for which a specific control law has to be designed. This two steps can be easily performed because, once the eccentric deviator is available in the facilities, it is sufficient to perform some tests and then compute the rest of the identification analysis off-line. Finally, the last step, it is to perform a quick and informative identification of the model during the production to learn in which configuration the plant is working and adapt the controllers to obtain the chosen performances.

Unfortunately the last step of the procedure described above comes with some practical difficulties. The first one is that the controller of the machine is not designed for the implementation of the identification procedure and, since the eccentric deviator is installed in a mill, the computers that may execute the estimate are usually not optimized to perform this kind of operation. The second obstacle is the required time to acquire the data from the drive, for example, to obtain a dataset with 29990 data points and four signals it usually takes half an hour to acquire the data. Moreover, after the acquisition of the data a cleaning step was necessary. This slowed the procedure and was the reason why sometimes there were points on the acquired signals that were clearly affected by an error. Additionally, there is the problem on when to perform the movements to start the identification procedure. This can be partially solved since a good idea could be to perform the movements during the stop of the plant when there is some spare time to perform and start acquiring the data.

Finally, to obtain better models and ease the process of the System Identification procedure it could be a good improvement to reduce the time between two acquisition which is currently equal to $500\,\mu s$ but with recent changes on the drive it could be reduced to $250\,\mu s$. This can improve even more the quality of the identification of all the models with all the benefits that this implies. This improvement should come with an increase of the maximum number of data that can be acquired. These changes can help a lot the identification procedure since some dataset were cut due to the high duration of tests. Moreover, for the part of the control design, an idea is to create the torque feed-forward input is by using an identification procedure to identify the inverse model and with that obtain off-line the optimal input for all the configurations. For the position loop control, an idea for a more flexible control is the following: by deriving the space model state from the identified $\mathcal{F}(z)$, it is possible to design an observer for each configuration of the eccentric deviator.

Appendix A

Profile Description

Here are reported all the characteristic of the used profiles.

A.1 Medium Profile

The Medium profile is characterized by a total duration of $T_{Med} = 71.79\,ms$ and starts from either 0 rad or π rad. The description of its ramps are showed in Table A.1.

Table A.1: Ramps characteristics.

Ramp	Angular Velocity				Acceleration	Duration	Computed Angle	
	Starting		Final					
	rpm	$\frac{\text{rad}}{s}$	rpm	$\frac{\text{rad}}{s}$	$\frac{\text{rad}}{s^2}$	ms	$\circ$	rad
First	0	0	472.03	49.43	2800	17.65	25°	$\frac{5}{36}\pi$
Second	472.03	49.43	715.88	74.97	1400	18.24	65°	$\frac{13}{36}\pi$
Third	715.88	74.97	472.03	49.43	-1400	18.24	65°	$\frac{13}{36}\pi$
Fourth	472.03	49.43	0	0	-2800	17.65	25°	$\frac{5}{36}\pi$

A.2 Trapeze Profile

The Trapeze profile is characterized by a total duration of $T_{Trp} = 127.91\,ms$ and starts from either 0 rad or π rad. The description of its ramps are showed in Table A.2.

Table A.2: Ramps characteristics.

Ramp	Angular Velocity				Acceleration	Duration	Computed Angle	
	Starting		Final					
	rpm	$\frac{\text{rad}}{s}$	rpm	$\frac{\text{rad}}{s}$	$\frac{\text{rad}}{s^2}$	ms	∘	rad
First	0	0	390.88	40.93	800	51.17	60°	$\frac{1}{3}\pi$
Second	390.88	40.93	390.88	40.93	0	25.58	60°	$\frac{1}{3}\pi$
Third	390.88	40.93	0	0	−800	51.17	60°	$\frac{1}{3}\pi$

A.3 Medium Profile

The Run-Up profile is characterized by a total duration of $T_{RU} = 90.35\,ms$ and starts from either $-\frac{1}{9}\pi\,\text{rad} = -20°$ or $\frac{10}{9}\pi\,\text{rad} = 220°$. The description of its ramps are showed in Table A.3.

Table A.3: Ramps characteristics.

Ramp	Angular Velocity				Acceleration	Duration	Computed Angle	
	Starting		Final					
	rpm	$\frac{\text{rad}}{s}$	rpm	$\frac{\text{rad}}{s}$	$\frac{\text{rad}}{s^2}$	ms	∘	rad
First	0	0	591.72	61.97	2000	30.98	55°	$\frac{11}{36}\pi$
Second	591.72	61.97	700.14	73.32	800	14.19	55°	$\frac{11}{36}\pi$
Third	700.14	73.32	591.72	61.97	−800	14.19	55°	$\frac{11}{36}\pi$
Fourth	591.72	61.97	0	0	−2000	30.98	55°	$\frac{11}{36}\pi$

Bibliography

[1] Bolognani Silverio, *Capitolo 5 - Motore Sincrono a Magneti Permanenti (Brushless Sinusoidale)*

[2] Emerson datasheet, *Catalogo Tecnico CT Servo Drives and Motors, FEB 2016*

[3] Giovanni Incerti, Monica Tiboni, *Dinamica di meccanismi a camma veloci azionati da motori in corrente continua*

[4] Giancarlo Benettin, *Appunti per il corso di Fisica Matematica* `http://www.math.unipd.it/~benettin/links-mecc/dispense.pdf`

[5] P. K. Chattopadhyay, *Mathematical Physics*

[6] S. D. Joglekar, *Mathematical Physics: The Basics*

[7] Sadri Hassani, *Mathematical Physics: A Modern Introduction to Its Foundations*

[8] Lennart Ljung, *System Identification: Theory for the User*

[9] T. S. Soderstrom, Petre G. Stoica, System Identification

[10] Mattia Zorzi, *Lecture Notes in System Identification*

[11] Arun K. Tangirala, *Principles of System Identification: Theory and Practice*

[12] Magdi S. Mahmoud, Yuanqing Xia *Applied Control Systems Design*

[13] P. M. J. van den Hof, Bo Wahlberg, Siep Weiland, *System Identification*

[14] Karel J. Keesman, *System Identification: An Introduction*